



AFRL-RQ-WP-TR-2014-0038

HIFiRE-1 AND HIFiRE-5 TEST RESULTS

Roger L. Kimmel, David Adamczak, Matthew Borg, Thomas Juliano, and Scott Stanfield

**Hypersonic Sciences Branch
High Speed Systems Division**

FEBRUARY 2014

Final Report

Approved for public release; distribution unlimited

**AIR FORCE RESEARCH LABORATORY
AEROSPACE SYSTEMS DIRECTORATE
WRIGHT-PATTERSON AIR FORCE BASE, OH 45433-7541
AIR FORCE MATERIEL COMMAND
UNITED STATES AIR FORCE**

NOTICE AND SIGNATURE PAGE

Using Government drawings, specifications, or other data included in this document for any purpose other than Government procurement does not in any way obligate the U.S. Government. The fact that the Government formulated or supplied the drawings, specifications, or other data does not license the holder or any other person or corporation; or convey any rights or permission to manufacture, use, or sell any patented invention that may relate to them.

This report was cleared for public release by the USAF 88th Air Base Wing (88 ABW) Public Affairs Office (PAO) and is available to the general public, including foreign nationals.

Copies may be obtained from the Defense Technical Information Center (DTIC)
(<http://www.dtic.mil>).

AFRL-RQ-WP-TR-2014-0038 HAS BEEN REVIEWED AND IS APPROVED FOR
PUBLICATION IN ACCORDANCE WITH ASSIGNED DISTRIBUTION STATEMENT.

*//Signature//

ROGER L. KIMMEL
Aerospace Engineer
Hypersonic Sciences Branch
High Speed Systems Division

//Signature//

RODOLFO BUENTELLO-HERNANDEZ
Branch Chief
Hypersonic Sciences Branch
High Speed Systems Division

//Signature//

THOMAS A. JACKSON
Deputy for Science
High Speed Systems Division
Aerospace Systems Directorate

This report is published in the interest of scientific and technical information exchange, and its publication does not constitute the Government's approval or disapproval of its ideas or findings.

*Disseminated copies will show “//Signature//” stamped or typed above the signature blocks.

REPORT DOCUMENTATION PAGE					Form Approved OMB No. 0704-0188	
The public reporting burden for this collection of information is estimated to average 1 hour per response, including the time for reviewing instructions, searching existing data sources, gathering and maintaining the data needed, and completing and reviewing the collection of information. Send comments regarding this burden estimate or any other aspect of this collection of information, including suggestions for reducing this burden, to Department of Defense, Washington Headquarters Services, Directorate for Information Operations and Reports (0704-0188), 1215 Jefferson Davis Highway, Suite 1204, Arlington, VA 22202-4302. Respondents should be aware that notwithstanding any other provision of law, no person shall be subject to any penalty for failing to comply with a collection of information if it does not display a currently valid OMB control number. PLEASE DO NOT RETURN YOUR FORM TO THE ABOVE ADDRESS.						
1. REPORT DATE (DD-MM-YY) February 2014		2. REPORT TYPE Final		3. DATES COVERED (From - To) 31 January 2013 – 01 February 2014		
4. TITLE AND SUBTITLE HIFiRE-1 AND HIFiRE-5 TEST RESULTS				5a. CONTRACT NUMBER In-house		
				5b. GRANT NUMBER		
				5c. PROGRAM ELEMENT NUMBER 61102F (AFOSR)		
6. AUTHOR(S) Roger L. Kimmel, David Adamczak, Matthew Borg, Thomas Juliano, and Scott Stanfield				5d. PROJECT NUMBER 2307 (AFOSR)		
				5e. TASK NUMBER N/A		
				5f. WORK UNIT NUMBER Q042		
7. PERFORMING ORGANIZATION NAME(S) AND ADDRESS(ES) Hypersonic Sciences Branch (AFRL/RQHF) High Speed Systems Division Air Force Research Laboratory, Aerospace Systems Directorate Wright-Patterson Air Force Base, OH 45433-7541 Air Force Materiel Command United States Air Force				8. PERFORMING ORGANIZATION REPORT NUMBER AFRL-RQ-WP-TR-2014-0038		
9. SPONSORING/MONITORING AGENCY NAME(S) AND ADDRESS(ES) Air Force Research Laboratory Aerospace Systems Directorate Wright-Patterson Air Force Base, OH 45433-7542 Air Force Materiel Command United States Air Force				10. SPONSORING/MONITORING AGENCY ACRONYM(S) AFRL/RQHF		
				11. SPONSORING/MONITORING AGENCY REPORT NUMBER(S) AFRL-RQ-WP-TR-2014-0038		
12. DISTRIBUTION/AVAILABILITY STATEMENT Approved for public release; distribution unlimited						
13. SUPPLEMENTARY NOTES PA Case Number: 88ABW-2014-3421; Clearance Date: 17 Jul 2014.						
14. ABSTRACT The primary experiment for HIFiRE-1 was to measure boundary-layer transition in hypersonic flight on a 7 degree half-angle, axisymmetric cone with a 2.5 mm radius bluntness. A secondary experiment measured mean and fluctuating pressure, and heat transfer on a cylinder-33-deegree-flare geometry. The ascent provided smooth-body, low angle-of-attack, boundary-layer transition at Mach numbers greater than 5. The end of turbulent-to-laminar transition occurred at Reynolds numbers between 10.3 to 12.2 million. Second-mode N-factors of approximately 14 correlated transition. A diamond-shaped trip retained turbulent flow until reaching a roughness Reynolds number $Re_{kk} = 2200$. During re-entry, transition was measured around the circumference of the cone at Reynolds numbers ranging from 3 million on the leeside to 5 million on the windward side. In the shock-boundary layer interaction, maximum sound pressure levels of 173 dB were recorded upstream of the flare, and 185 dB on the flare itself. The principal goal of HIFiRE-5 was to measure hypersonic boundary layer transition on an elliptic cone. The second stage booster failed to ignite, so the experiment reached a maximum Mach number of only 3. Nevertheless, supersonic pressure and temperature data were obtained under laminar and turbulent flow, and flight systems were validated. Traveling and stationary crossflow instabilities were clearly measured for HIFiRE-5 in ground test in a quiet flow tunnel. The frequency, phase speed, and wave angle were all in good agreement with computations.						
15. SUBJECT TERMS boundary layer transition, hypersonic, flight test						
16. SECURITY CLASSIFICATION OF:			17. LIMITATION OF ABSTRACT: SAR	18. NUMBER OF PAGES 130	19a. NAME OF RESPONSIBLE PERSON (Monitor) Roger L. Kimmel	
a. REPORT Unclassified	b. ABSTRACT Unclassified	c. THIS PAGE Unclassified			19b. TELEPHONE NUMBER (Include Area Code) N/A	

Table of Contents

<u>Section</u>	<u>Page</u>
List of Figures.....	ii
List of Tables	v
Acknowledgments	vi
1. Summary	1
2. Introduction	2
3. Flight Vehicle, Trajectory, Instrumentation and Data Analysis.....	4
4. Ascent Phase Transition	16
4.1. Phase 1, Transition Dominated by Nose Tip Steps	16
4.2. Phase 2, Erratic Transition Progression	22
4.3. Phase 3, Smooth-Body Transition	23
4.4. Insight from High-Bandwidth Instrumentation.....	26
4.5. Intentionally Tripped Transition	30
5. Descent Phase Transition	32
6. Ascent Shock-Boundary Layer Interaction Experiment	53
7. HIFiRE-5 Flight Test Analysis	64
7.1. Vehicle Description	64
7.2. Trajectory and Vehicle Attitude	68
7.3. Transition Results	73
7.4. HIFiRE-5 Conclusions and Future Work	79
8. HIFiRE-5 Ground Test.....	81
8.1. Background.....	81
8.2. Test Article and Methods	82
8.3. HIFiRE-5 Ground Test Pressure Sensor Array Results.....	84
8.4. Traveling Crossflow Wave Properties.....	87
8.5. Repeatability at $Re=8.1 \times 10^6/m$	89
8.6. Noisy Flow	91
8.7. Summary and Conclusions for HIFiRE-5 Ground Test	93
9. References	94
List of Acronyms.....	100
Appendix - HIFiRE Flight 1 Shock-Boundary Layer Interaction Spectral Analysis.....	102

List of Figures

Figure	Page
Figure 1 HIFiRE-1 Payload Configuration	4
Figure 2 HIFiRE-1 As-Flown Trajectory	6
Figure 3 HIFiRE-1 Radial Transducer Layout	7
Figure 4 HIFiRE-1 Cone Transducer Layout Detail	7
Figure 5 HIFiRE-1 Cylinder Transducer Layout Detail	8
Figure 6 HIFiRE-1 Flare Transducer Layout Detail	8
Figure 7 Examination of Adiabatic Back Face Boundary Condition	11
Figure 8 Cone Surface Pressure During Ascent	12
Figure 9 Measured Cone Surface Descent-Phase Pressures Compared to Taylor-Maccoll Solutions Derived From AFRL and NASA BETs	12
Figure 10 Roll Angle Definition	13
Figure 11 Ascent AoA	15
Figure 12 Ascent Mach and Reynolds Number	16
Figure 13 Ascent Wall Temperature Compared to Edge and Stagnation Temperatures at	17
Figure 14 Ascent Heat Transfer for Three Smooth Side ($\phi=0$) Thermocouples	18
Figure 15 Nose Assembly	18
Figure 16 Circumferential Variation in Step Heights on Nose Assembly	19
Figure 17 Rough Side ($\phi=180$) and Smooth-side ($\phi=0$) Transitions From Tripped to Laminar Flow	20
Figure 18 Measured Nose tip Thermocouple Temperatures Compared to Conduction Solutions for Hot and Cold Nose tips	21
Figure 19 Calculated Temperature Distributions for Fully Laminar, Fully Turbulent, Hot and Cold Tip Assumptions, Compared to Flight Measurements	22
Figure 20 Smooth-Side Cone Transition After $t=15$ Seconds	23
Figure 21 Heat transfer distributions	24
Figure 22 Axisymmetry of Heat Transfer and Transition	26
Figure 23 Fluctuating Pressure PHBW1 During Ascent	27
Figure 24 PHBW1 RMS pressure fluctuations	29
Figure 25 Comparison of Vatel Heat Transfer Gauge and Medtherm Schmidt-Boelter Heat Transfer Gauge	29
Figure 26 Boundary Layer Trip	30
Figure 27 Comparison of rough-side to smooth-side heat transfer	31
Figure 28 Descent Mach and Unit Reynolds Number	32
Figure 29 Descent Freestream Temperature and Pressure	33
Figure 30 Surface Pressure Traces	34
Figure 31 Roll Angle and PLBW3 Pressure Trace Versus Flight Time During Reentry	34
Figure 32 Spin Rate Versus Flight Time During Reentry	35
Figure 33 Total AoA Versus Flight Time During Reentry	36
Figure 34 Total AoA Versus Flight Time During Laminar-Turbulent Transition	36
Figure 35 Normalized Surface Temperatures Versus Flight Time	37
Figure 36 Transition Onset Times Inferred From Surface Temperature Traces	39
Figure 37 Transition Onset Times Along Different Cone Rays	39
Figure 38 Heat Transfer Trace From the Measurement Station (0.9013 m, 15°)	40
Figure 39 Fluctuating Pressure and Normalized RMS Pressure for One Full Rotation (Top) and Periodic Waves in the Fluctuating Pressure Trace (Bottom)	42
Figure 40 Autospectral Density Function for Pressure Fluctuations Underneath Laminar Boundary, Transitional Boundary Layer, and Turbulent Boundary Layer	43

Figure 41 Contour Plot of Normalized RMS Surface Pressures Mapped Onto the Φ - Re Plane	43
Figure 42 Contour Plots of (a) Normalized Low-Frequency RMS, and (b) Normalized High-Frequency RMS of PHBW1/PLBW4	44
Figure 43 Contour Plots of (a) Normalized Low-Frequency RMS of PHBW2/PLBW4, and (b) Normalized High-Frequency RMS of PHBW2/PLBW4.....	44
Figure 44 Contour Plots of (a) Normalized Low-Frequency RMS of PHBW3/PLBW4, and (b) Normalized High-Frequency RMS of PHBW3/PLBW4.....	45
Figure 45 Azimuthal Extent of Shoulder Disturbances, $\Delta\Phi$, and Duration in Time, Δt , With Respect to Re_x	45
Figure 46 Autospectral Density Function of Periodic Disturbances Lying Between $50 < \Phi < 90$ Degrees at Station (0.8513 m, 10^0).....	46
Figure 47 Autospectral Density Function of Periodic Disturbances Lying Between $200 < \Phi < 280$ Degrees at Station (0.8513 m, 10^0).....	47
Figure 48 Power Spectra Contours In the Wind-Fixed Azimuthal Coordinate System for (a) PHBW1, (b) PHBW2, PHBW3, and (d) HT3	47
Figure 49 Comparison of the PHBW1, PHBW2, PHBW3, and HT3 Results for (a) Periodic Disturbances, and (b) Transition Front.....	49
Figure 50 Contour Plots Depicting Location of Turbulent Breakdown of Periodic Disturbances on (a) PHBW1, (b) PHBW2, and (c) PHBW3	49
Figure 51 Periodic Disturbances and Transition Front Determined From HT3.....	50
Figure 52 Mean Pressures Recorded From Low Bandwidth Pressure Transducers	55
Figure 53 Normalized Mean Surface Pressure Distributions Along the Length of the Cylinder and Flare	56
Figure 54 Heat Transfer Coefficient Distributions Along Cylinder and Flare	57
Figure 55 Normalized Saturated Data Points for the High Bandwidth Pressure Transducers	58
Figure 56 Normalized RMS Pressure Distributions Along Cylinder and Flare	59
Figure 57 Normalized RMS Pressures at Versus Time	60
Figure 58 Saturated Data Points	61
Figure 59 (a) Fluctuating Pressure Versus Time at $x=1.5213$, and (b) Normalized Histogram	61
Figure 60 Pressure Transducer Power Spectra	62
Figure 61 Sound level distributions along the length of the cylinder and flare for times 3 to 22 seconds. The black vertical line depicts the location of the corner	62
Figure 62 HIFiRE-5 Stack	65
Figure 63 Elliptic Cone Geometry and Coordinate System.....	66
Figure 64 HIFiRE-5 Payload, Including Nosetip Detail.....	66
Figure 65 HIFiRE-5 Nostetip Detail.....	67
Figure 66 Nostetip Assembly Cold Step Height.....	67
Figure 67 Closeout Side of Payload Showing Fasteners (Red Circles)	68
Figure 68 Vehicle Altitude (Left) and Velocity (Right)	69
Figure 69 Vehicle Pitch Angle (Left) and Azimuth (Right)	69
Figure 70 Vehicle Attitude Angles and Conventions	70
Figure 71 Vehicle AoA and Yaw During Ascent (Left) and Descent (Right).....	70
Figure 72 Reynolds Number Per Meter and Mach Number During Flight	71
Figure 73 Sample Surface Pressure Measurements During Ascent (Left) and Descent (Right)	72
Figure 74 Ascent (Top) and Descent (Bottom) AoA (Left) and Yaw (Right), Compared to	73
Figure 75 Heat Transfer at Upstream (Top) and Downstream (Bottom) Locations on the Leading Edge (Major Axis) During Ascent (Left) and Descent (Right).....	75
Figure 76 Heat Transfer for Upstream (Top) and Downstream (Bottom) Transducers on the Minor Axis During Ascent (Left) and Descent (Right).....	76
Figure 77 Transition Reynolds Numbers During Descent.....	78

Figure 78 Transition Location as a Function of Freestream Reynolds Number at Various Angular Locations.....	79
Figure 79 HIFiRE-5 Wind Tunnel Model.....	82
Figure 80 Schematic of Instrumentation Holes.....	83
Figure 81 PSDs for Quiet Reynolds Number Sweep, Sensors 1, 3, and 5	84
Figure 82 N-factor Contour for Traveling Crossflow for $Re = 9.8 \times 10^6 / m$	85
Figure 83 Notional Sensor Layout for Cross-Spectral Analysis.....	86
Figure 84 Typical PSD, Coherence, Phase Angle and Time Delay.....	87
Figure 85 Wave Angle and Phase Velocity for Traveling Crossflow Instability.....	88
Figure 86 PSD, Phase Angle, Wave Angle and Time Delay for 11 Runs With $Re = 8.1 \times 10^6 / m$	90
Figure 87 PSD for Noisy Flow, $Re = 0.4 - 5.5 \times 10^6 / m$, Sensor 3	92

List of Tables

<u>Table</u>	<u>Page</u>
Table 1 Freestream Conditions During Descent Transition	9
Table 2 Smooth Side Transition Times During Ascent	25
Table 3 Aerodynamic Values For 3 to 22 Seconds.....	53
Table 4 Sensor Locations	83
Table 5 Statistics for 11 repeat runs at $Re=8.1 \times 10^6/m$	91

Acknowledgments

This work was supported by the United States Air Force Research Laboratory and the Australian Defence Science and Technology Organisation and was carried out under Project Agreement AF-06-0046. Many thanks are extended to RANRAU, AOSG, WSMR/DTI/Kratos, all members of the DSTO AVD Brisbane Team, the Andoya Rocket Range of Norway and DLR/Moraba. The authors also wish to acknowledge the efforts and support of Douglas Dolvin, AFRL/RQHV and John Schmisser, AFOSR/RTE. The BEAs were provided by Mary Bedrick of Detachment 3 Air Force Weather Agency. For HIFiRE-1, Mark Smith of NASA DFRC developed a BET, and Thomas Squire of NASA ARC performed additional thermal analysis. The authors are grateful to Prof. Steven Schneider of Purdue University for donating time in the BAM6QT for HIFiRE-5 tests. Prof. Schneider's research group was very helpful in supporting these tests. Meelan Choudhari and Fei Li of NASA LaRC performed computations.

1. Summary

The Hypersonic International Flight Research Experimentation (HIFiRE) program is a hypersonic flight test program executed by the Air Force Research Laboratory (AFRL) and Australian Defence Science and Technology Organisation (DSTO). HIFiRE flight one (HIFiRE-1) flew in March 2010. The primary experiment for HIFiRE-1 was to measure boundary layer transition in hypersonic flight on a nonablating, 7 degree half-angle, axisymmetric cone with a small bluntness of 2.5 mm radius. The secondary aerothermodynamics experiment was to measure mean and fluctuating pressure, and heat transfer on a cylinder-33-degree-flare geometry behind the cone. The flight gathered pressure, temperature, and heat transfer measurements during ascent and reentry. Although the vehicle reentered the atmosphere at a higher than intended angle of attack (AoA), the ascent portion of the flight provided smooth-body, low AoA, boundary layer transition data at freestream Mach numbers greater than 5, where transition was presumed to be dominated by second-mode instability. The AoA during this portion of the flight was less than 1 degree. The end of turbulent-to-laminar transition occurred at Reynolds numbers between 10.3 to 12.2 million, based on x -location and freestream conditions. Transition was correlated with second-mode N -factors of approximately 14. A diamond-shaped trip retained turbulent flow through ascent until reaching a roughness Reynolds number $Re_{kk}=2200$.

Due to the high AoA during reentry, special care had to be taken to extract meaningful data. High bandwidth instrumentation such as the Kulite pressure transducers and Vatel heat transfer gauges could resolve local laminar and turbulent regions as the vehicle's spin carried them between the windward and leeward sides of the vehicle. These data indicated transition Reynolds numbers that were lower than during ascent. Relatively low-band periodic pressure and heat transfer disturbances were recorded just prior to transition. The transition location measured with the Medtherm thermocouples agreed well with a mean transition location derived from the higher-bandwidth instrumentation.

Analysis of the shock boundary layer interaction experiment was confined to ascent, because the high angles of attack encountered during reentry made analysis of this phase difficult. These data illustrate the movement of the separation-induced shock and upstream influence as Mach number and Reynolds number varied during descent. High sound pressure levels were recorded throughout the interaction. Sound pressure levels as high as 180 dB were recorded on the flare. Intermittency in the interaction region, with bimodal pressure distributions, was observed near the upstream influence.

HIFiRE flight five flew in April 2012. The principal goal of this flight was to measure hypersonic boundary layer transition on a three-dimensional body. The second stage booster failed to ignite, so the experiment reached a maximum Mach number of only 3. Nevertheless, supersonic pressure and temperature data were obtained under laminar and turbulent flow, and flight systems were validated. A traveling crossflow instability was clearly measured for HIFiRE-5 in ground test in a quiet flow tunnel using surface mounted pressure sensors. The frequency, phase speed, and wave angle were measured and were all in good agreement with computations.

2. Introduction

The HIFiRE program is a hypersonic flight test program executed by the United States AFRL and the Australian DSTO.^{1,2} Its purpose is to develop and validate technologies critical to next generation hypersonic aerospace systems. Candidate technology areas include, but are not limited to, propulsion, propulsion-airframe integration, aerodynamics and aerothermodynamics, high-temperature materials and structures, thermal management strategies, guidance, navigation, and control, sensors, and system components. The HIFiRE program consists of extensive ground tests and computation focused on specific hypersonic flight technologies. Each technology program is designed to culminate in a flight test. The first science flight of the HIFiRE series, HIFiRE-1, launched 22 March 2010 at the Woomera Prohibited Area in South Australia at 0045 UTC (1045 local time).

The primary objective of HIFiRE-1 was to measure aerothermal phenomena in hypersonic flight. The primary experiment consisted of boundary layer transition measurements on a 7 degree half angle cone with a nose bluntness of 2.5 mm radius. The secondary aerothermal experiment was a shock-boundary layer interaction created by a 33-degree-flare/cylinder configuration. HIFiRE-1 ground test and computation created an extensive knowledge base regarding transition and SBLI on axisymmetric bodies. This research has been summarized in numerous prior publications.^{3,4,5,6,7,8,9,10,11,12,13,14} A companion paper to the current one presented initial *N*-factor calculations for the HIFiRE-1 BLT flight experiment.¹⁵

Preliminary results from the HIFiRE-1 aerothermal experiments were previously published.¹⁶ This paper presented results from both the BLT and SBLI experiments during ascent and descent. Although the vehicle was at a higher AoA than intended during descent, the payload instrumentation scheme permitted acquisition of interesting and useful high AoA transition data.^{17,18} A subsequent publications expanded on the SBLI experiment during ascent.¹⁹

The present paper expands upon and refines the ascent BLT results. Although the descent phase was the primary design point for HIFiRE-1, a portion of the ascent yielded useful, low angle-of-attack hypersonic transition data. Ascent transition occurred in three phases. In the initial phase, during the first 11 to 14 seconds of flight, transition was induced by small backward-facing steps on the nose tip. At the end of this phase, multiple transducers on the forward portion of the cone registered a transition to laminar flow. During the second phase, from about 14 to 19 seconds, transducers on the mid-portion of the cone showed an erratic transition process, with multiple turbulent-to-laminar and laminar-to-turbulent transitions. After 19 seconds, transducers on the aft-portion of the cone showed an orderly, rearward movement of the transition front consistent with a smooth-body, second-mode transition. In addition to these data, high-bandwidth instrumentation gave some insight into unsteady phenomena during the transition process. Also, an intentionally placed, diamond-shaped boundary layer trip provided tripped transition data.

The preliminary results given by Kimmel *et al.*¹⁶ provided a general description of the laminar-turbulent transition process during reentry. It was beyond the scope of this initial investigation to provide a more detailed description. This paper expands upon the existing results providing

a more detailed description of the three-dimensional, laminar-turbulent transition process during reentry of the HIFiRE-1 flight. Specifically, power spectra, cross-spectra, and correlation techniques were used to characterize surface pressure measurements, and investigate the periodic disturbances observed during laminar-turbulent transition. These techniques required the implementation of special methods to accurately describe the distortion caused by the unevenly spaced sampling scheme of the time series data collected during flight.²⁰ The results presented in this paper utilized these methods to estimate power spectra of surface pressures measured underneath laminar, turbulent, and transitional boundary layers, and to determine the frequency, wavelength, and orientation of the periodic disturbances on the payload surface at different flight times. Other results in this section of the report include spin rates and angles-of-attack, as functions of the flight time, and normalized root-mean-squared pressures as a function of Reynolds number and angular location.

3. Flight Vehicle, Trajectory, Instrumentation and Data Analysis

The HIFiRE-1 vehicle has been described in several publications, most notably in Ref. 14. The overall payload dimensions and the different payload modules are shown in Figure 1. The experiments were carried out on the forward sections of the payload including a cone, a cylinder, and a flare that transitions to the diameter of the second stage motor (0.356 m). The nose tip consisted of iridium-coated TZM. The surface finish of the nose tip after coating was measured to be 6 to 8 microinches (0.15 to 0.2 microns) rms. The aluminum cone shell was finished to a 0.8 micron R_a finish. The cone half angle of 7 degrees was chosen to match configurations used in preceding ground tests and analytical/numerical work. One side of the cone incorporated a diamond-shaped trip element to create roughness-induced transition. The flare angle of 33° was chosen to induce turbulent boundary layer separation and reattachment on the flare face⁴ as was observed during wind tunnel testing. Two cutout channels in the flare, one of which is visible in the bottom of Figure 1, contained a laser-diode absorption spectrometry experiment that was discussed in a prior publication.²¹

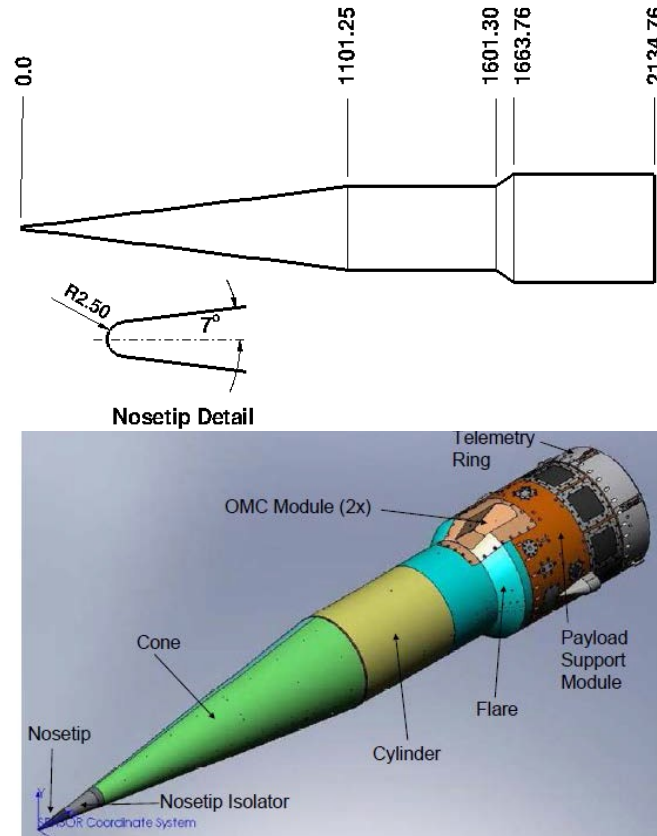


Figure 1 HIFiRE-1 Payload Configuration

The launch vehicle for the HIFiRE-1 payload was a Terrier Mk70 booster–Improved Orion sustainer²² motor combination. The Terrier and Orion motors were sourced from surplus military ordnance used extensively in sounding rocket programs. This motor combination was

chosen to minimize overall program costs and, based on past flight experience, to deliver a Mach number between 7 and 8 during the experiments. Booster and sustainer were passively spun using fin cant on the individual stages to minimize trajectory dispersion. Total payload weight was 135 kg with an all-up flight segment weight of 1554 kg and a total stack length of just over 9 meters.

The payload flew a ballistic trajectory similar to those employed for the HyShot²³ and HyCAUSE²⁴ flights. The as-flown trajectory is shown in Figure 2. The Terrier first stage burnt for 6.3 seconds and was then drag-separated from the second stage. The Orion/payload combination coasted until the second stage ignited at 15 seconds. Orion burnout occurred at 43 seconds. The payload remained attached to the second stage throughout the entire flight to provide stability as the payload reentered the atmosphere. Approximately the first and last 45 seconds of the trajectory were endoatmospheric. The remainder of the trajectory was exoatmospheric. During the exoatmospheric phase of the trajectory the Orion/payload combination was to have been reoriented with the reentry flight path angle. This was to have been accomplished using two nitrogen cold gas thrusters and a process employed for the reorientation of spinning satellites as presented by Wiesel.²⁵

A prior publication described the HIFiRE-1 mission.²⁶ The most notable complications in the mission with regard to its science objectives were failures of the on-board GPS and the exoatmospheric pointing maneuver, and drift in the cone thermocouples. The loss of the GPS meant that the vehicle altitude and velocity had to be reconstructed from existing data such as accelerometers, radar tracks, etc. Ref. 26 describes development of the BET. The failure of the exoatmospheric pointing maneuver was a more serious malfunction, since it caused the vehicle to enter the atmosphere with an AoA as high as 40 degrees. Although AoA oscillations damped and decreased as the vehicle descended, the payload AoA was still over 10 degrees as aerothermal data began to be collected during descent. Since the risk of this occurrence was recognized prior to flight, the payload flew unshrouded, i.e. no nosecone shell covered the experiment during ascent. This permitted low-AoA (< 1 degree) data to be obtained during ascent.

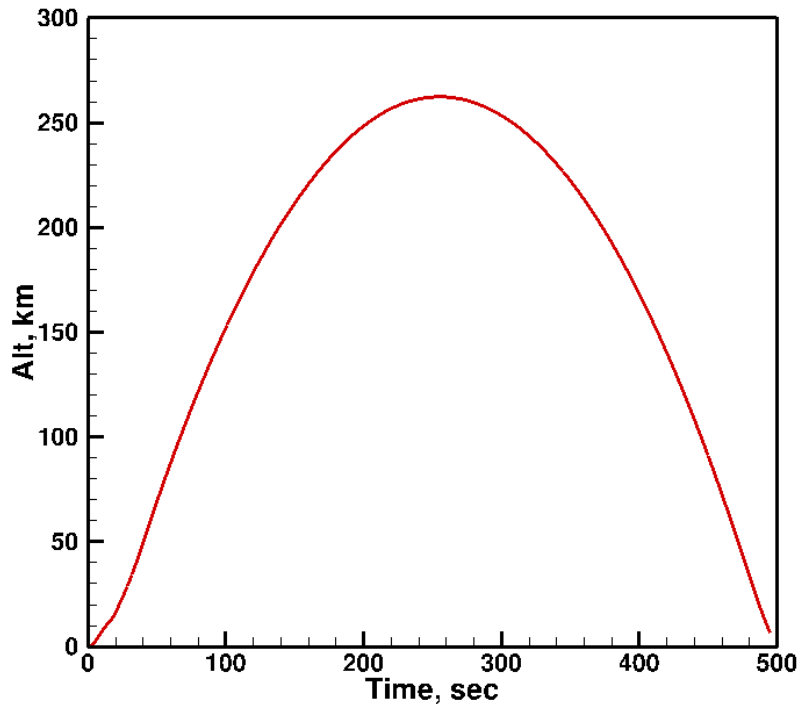


Figure 2 HIFiRE-1 As-Flown Trajectory

The primary aerothermal instrumentation for HIFiRE-1 consisted of Medtherm Corporation coaxial thermocouples. Type T (copper-constantan) thermocouples were installed in aluminum portions of the aeroshell and Type E (chromel-constantan) were installed in the steel portions. Kulite[®] pressure transducers measured local static pressures. Several pressure transducers were operated in differential mode to measure differential pressures 180 degrees apart on the vehicle to aid in attitude determination. Other transducers were referenced to internal pressure and sampled at up to 60 kHz to measure high-frequency pressure fluctuations. Figures 3 through 6 HIFiRE-1 illustrate the transducer layout. In these figures, TLBW refers to Medtherm coaxial thermocouples, PLBW refers to Kulite[®] model XCE-093 pressure transducers sampled at 400 Hz, and PHBW refers to Kulite[®] pressure transducers sampled at up to 60 kHz.

Heat transfer transducers HT1, HT2, HT6 and HT7 were Medtherm Schmidt-Boelter gauges sampled at 400 Hz. HT3 and HT8 were Vatel Corporation thin-film thermopile heat transfer gauges sampled at 4 kHz. HT5 and HT10 were ITA Inc. Delta-T gauges sampled at 400 Hz to record transition. One of these gauges failed prior to flight, and the other provided limited transition data.

All pressure transducers with the exception of the flare were model XCE-093. Those in the flare were XTEH-7LAC-190 (M). The flare transducers each output separate AC and DC-coupled signals that were digitized on different channels.

The coaxial thermocouples were dual-junction models that measured front-surface and back-surface (internal) temperatures simultaneously. These thermocouples were bonded into pre-drilled holes in the model surface using LOCTITE[®] brand adhesive. The thermocouples were installed with the back face junction flush to within 0.1 mm (estimated) of the model interior

surface. The portion of the thermocouple which extended beyond the model external surface was removed using files and abrasives so that the final thermocouple contour matched the model surface contour. This finishing process created intimate contact between the center-wire and annular thermocouple materials, resulting in a thermocouple junction.

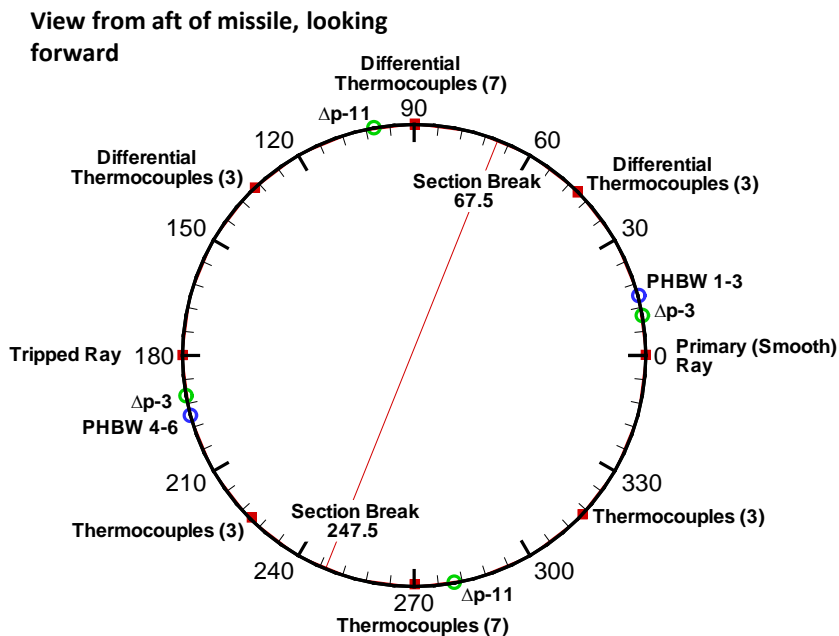


Figure 3 HIFiRE-1 Radial Transducer Layout

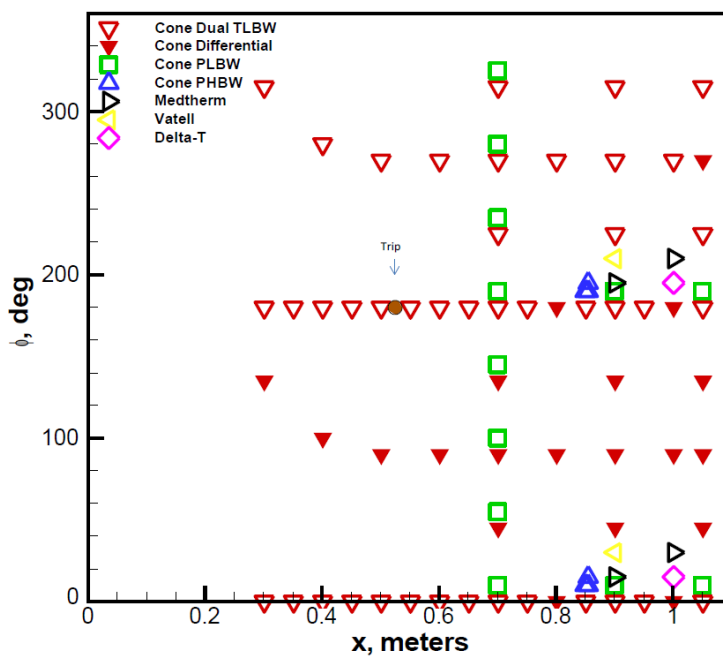


Figure 4 HIFiRE-1 Cone Transducer Layout Detail

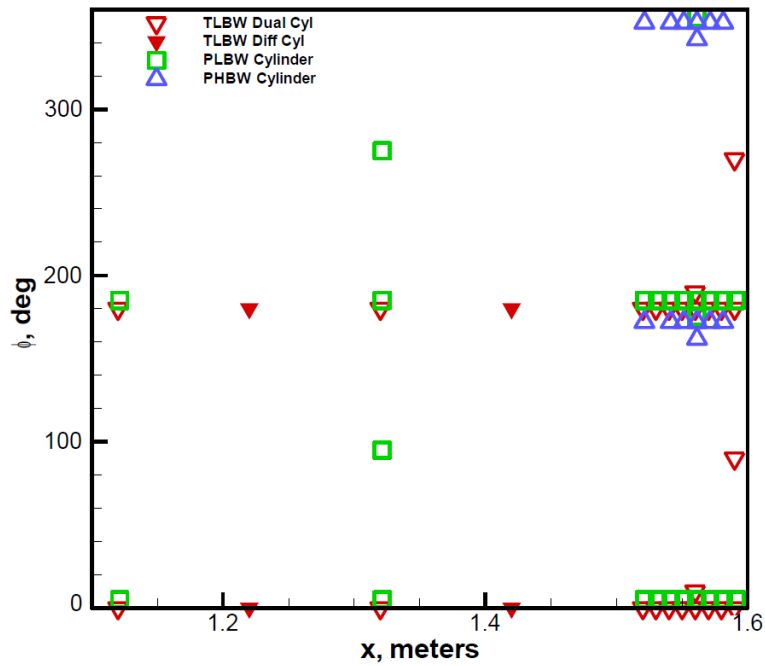


Figure 5 HIFiRE-1 Cylinder Transducer Layout Detail

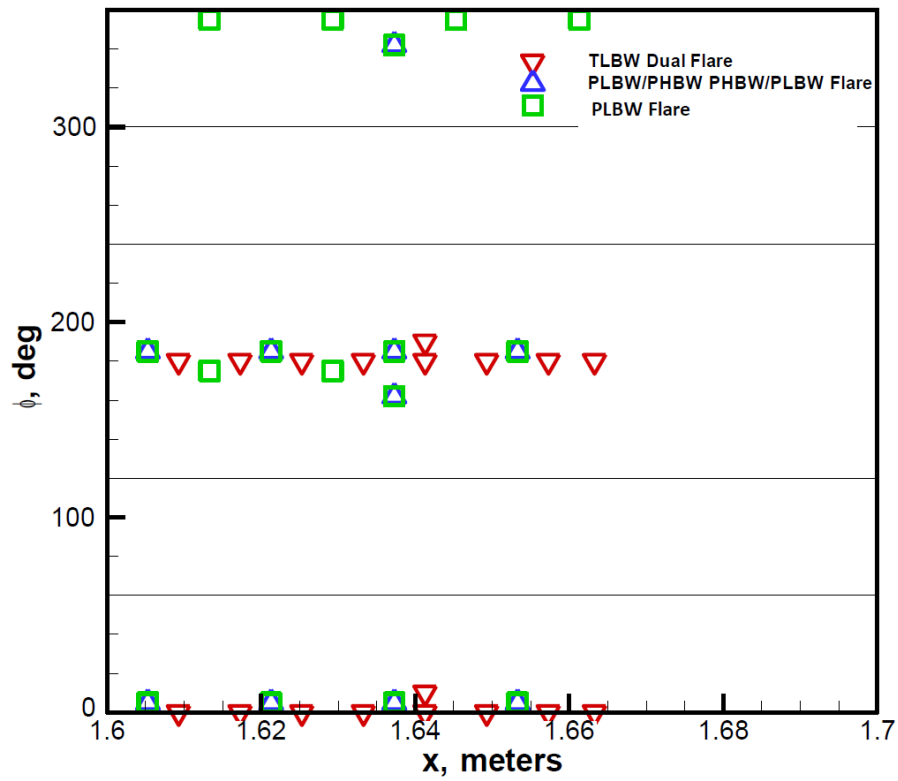


Figure 6 HIFiRE-1 Flare Transducer Layout Detail

Data analysis for the HIFiRE-1 flight required development of a best-estimated atmosphere (BEA), best-estimated trajectory (BET) and vehicle attitude estimate. A prior paper describes the BEA and BET development.²⁶ The uncertainty in the freestream unit Reynolds number was estimated assuming contributions from uncertainties in altitude, velocity, and atmospheric properties. Uncertainties in altitude and velocity were assumed equal to the residual (original minus reconstructed flight data) of the BET. Uncertainties in atmospheric properties during ascent were taken as the maximum estimated percentage uncertainties below 20 km from the BEA. Before $t=40$ seconds, estimated uncertainty in freestream unit Reynolds was estimated to be less than 2 percent. Using a similar procedure, uncertainty in Mach number was estimated to be less than 0.1 during ascent.

For descent, the freestream conditions, p_∞ , T_∞ , M_∞ and Re , were obtained from the best-estimated trajectory. The relative uncertainties for p_∞ , T_∞ , M_∞ , ρ_∞ , Re , and U_∞ are 26.8%, 2.7%, 25.0%, 25.1%, and 0.8%, as determined from the BET. The uncertainties given are the maximum uncertainties corresponding to $t = 483.5$ seconds. As will be shown later in this report, laminar-turbulent transition occurred between 480 and 485 seconds at the downstream location of $x = 0.85$ meters. During this time window, M_∞ was approximately constant with a value of $\sim 7.0 \pm 0.11$. The unit Re ranged from 2.0 ± 0.5 to $8.0 \pm 2.0 \times 10^6$ per meter. The largest percent change in unit Re for any one full spin revolution of the vehicle was 7.6%. During the 5 seconds of transitional flow, p_∞ and T_∞ ranged from 1050 ± 280 to 3500 ± 940 Pa and 235.0 ± 6.3 to 218.0 ± 5.9 K, respectively. The largest percent change in p_∞ and T_∞ during any one full rotation of the payload was 16% and 0.5%, respectively. The free stream conditions during reentry transition are tabulated in Table 1. The column designated as % Change refers to the largest percent change per full rotation of the payload during the 480 - 485 second window.

Table 1 Freestream Conditions During Descent Transition

Freestream Quantity	$t = 480$ seconds	$t = 485$ seconds	% Change
Re x 10^6 , 1/m	2.0 ± 0.5	8.0 ± 2.0	7.6
Mach Number	6.8 ± 0.1	7.0 ± 0.1	0.25
Pressure, Pa	1050 ± 280	3500 ± 940	16.0
Temperature, K	235.0 ± 6.3	218.0 ± 5.9	0.5

HIFiRE-1 transmitted data on three telemetry streams. With the exception of TM stream one, which consisted mostly of rough-side transducers, transmission quality was good. TM stream one was very noisy, with dropouts and bit shifts that degraded the quality of data on this channel.

Analysis of the thermocouple and pressure data consisted of first removing demonstrably bad points due to TM dropouts. Thermocouple data, which was originally processed using a linear thermocouple calibration, was re-calibrated to account for thermocouple nonlinearities using standard NIST calibration coefficients for type T and type E thermocouples.²⁷ The amount of correction depended on temperature and type of thermocouple. The maximum nonlinear correction for the T thermocouples during ascent was about 5 K. The maximum nonlinear correction for the Type E thermocouples was about 33 K, for thermocouples near attachment in the SBLI. SBLI thermocouples required greater adjustment due to their higher temperature.

Heat transfer analysis required that the thermocouple data be smoothed. Where data points were missing, data was linearly interpolated between good points, so that input data for the heat transfer analysis were evenly spaced in time. Back face temperatures were zero-shifted so that the average temperatures of the front and back face thermocouples for the first 0.1 seconds of data were coincident. The data were smoothed using a simple moving average of 0.2 seconds.

Heat transfer was estimated using inverse analysis.²⁸ Radiation was not considered since it was estimated to be less than 1% of convective heat transfer during periods of interest in the flight. Heat transfer at the aeroshell front face (wetted surface) was derived from the one-dimensional conduction equation

$$\dot{q} = k \frac{\partial T}{\partial y} \quad (1)$$

The temperature distribution through the aeroshell was obtained by solving the transient conduction equation

$$\frac{\partial T}{\partial t} = \alpha \frac{\partial^2 T}{\partial y^2} \quad (2)$$

The transient conduction equation requires front and back face boundary conditions. The time-history of the front face was used as one BC. Both adiabatic conditions and measured back face temperature histories were tested as back face BCs. Both boundary conditions gave similar results, although results using adiabatic back face conditions were slightly more consistent. The adiabatic back face condition was thus used for most analysis in this paper. All analysis was carried out using thermal properties for the shell materials, 6061 T6 aluminum ($C_p=896$ J/kg/K, $k=167$ W/m/K and $\rho = 2700$ kg/m³)²⁹ and AISI 1045 carbon steel ($C_p=486$ J/kg/K, $k=51.9$ W/m/K and $\rho = 7870$ kg/m³)³⁰.

Uncertainty in measured heat transfer was dominated by uncertainties in boundary conditions and measured temperature. The adiabatic back face BC was tested by using measured front face temperatures as inputs to a 1D thermal conduction model of the aeroshell in the TOPAZ finite element conduction solver. The measured front face temperatures were used as a temperature BC for TOPAZ, and the back face was treated as adiabatic. Figure 7 presents the results of two such computations at $x=0.3$ m and $x=1.05$ m. The computed back face temperature generally agreed well with the measured temperature up to about 10 to 15 seconds, especially for the more downstream measuring station. After this time the measured back face temperatures were somewhat lower than would be expected from an adiabatic back face condition, indicative perhaps of heat transfer from the back face of the aeroshell or small temperature offsets.

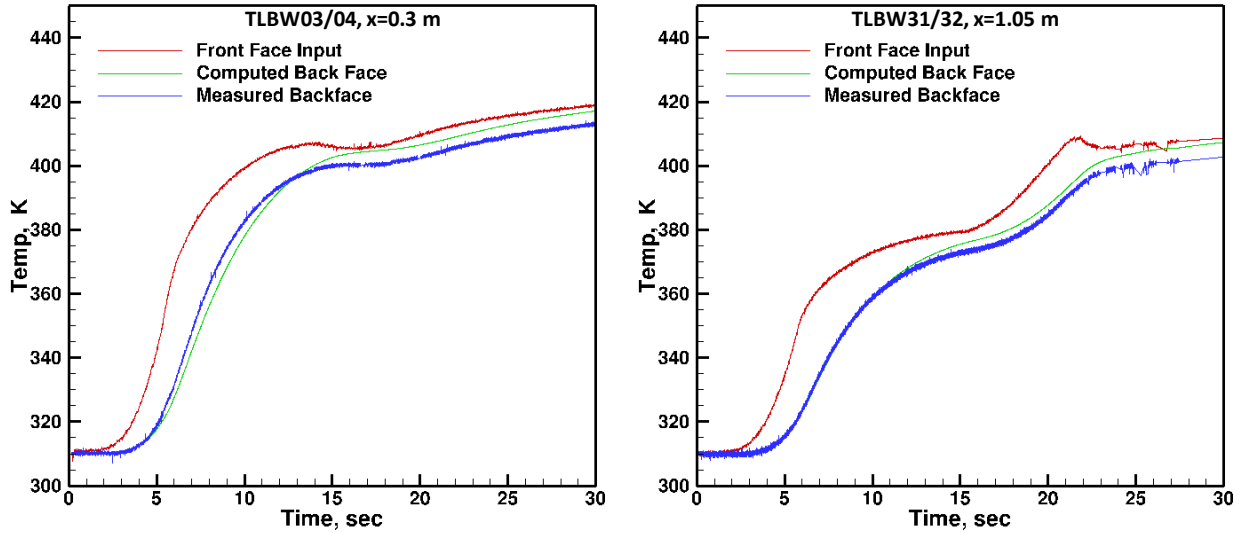


Figure 7 Examination of Adiabatic Back Face Boundary Condition

Although the difference between the expected adiabatic back face temperature and the measured temperature is less than 5 degrees, this was enough to create large percentage errors when low laminar heating levels occurred. The maximum difference between adiabatic and temperature back face BCs was about 25 kW/m^2 . Comparison with measured laminar and turbulent heating levels with predictions indicated that $\pm 25 \text{ kW/m}^2$ was a reasonable uncertainty bound on the measured heat transfer.

Pressure measurements recorded after the vehicle left the atmosphere revealed some zero shift. This zero shift for cone pressure transducers during ascent was determined by averaging the pressure for a given sensor over a 0.2 second window centered at $t = 60 \text{ sec}$ ($h = 88600 \text{ km}$). This zero shift was assumed to be linear with time during the launch, and the appropriate increment at a given time was then subtracted from the measured signal:

$$p = p_m - \frac{t}{60} \delta p \quad (1)$$

Figure 8 compares the surface pressure measured on four transducers to the Taylor-Maccoll solution³¹ for surface pressure on a 7 degree sharp cone. Although the HIFiRE configuration had a 2.5 mm radius blunt nose, comparisons of measured pressure data at $M=7$ and $Re = 1.6 \times 10^6/\text{m}$ (Ref. 11) to sharp-cone calculations showed that effects of this small bluntness were inconsequential by the most upstream measurement station. The measured pressures were generally within 6% of the Taylor-Maccoll solution. This agreement provides a posteriori validation of the BET. The periodic fluctuations in pressure, most notable for $t > 20$ seconds, are due to vehicle spin combined with small AoA. The scatter in pressure for $t < 6$ seconds is attributed to acceleration sensitivity of the transducers.

Pressure transducers on the cylinder and flare in the shock boundary layer interaction showed a more complicated zero shift during ascent. The discussion of data analysis for these transducers is deferred to Section 6.

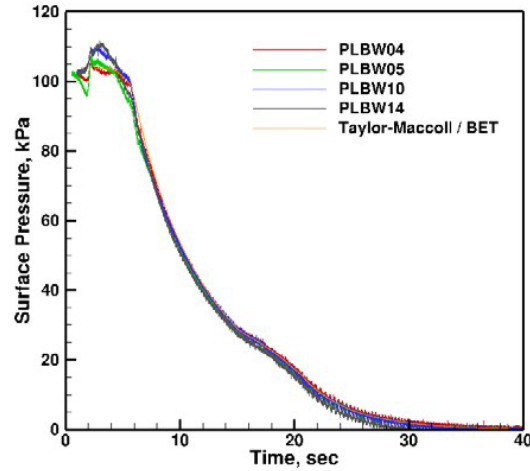


Figure 8 Cone Surface Pressure During Ascent

A similar procedure was applied to surface pressures recorded during reentry. Since in this case there was no ground-level reference, the correction consisted of a scalar shift so that transducers read zero at 456 seconds ($h=80$ km). The results of this data treatment are compared to Taylor-Maccoll solutions based on the AFRL and NASA BETs in Figure 9. Large oscillations in pressure due to the high AoA reentry are apparent. The extrema of the measured pressures bracket solutions from both BETs, but the NASA BET appears to better approximate the mean. The NASA BET was thus used for all analysis described in this paper. PLBW04 appears to drift for $t > 485$ seconds.

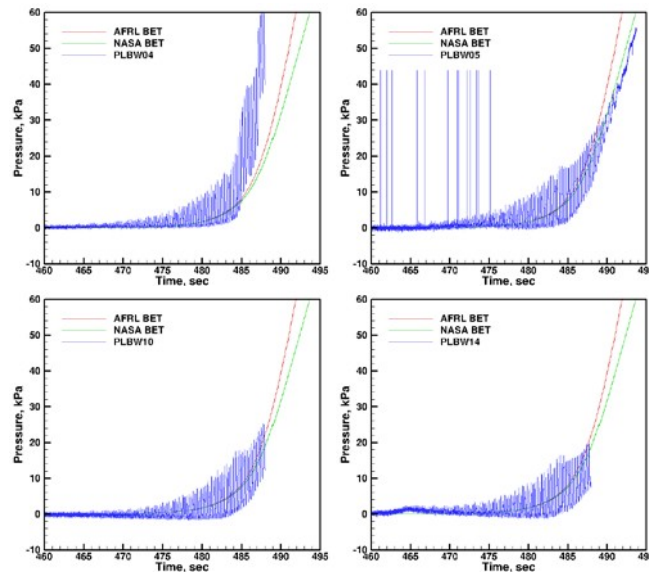


Figure 9 Measured Cone Surface Descent-Phase Pressures Compared to Taylor-Maccoll Solutions Derived From AFRL and NASA BETs

The vehicle orientation in flight is described by the velocity-referenced coordinate system shown in Figure 10. Roll angle, Φ , is defined as the angle between the $\phi=0$ primary

instrumentation ray and the velocity component normal to the missile long axis, positive counterclockwise as viewed from the front of the payload. The vehicle spin in flight was counterclockwise (viewer in front of the missile, looking aft), as determined from inspection of surface pressures, ground cameras and other onboard sensors. AoA and roll angle were determined from measured cone surface pressures. The vehicle rotated on its long axis, which in turn executed a coning motion or precession about the flight path.²³ The coning period was much longer than the spin period, so the orientation of any given transducer may be approximated as a rotation from windward to leeward and back again at constant AoA. This motion created a surface pressure that was usually a sinusoidal function in time, although at some times other lower amplitude harmonics were evident in the pressure signal, indicating a somewhat more complicated motion. The fluctuating component of the surface pressure measured with absolute pressure transducers was determined by taking a moving average of the pressure and then subtracting this from the instantaneous pressure. Differential pressure transducers also measured the pressure difference between two ports 180 apart on the cone. Two differential transducers were used to monitor four ports, but one transducer malfunctioned, leaving only one differential pressure measurement.

Several schemes were examined to determine the roll angle during ascent. Although all gave similar answers, the simplest and most satisfactory method was to locate the local maxima and minima in the differential pressure, and assume a constant roll rate (linear phase variation in time) between these two points. The spin rate varied from about 6 Hz just after first stage burnout at 8.5 seconds, to 3.7 Hz at 30 seconds. These roll rates, which are referenced to velocity, are slightly different from those extracted from the horizon sensors or magnetometers, which are earth-referenced.²⁶ Because AoA was higher during descent, a slightly more detailed assessment of roll angle was applied to this phase of flight. The description of this method is deferred to section 5.

View is from front of missile, looking aft

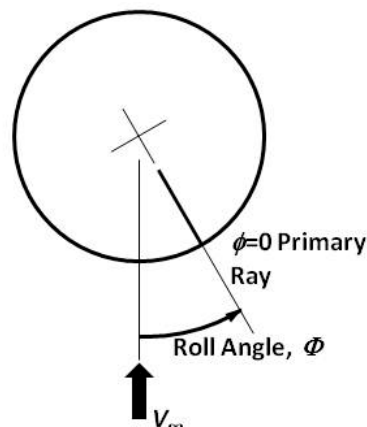


Figure 10 Roll Angle Definition

Two concerns regarding the vehicle spin need to be addressed, effects of vehicle spin on the fluid dynamics, and the time response rate of transducers. The maximum spin rate observed during ascent, 6Hz, equates to a tangential velocity of 5 m/s at the downstream end of the cone.

The missile velocity at this time was 1120 m/s. Since the tangential velocity was less than one half of one percent of the freestream velocity, it is unlikely that the missile spin had any significant fluid dynamic effect on transition. This supposition is further supported by wind tunnel tests conducted on a 9 degree half angle spinning cone.³² In these tests, carried out at Mach 5 and 8, comparison of transition data on a spinning cone to a stationary cone showed no skewing of the transition front, at spin rates up to 6,000 degrees/s (16.7 Hz roll rate) and AoA up to 6 degrees.

The second concern regarding vehicle spin was the response rate of the transducers. Assuming that transition-front asymmetries due to AoA were wind-fixed, a given transducer within the transition region would transit both laminar and turbulent areas during one revolution. A transducer would show some skewing of the transition front depending on the transducer frequency response. Given that the flight ascent data were procured at angles of attack less than 1 degree, flow asymmetry was expected to be small. Preflight ground tests gave contradictory trends regarding the effect of AoA on transition. Tests at NASA LaRC at Mach 6 at AoA=0, 3 and 5 degrees indicated that transition moved aft on the windward and forward on the leeward side of the vehicle with increasing AoA.¹³ Tests at AoA=0, 1, and 5 degrees at CUBRC at Mach 7.2 indicated a forward movement of transition on both windward and leeward with increasing AoA.⁴ CUBRC tests indicated a change in windward side transition location of 33% at 1 degree AoA. The LaRC tests indicated a windward side transition movement of only 16% at 3 degrees AoA. The Vatel heat transfer gauges provided a manufacturer-quoted response time of 17 microseconds, and the Kulite pressure transducers responded at up to 30 kHz. Given the fast response of these instruments, they were deemed adequate to resolve any AoA-induced transition asymmetries, since the vehicle spin rate was less than 6 Hz through most portions of the flight.

Ascent AoA was similarly estimated by taking local extrema in pressure for each transducer, and then interpolating AoA from tabulated values of cone pressure and Mach number. The estimated AoA was then obtained by averaging over the transducers. Figure 11 illustrates these results. During ascent, AoA was less than 0.5 degree for $t < 21$ seconds, and less than 1 degree for $t < 22$ seconds. The estimated uncertainty for AoA is 0.3 degree for ascent ($t < 22$ seconds). This uncertainty is derived from the RMS variation in calculated AoA among the transducers. For $t > 22$ seconds, the low ambient pressure gives rise to larger uncertainty.

Because descent AoA was higher, additional data and methods were applied to this phase of flight. Discussion of these methods is deferred to Section 5.

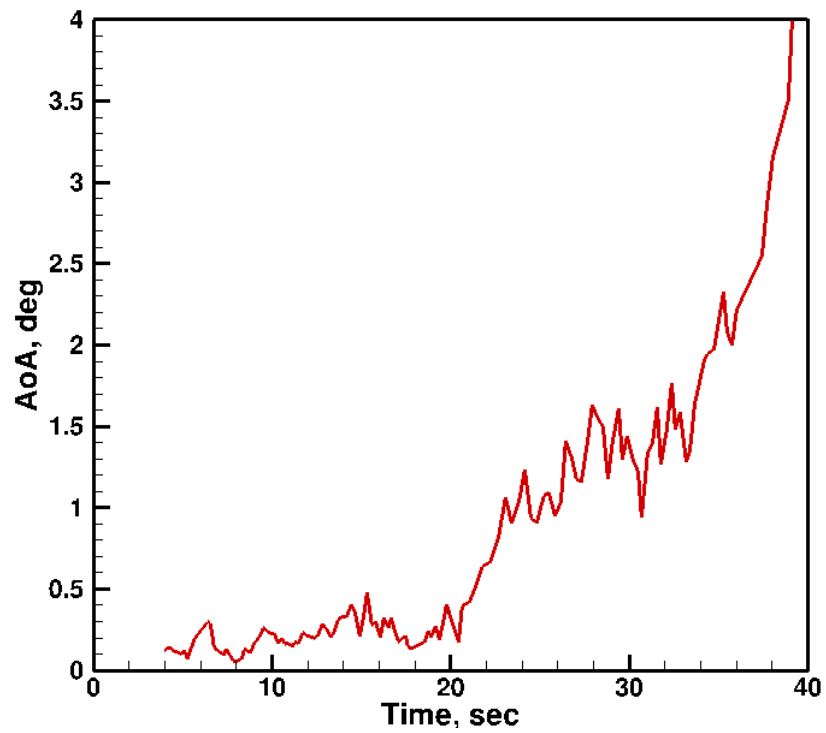


Figure 11 Ascent AoA

4. Ascent Phase Transition

4.1. Phase 1, Transition Dominated by Nose Tip Steps

The Mach number and Reynolds number varied non-monotonically through the ascent due to the motor burns. Figure 12 shows that Mach and Reynolds initially increased as the first stage burnt. Freestream Mach number and Reynolds number were derived from the BET and BEA, and the boundary layer edge values were determined from a Taylor-Maccoll solution for a sharp cone of 7 degree half-angle. The edge unit Reynolds number peaked at over 65×10^6 per meter at first-stage burnout at $t=6$ seconds. Mach and Reynolds then dropped as the vehicle coasted until approximately $t=15$ seconds, when the second stage fired. At this point Mach and Reynolds both began to climb, until about $t=19$ seconds, when Reynolds number reached a second maximum. The vehicle continued to accelerate and Mach increased after this time, but Reynolds number dropped due to the rapid decrease in air density.

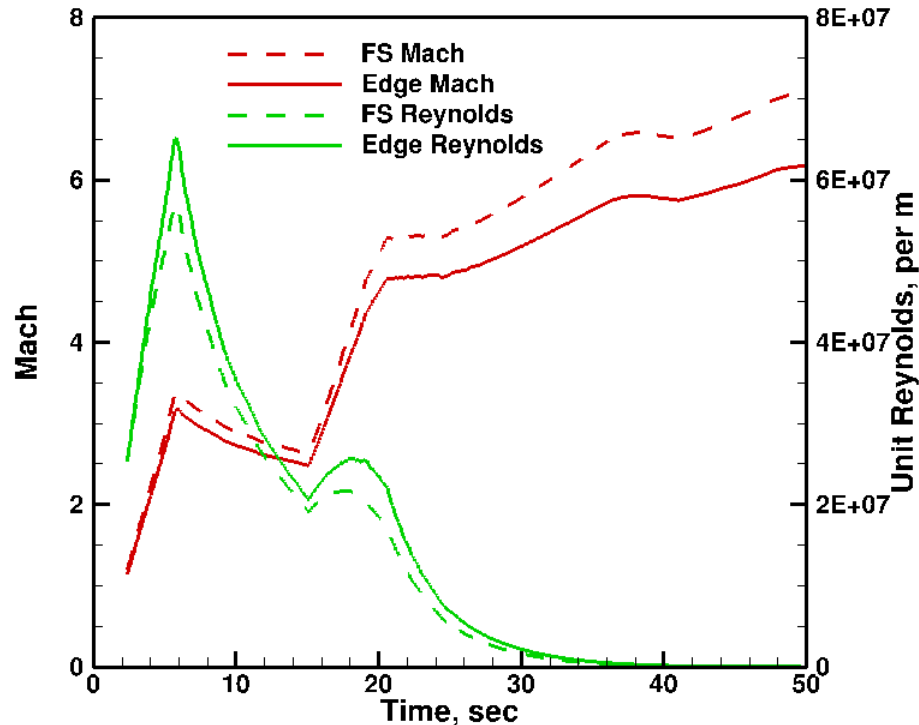


Figure 12 Ascent Mach and Reynolds Number

The wall condition throughout the flight was a cooled wall. Figure 13 illustrates the T_w/T_e and T_w/T_0 history throughout ascent for TLBW31 at $x=1.0513$ m. The edge temperature, T_e , was taken from a Taylor-Maccoll solution for the static temperature at the surface of the cone. These ratios at other x -stations on the cone were similar to those presented in Figure 13, since there was little temperature variation over the length of the cone frustum. The ratio T_w/T_0 decreased throughout first-stage burn, then increased during the coast phase. T_w/T_0 decreased sharply during the initial second-stage burn, then continued to decrease at a slower rate during the sustain portion of the second-stage burn. This ratio was approximately 25% by $t=30$ seconds.

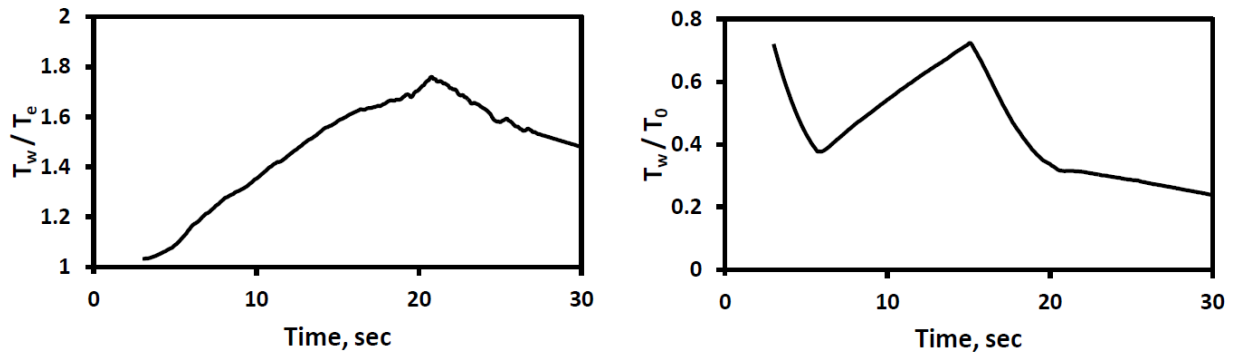


Figure 13 Ascent Wall Temperature Compared to Edge and Stagnation Temperatures at $x=1.0513$ m

During ascent, the cone boundary layer was turbulent over most of the vehicle shortly after it left the launch rail. This transition front then progressed downstream over the cone as the vehicle ascended and Reynolds number dropped. The ascent transition front movement was at odds conceptually from what we are familiar with in flight tests and wind tunnel experiments, and this creates some difficulty with nomenclature. For this reason, the first point in time at which the boundary layer at a given transducer appeared to depart from fully turbulent flow during ascent will be referred to as “TL (turbulent-laminar) onset.” For a given transducer, the last point in time at which there is discernible turbulent flow, before flow at that location goes fully laminar, will be referred to as “TL end.”

The turbulent flow early in flight probably arose from a trip near the nose. Figure 14 shows heat transfer as a function of time, derived from temperature measurements on the smooth side of the cone. Expected turbulent and laminar heat transfer derived from Eckert³³ and van Driest³⁴ theories at $x=0.3$ m are shown for reference. The expected heat transfer was computed using the measured cone temperatures and BET conditions. The trends in expected heat transfer follow the Mach/Reynolds characteristics described above. The data show that heat transfer at these two transducers ($x=0.3013$ and 0.5013 m) transitioned from laminar to turbulent values nearly simultaneously at about $t=13.5$ seconds. This rapid movement of the transition front is consistent with tripped flow. The two transducers at $x=0.5513$ and 0.6013 m were damaged before flight and did not produce data. Flow over the transducer at $x=0.6513$ m remained turbulent beyond 13.5 seconds until about 15 seconds, when it appears to have transitioned to laminar.

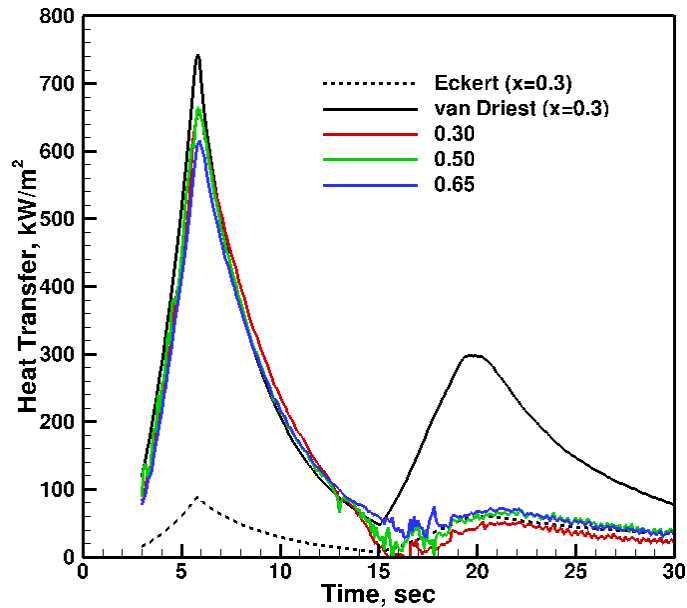


Figure 14 Ascent Heat Transfer for Three Smooth Side ($\phi=0$) Thermocouples

The suspected source of the trip during the early portions of flight was one or more backward-facing steps in the nose assembly. The nose assembly, shown in Figure 15, consisted of the TZM nose tip and steel isolator, and was attached to the aluminum cone frustum by a stainless steel joiner. To prevent steps from occurring at these joints during flight due to differential thermal expansion, small backward-facing steps were designed into the joints at room temperature. The steps were sized so that the joints would be flush with no steps at 23 km during reentry.

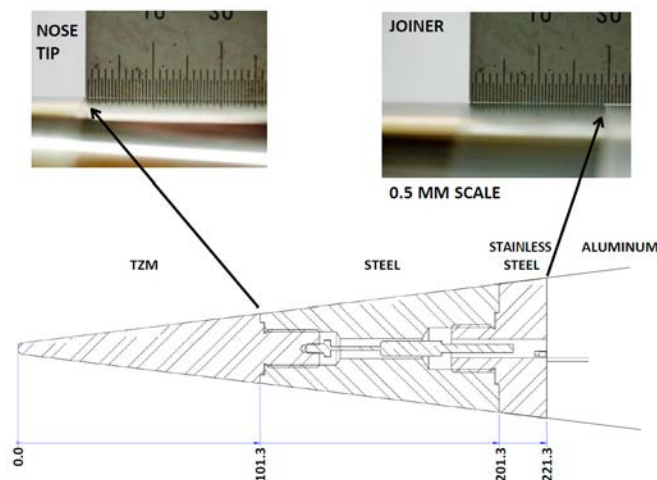


Figure 15 Nose Assembly

The as-manufactured steps were measured in the DSTO Brisbane shop using a lathe and a dial indicator. Figure 16 shows the step heights measured with this procedure. The payload was disassembled after this measurement and then reassembled at the range prior to launch. The necessary clearances between parts invariably lead to variations in joint quality each time a joint is assembled. To try to document this at the range following final assembly, a laser scan of the flight vehicle was attempted just prior to launch. This was foiled by specular reflection from the polished surface of the payload. An attempt was made to scale step heights from the macrophotos shown in Figure 15. This rough analysis indicated step heights of 0.2 mm or less, consistent with the bench measurements shown in Figure 16.

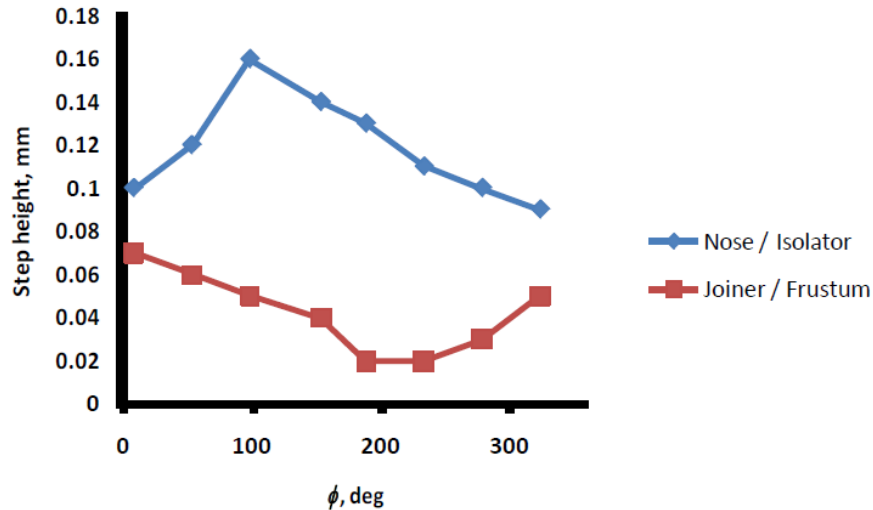


Figure 16 Circumferential Variation in Step Heights on Nose Assembly

Thermocouples at other circumferential stations indicate that the transition from tripped nose tip flow did not occur simultaneously around the model. A likely cause for this variation was the circumferential variation in the step heights in the nose assembly noted above. Figure 17 illustrates this variation in transition time. This figure shows measured heat transfer on the $\phi=0$ and $\phi=180$ degree rays of the cone at $x=0.3$ m. The $\phi=180$ ray is on the rough side of the cone, but the $x=0.3$ m station illustrated in Figure 17 is well upstream of the roughness element and uninfluenced by it. Flow over the $\phi=0$ degree ray dropped laminar at about 14 seconds, and flow over the $\phi=180$ ray dropped laminar at about 11.5 seconds. The large heat transfer fluctuations observed on the rough-side transducers at about $t=20$ seconds are artifacts due to poor signal-to-noise ratio. TL onset conditions for the smooth side transducers ($0.3 < x < 0.5$ m) were $M_\infty \approx 2.75$ and $Re \approx 2 \times 10^6$. For the rough side, TL onset conditions ($0.3 < x < 0.5$ m) were $M_\infty \approx 2.78$ and $Re \approx 27 \times 10^6$.

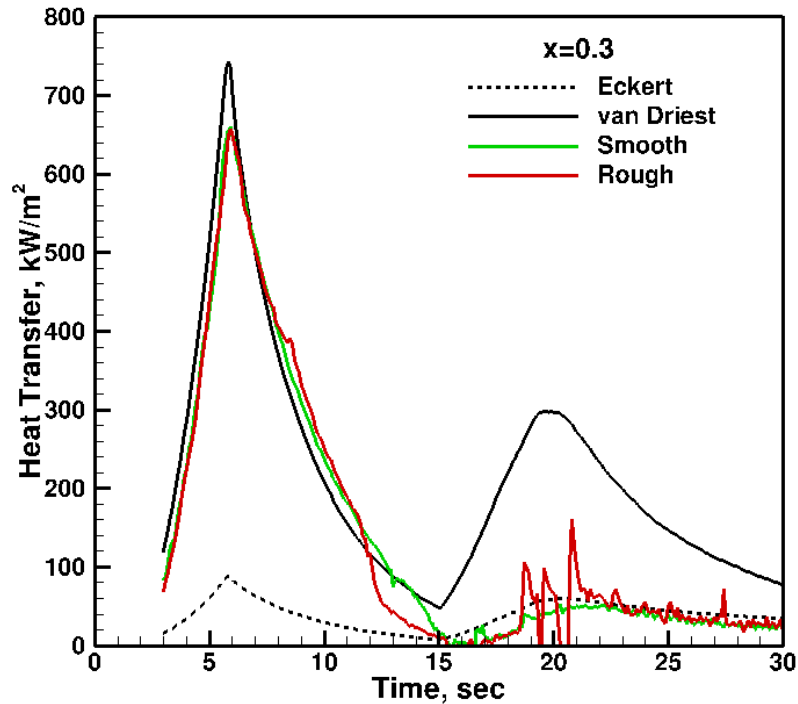


Figure 17 Rough Side ($\phi=180$) and Smooth-side ($\phi=0$) Transitions From Tripped to Laminar Flow

Finite-element conduction analysis further supports the supposition of tripped flow near the nose tip. In this analysis, two assumptions were made to bound the thermal state of the nose tip assembly. In the first case (hot tip), flow was assumed to trip at the nose tip/isolator junction, and transition to laminar at $t=14$ seconds. In the second case (cold tip), flow was assumed to trip at the joiner/frustum joint, and transition to laminar at 11.5 seconds. Laminar and turbulent heat transfer coefficients based on Eckert and van Driest heating estimates for these conditions were input into a finite-element conduction model of the nose tip. These transitions were modeled as step changes in space and time. Temperatures at two internal thermocouple locations (TLBW1 and TLBW2) were extracted from the solutions and compared to temperatures measured at these locations. TLBW1 was located in the TZM nose tip and TLBW2 was located in the joiner. Figure 18 shows that these limiting cases bounded the temperature measured on TLBW1, and the cold-tip model provided the better approximation to the TLBW2 measured temperature. Given the demonstrated circumferential nonuniformity of the heat transfer and uncertainties over trip locations, thermal contact resistances and so on, a unique solution to the measured nose tip temperatures was not expected. However, the Figure 18 results are consistent with an early trip at some point on the nose tip.

The impact of the nose joint steps was expected to diminish with time for several reasons. The boundary layer should become less sensitive to roughness as Mach number increased.³⁵ The roughness Reynolds number also would have decreased during ascent. This is because freestream Reynolds number dropped and Mach number increased, with both factors

thickening the boundary layer. Finally, as the nose temperature increased, the step heights would have decreased via thermal expansion as they were designed to do.

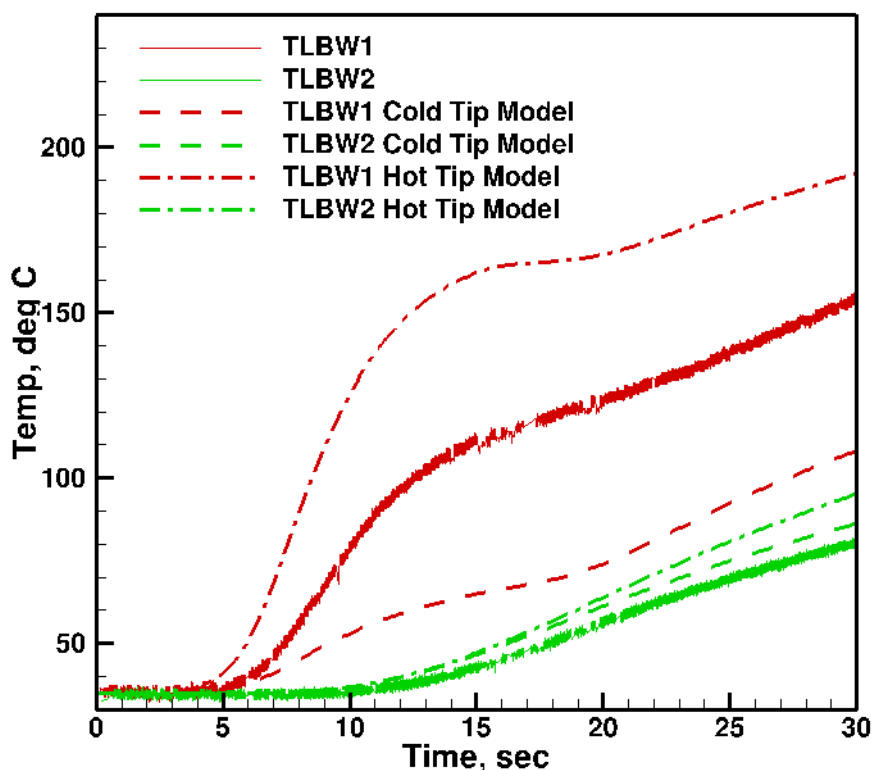


Figure 18 Measured Nose tip Thermocouple Temperatures Compared to Conduction Solutions for Hot and Cold Nose tips

The suspected early trip near the nose is significant even for later times when the transition is presumed to be smooth-body. This is because the vehicle possessed no surface instrumentation upstream of $x=0.3$ m, so the wall temperature distribution used as a boundary condition for CFD must be inferred from heat transfer calculations. Figure 19 presents an example of the effect of tripped nose tip flow on the temperature distribution. In this example, the TOPAZ code was run using convective boundary conditions based on the BET. Several cases were examined, including fully laminar, fully turbulent and two nose tip assumptions – the “hot tip” and “cold tip” cases described above. The hot and cold tip cases were assumed to be tripped at the times and locations noted above. After this, transition was assumed to occur at a number, based on edge conditions, of $Re_x=1.8e7$. This transition criterion was imposed merely to provide a rough approximation of the actual boundary conditions. The actual transition Reynolds number varied during flight. The aeroshell back face boundary condition for all cases was adiabatic. The surface temperature distribution for these cases at $t=22$ seconds is compared to the measured surface temperature distribution at the same time in flight for the $\phi=0$ degree ray in Figure 19. In all cases the computed distributions show a temperature spike near $x=0.2$ m due to the low-conductivity stainless steel joiner at this location. The first five temperature measurements agree somewhat better with the hot tip model than the cold tip. This is to be expected, since transition occurred later on this ray. Somewhat more variation was observed downstream, but this was due to the

oversimplification of the imposed transition criterion. What is most notable is the variation of 60K or more between the hot tip and cold tip cases upstream of the joiner at $x=0.2$ m. The actual temperature distribution is ultimately unknowable, but these two cases bound the wall temperature distribution.

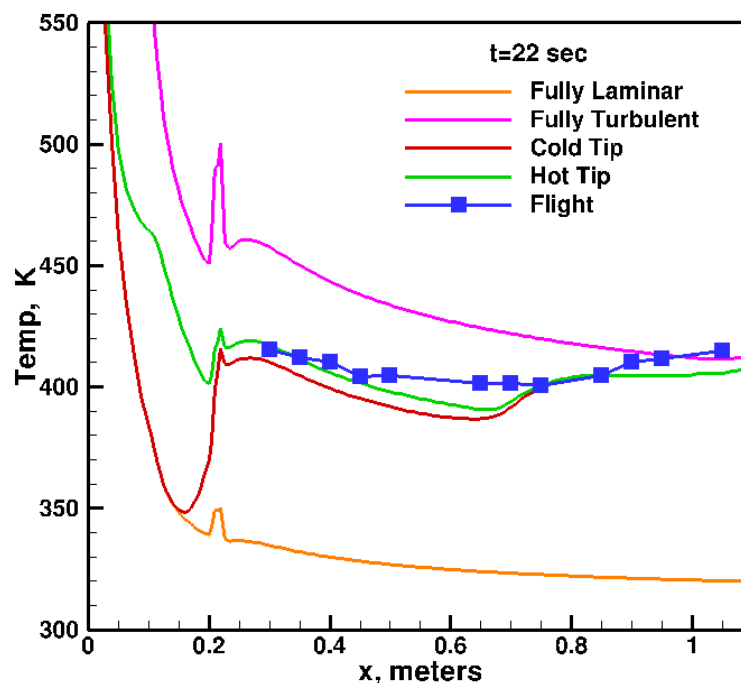


Figure 19 Calculated Temperature Distributions for Fully Laminar, Fully Turbulent, Hot and Cold Tip Assumptions, Compared to Flight Measurements

4.2. Phase 2, Erratic Transition Progression

After transition moved off the nose tip, it progressed over the cone in a more gradual fashion. Figure 20 illustrates this progression. Thermocouples at $x=0.9$, 0.95 and 1.05 m drop from turbulent to laminar flow for $20 < t < 23$ seconds. Thermocouples between $x=0.65$ and $x=0.85$ m showed a peculiar unsteady progression between $t=16$ and 20 seconds, with multiple excursions nearly equal to the difference between laminar and turbulent heat transfer. The source of these fluctuations is unknown. Their time scale appears larger than the rotation period of the missile, and thus cannot be ascribed to variations between windward and leeward transition. In any case, the AoA during this period was less than 0.5 degrees. This period occurred when the second-stage booster was at maximum thrust, and might be related to disturbances arising from the motor firing, although no large oscillations were evident in the vehicle accelerometers.

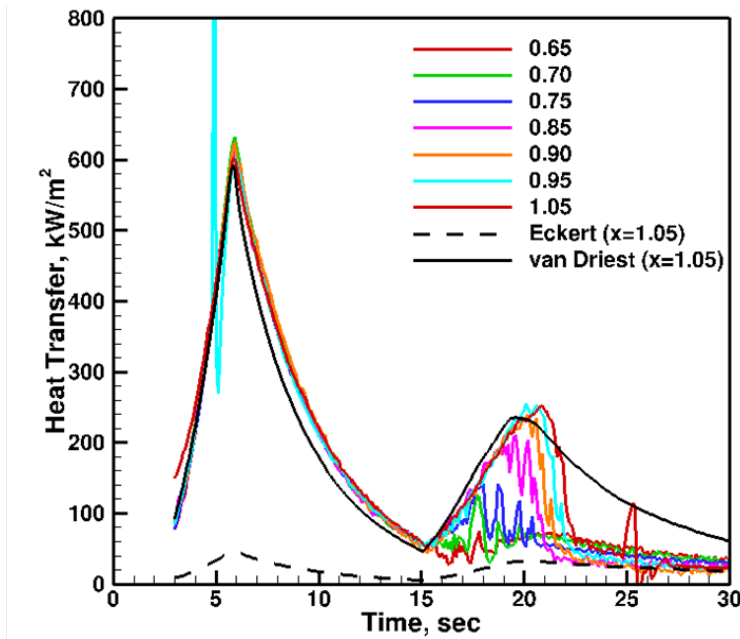


Figure 20 Smooth-Side Cone Transition After $t=15$ Seconds

4.3. Phase 3, Smooth-Body Transition

The transition progression may also be visualized by examining heat transfer distributions over the cone at fixed points in time. This data presentation is an aid to visualization, since it resembles the traditional presentation of wind tunnel data. Obtaining quantitative heat transfer on the cone was not a primary objective of the HIFiRE-1 mission, but an effort was made to extract this data in order to better understand the transition process. Although the measured heat transfer data showed significant scatter, up to 70% of expected laminar heat transfer, transition trends may still be extracted. Figure 21 presents heat transfer coefficient as a function of Reynolds number for times between $t=19$ and 22 seconds. In this figure, symbols indicate flight data, dashed lines are predicted Eckert laminar heat transfer, and solid lines are predicted van Driest turbulent heat transfer. Heat transfer coefficient and Reynolds were both referenced to freestream values. Over this period, transition moved steadily back over the cone. The maximum transition Reynolds number derived from Figure 21 occurred at 19 seconds, and was approximately 14.5×10^6 (freestream conditions) or 18×10^6 (edge conditions). Table 2 summarizes the transition times derived from smooth-side thermocouples during ascent. Edge unit Reynolds numbers in this table were determined using surface conditions computed with a Taylor-Maccoll solutions for a sharp cone at the appropriate freestream conditions. The nearly simultaneous transition at stations at $x=0.5$ m and upstream is a further indication of tripped behavior. Transition upstream of $x=0.85$ m was difficult to define due to the oscillatory nature of the heat transfer.

Stability calculations for HIFiRE-1 indicated correlating N -factors of 13.5 to 13.7 for $21 < t < 22$ seconds, with a second-mode dominated transition.¹⁵ This number is well above the value of $N=5.5$ observed in wind tunnel tests of HIFiRE-1,^{5,10} and higher even than the commonly referenced $N=10$ presumed for free flight.^{36,37} Stability calculations by multiple researchers for

the Reentry-F and Sherman-Nakamura hypersonic flight tests indicated correlating N -factors of 3.7 to 15.^{37,38} The investigators ascribed much of this variation to uncertainty in the calculated boundary conditions. With the lowest Reentry-F case excluded, correlating N -factors for these two flights ranged from 8 to 15. Transition during the latter phase of HIFiRE-1 was thus not only consistent with a smooth-body, second-mode transition, but the flight also provides a reference case with well-defined boundary conditions for determination of correlating N -factors in hypersonic flight.

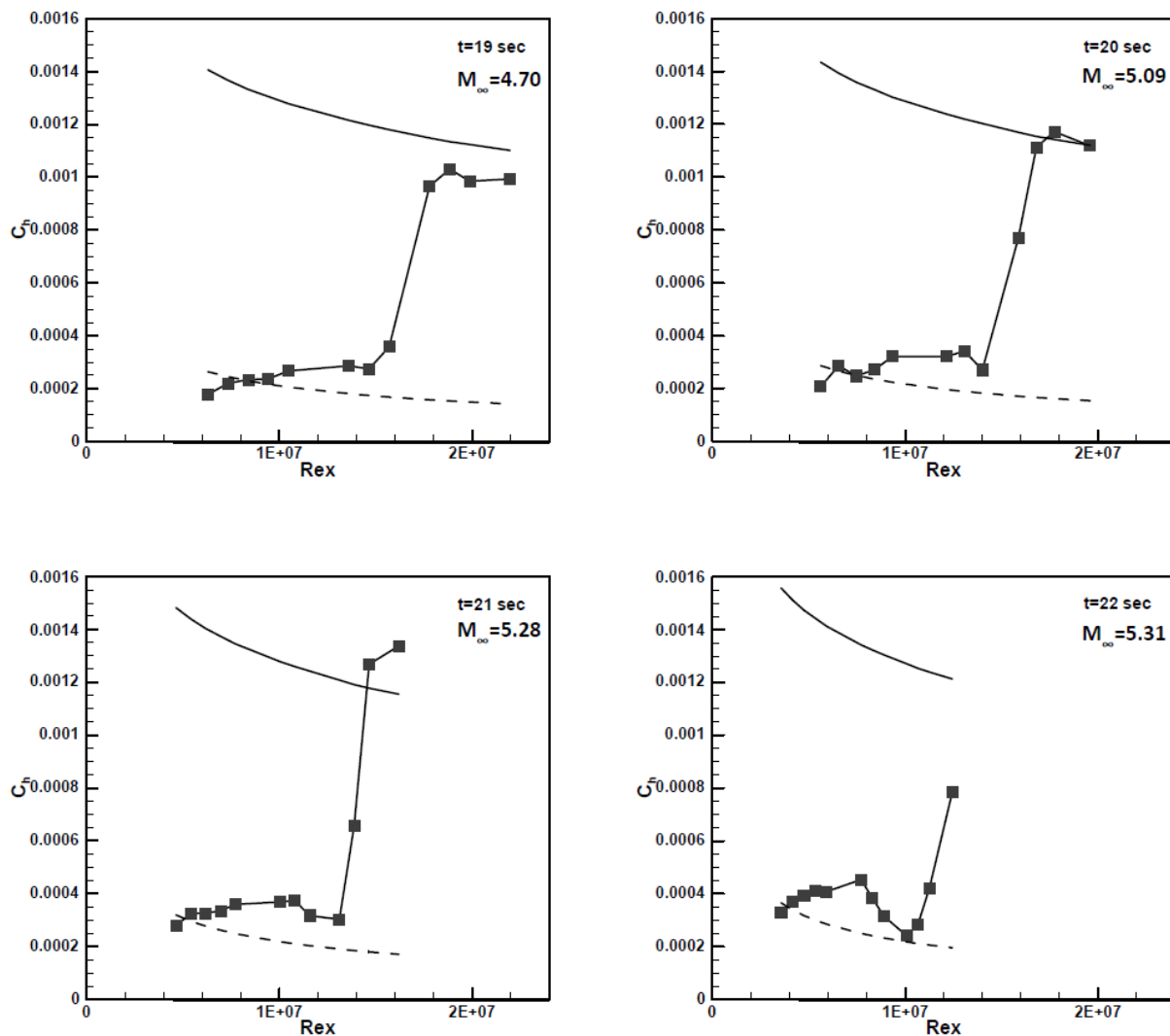


Figure 21 Heat transfer distributions

Table 2 Smooth Side Transition Times During Ascent

TL Transition Onset								
Axial distance from stagnation point, x	Surface arc length from stagnation point, s	Time after liftoff, t	Freestream unit Reynolds number, Re	Edge unit Reynolds, Re_e	Freestream Mach, M	Edge Mach, M_e	Rex	$Re_e s$
m	m	s	1/m	1/m				
0.3013	0.3037	13.8	21490000	23380000	2.65	2.51	6474937	7099631
0.3513	0.3540	14.2	20710000	22490000	2.63	2.49	7275423	7962316
0.4013	0.4044	14.49	20000000	21690000	2.62	2.47	8026000	8771729
0.4513	0.4548	14.49	20000000	21690000	2.61	2.47	9026000	9864373
0.5013	0.5052	14.5	19970000	21660000	2.61	2.47	10010961	10941862
0.6513	0.6563	15.29	18920000	20540000	2.64	2.49	12322596	13480215
0.7013	0.7067	15.44	19100000	20820000	2.69	2.54	13394830	14712794
0.7513	0.7570	17.99	20990000	24790000	3.96	3.67	15769787	18767067
0.8513	0.8578	18.79	20380000	24760000	4.39	4.04	17349494	21238949
0.9013	0.9082	20.16	18260000	23140000	5.03	4.58	16457738	21015013
0.9513	0.9585	20.12	18300000	23160000	5.01	4.56	17408790	22199873
1.0513	1.0593	20.91	16320000	20990000	5.27	4.77	17157216	22234595
TL Transition End								
0.3013	0.3037	15.59	19280000	21090000	2.75	2.6	5809064	6404244
0.3513	0.3540	15.72	19450000	21340000	2.8	2.64	6832785	7555172
0.4013	0.4044	15.5	19170000	20920000	2.72	2.56	7692921	8460331
0.4513	0.4548	15.5	19170000	20920000	2.72	2.56	8651421	9514186
0.5013	0.5052	15.71	19440000	21320000	2.8	2.64	9745272	10770107
0.6513	0.6563	17.98	20980000	24770000	3.95	3.66	13664274	16256325
0.7013	0.7067	20.23	18160000	23060000	5.07	4.61	12735608	16295726
0.7513	0.7570	20.79	17060000	21970000	5.29	4.79	12817178	16632209
0.8513	0.8578	21.51	13700000	17600000	5.24	4.74	11662810	15097153
0.9013	0.9082	21.58	13500000	17400000	5.25	4.75	12167550	15802128
0.9513	0.9585	22.38	10900000	14000000	5.23	4.74	10369170	13419612
1.0513	1.0593	22.51	10500000	13500000	5.22	4.73	11038650	14300478

The symmetry of the transition process was assessed by comparing output from transducers located at the same axial location but at different circumferential locations. The $\phi=0, 180$ (upstream of the diamond trip), 270, 315 degree rays are considered since they had instrumentation at similar x -locations. Figure 22 shows these results at several axial locations. Generally, turbulent and laminar heat fluxes were the same on all the rays within experimental scatter. The $\phi=0$ and 315 degree rays showed similar transition behavior at all the x -stations considered. At $x=0.4$ m, the $\phi=270$ degree and $\phi=0$ rays transitioned nearly simultaneously. At this same x -station, the $\phi=180$ degree transducer (on the rough side of the cone but upstream of the roughness element) transitioned earlier than the other two rays, as noted above. At $x=0.7$ m, the $\phi=0$ and 315 degree rays behaved similarly, but the $\phi=270$ degree transducer transitioned much later than the other two rays. At $x=0.9$ m, the $\phi=0, 270$ and 315 degree rays were similar, although the $\phi=270$ degree ray transitioned somewhat later than the other two rays. At $x=1.05$ m, the $\phi=0$ and 315 degree rays transitioned simultaneously. In summary, for the rays considered, the circumferential symmetry in laminar and turbulent heat transfer was good. The transition symmetry was good downstream of $x=0.85$ m (or after about 19 seconds). Upstream (or before) this, transition showed some asymmetry, with the 270 degree ray transitioning later than the $\phi=0$ and 315 degree rays. The

implication is that prior to 19 seconds, the $\phi=270$ degree ray was influenced by some type of roughness different from the other rays. Although the $\phi=270$ degree ray was adjacent to the diamond trip at $\phi=180$ degrees, $x=0.5263$ m, it is unlikely that the effect of the trip would have spread far enough laterally to contaminate flow on the $\phi=270$ degree ray. Therefore it is surmised that prior to 19 seconds, the $\phi=270$ degree ray was influenced by some other roughness on the upstream portion of the cone.

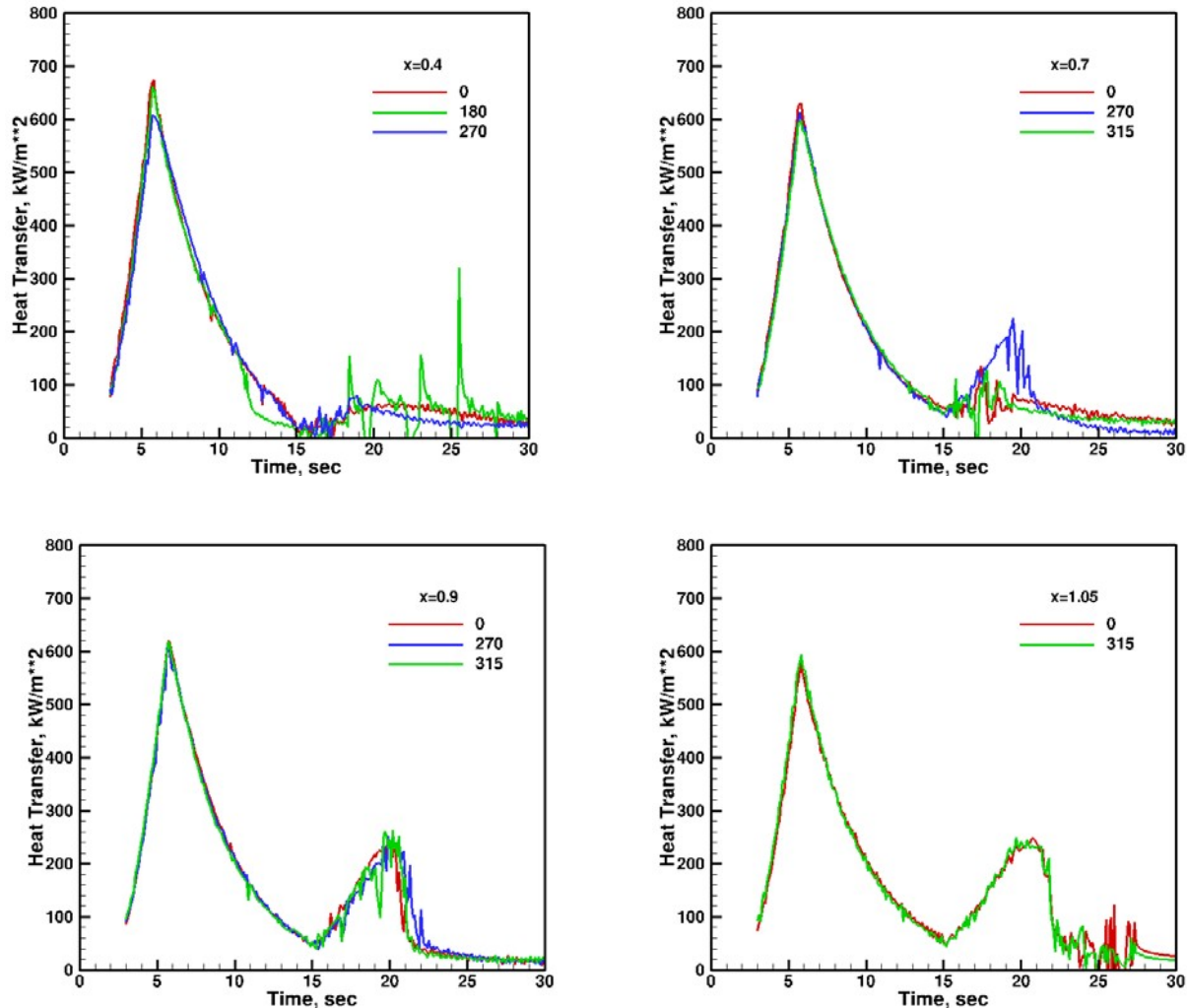


Figure 22 Axisymmetry of Heat Transfer and Transition

4.4. Insight from High-Bandwidth Instrumentation

Additional insight into the transition process was gained by examining higher bandwidth sensors. Figure 23 presents pressure fluctuations from one high-bandwidth Kulite® pressure sensor, PHBW1. Similar results were obtained from the other two smooth-side Kulites®. The Kulite® pressure transducers on the cone were sampled at 60 kHz and bandpass filtered between 100 Hz and 30 kHz. Although the frequency response of the transducer was an order of magnitude lower than expected second-mode instability frequencies, the instrument at least gave some

measure of the transition dynamics. The left side of Figure 23 presents dimensional pressure fluctuations. The right side of the figure shows the same data normalized by the local cone static pressure. The static pressure was derived from a Taylor-Maccoll solution based on the BEA and BET. As shown in Figure 8, the Taylor-Maccoll solution provides a good representation of the measured static pressure, but is free of noise. Pressure fluctuations in the turbulent boundary-layer prior to about 18 seconds mirrored the local mean pressure, increasing to a maximum at first stage burnout, then declining as the vehicle coasted. A jump in pressure fluctuations at about $t=3$ seconds occurred when the vehicle went sonic. After this time, pressure fluctuations (as a percentage of local static pressure) were largely constant until about $t=15$ seconds. Large fluctuations occurred when the second stage fired at 15 seconds, but these were largely spurious and due to interference between the second-stage exhaust plume and the TM. The large fluctuations at this time consisted of numerous single-point spikes. Pressure fluctuations began to grow until about 20 to 21 seconds, when they suddenly collapsed. Transition was measured on the thermocouples at this x -station between 18.8 to 21.5 seconds.

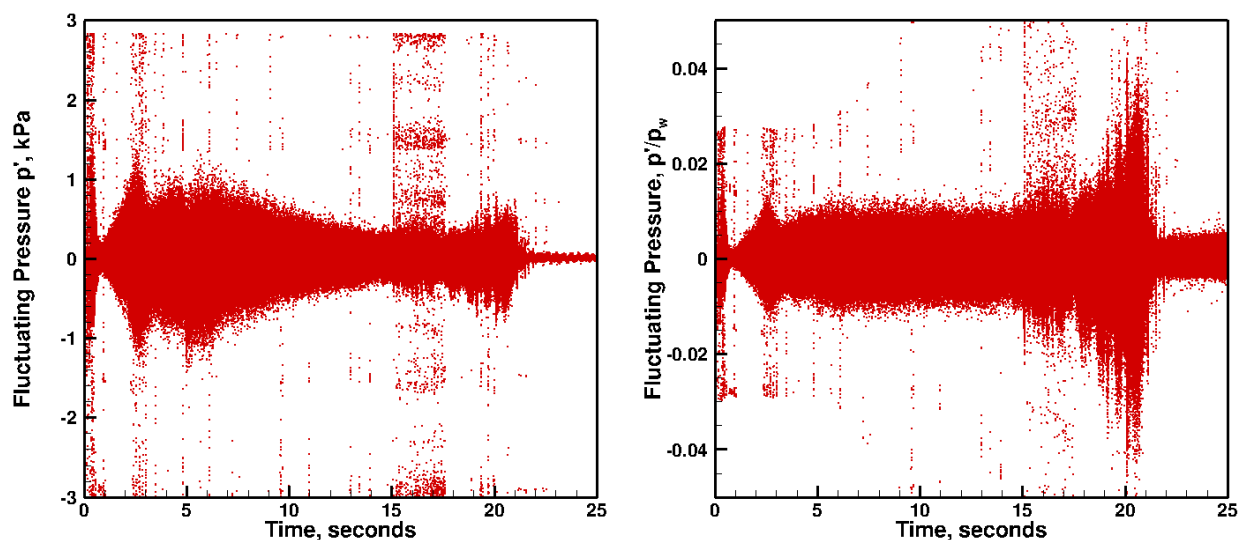


Figure 23 Fluctuating Pressure PHBW1 During Ascent

Figure 24 presents PHBW1 pressure fluctuations measured on the cone during ascent, expressed as an RMS value. The RMS was calculated over a moving 2000 point window, and was normalized by the local mean pressure measured calculated using a Taylor-Maccoll. As shown in Figure 23, a small low-frequency modulation due to vehicle spin occurred in the high-bandwidth pressure signal, even though the signal was band-pass filtered. This low-frequency ripple and any DC offsets were removed by subtracting the mean signal, derived from a 2000 point moving average. The boundary layer at this location was fully turbulent (as measured by heat transfer) until approximately $t=18.8$ seconds. After this, the flow transitioned to fully laminar at $t=21.5$ seconds. The sharp rise in the RMS between 15 to 17 seconds is due to telemetry noise during the initial second-stage firing, and is spurious. RMS pressure fluctuations beneath the supersonic turbulent boundary layer were constant at about 0.4%. Pressure fluctuations measured beneath turbulent boundary layers on cones range from 1 to 3 % in conventional wind tunnels.³⁹ Similar ground measurements under quiet

conditions are not available. The rise in pressure fluctuations near 20 seconds is typical of measurements of transitional boundary layers made in wind tunnels.³⁹

Figure 24 shows the normalized RMS pressure rising after $t=23$ seconds. Part of this rise is due to small errors in the mean pressure, and part of this is a bias in the signal due to electronic noise. The electronic noise floor was estimated as the measured sensor RMS at $t=60$ seconds, which was about 8 Pa. The contribution of electronic noise to the turbulent signal was negligible, but at $t=25$ seconds it accounted for about one half of the signal RMS shown in Figure 24. It should also be noted that the frequency response of the Kulite sampling system was 30 kHz. Probably a substantial portion of the turbulent pressure fluctuation spectrum was above this frequency, so the RMS values, especially for turbulent flow, are probably understated.

Figure 25 shows the dynamics of the transition process during ascent as revealed by a Vatell heat transfer gauge (HT3) and a Medtherm Schmidt-Boelter gauge (HT2). Both devices are thermopiles, but the Vatell device is a thin-film gauge with a higher frequency response than the Medtherm. The manufacturer-quoted time constant for the Vatell gauge is 17 microseconds. No such data were available for the specific Medtherm Schmidt-Boelter gauges that were flown, but similar models had stated time constants of 10 to 15 msec. These gauges were located at $\phi=30$ degrees. HT3 was located at $x=0.90$ m, and the HT2 was located just downstream at $x=1.0$ m. These gauges reveal that the transition process that occurred between about $21.0 < t < 22.4$ seconds was the result of multiple rapid transitions between turbulent and laminar flow. The period of laminar flow between turbulent episodes gradually increased, until the flow was fully laminar.

HT2 and HT3 were well-correlated, with HT2 showing a damped response due to its lower frequency response. This degree of correlation indicates that the phenomenon was a flowfield feature, and not a characteristic of the individual transducer. The thermocouples located at $x=0.9013$ m indicated transition onset and end for $20.16 < t < 21.58$ seconds. Throughout ascent, the Schmidt-Boelter gauges indicated lower heat transfer than the thermocouples, and the Vatell gauge measured heat transfer was less than the Schmidt-Boelters, but all devices indicated similar heat transfer trends. Similar unsteady transition movement was observed on thermocouples and Kulite gauges, although the thermocouple response was even more damped than the Medtherm response.

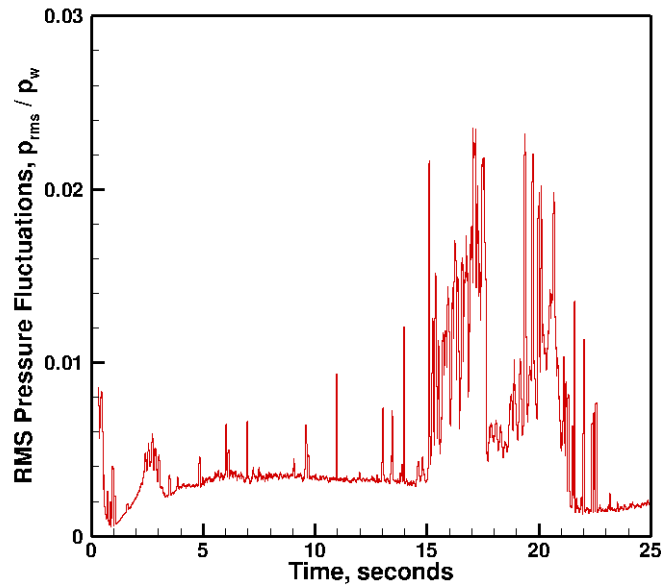


Figure 24 PHBW1 RMS pressure fluctuations

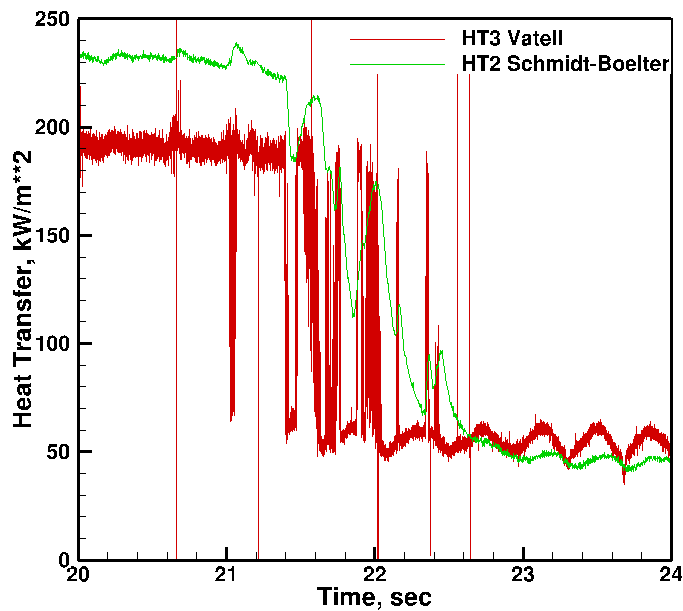


Figure 25 Comparison of Vatell Heat Transfer Gauge and Medtherm Schmidt-Boelter Heat Transfer Gauge

The modulation of heat transfer evident after about 22 seconds was due to the spin of the vehicle, and permits a qualitative comparison of the intermittency to the spin period. Transition occurs over about three spin periods. Since the periods of turbulent flow appear at roughly the same location in each period, it is likely that the intermittency is related to the vehicle orientation. In the period between the first laminar drop at 21.02 seconds and the last

turbulent spike at 22.42 seconds, the freestream unit Reynolds number dropped from 15.8×10^6 to 10.7×10^6 per meter. During this time, AoA increased from 0.4 to 0.7 degrees. Similar intermittent behavior was observed on the Kulite gauges, but with less resolution.

4.5. Intentionally Tripped Transition

The cone ray diametrically opposed to the smooth-side thermocouple ray contained a diamond-shaped trip centered at $x=0.5263$ m. Figure 26 shows the trip construction and a photo of the installed trip. Medtherm coaxial thermocouples are visible upstream and downstream of the trip. The planform of the trip was a square, 10 mm on each side, with radiused corners. The nominal trip height above the cone surface was 2 mm, and it was constructed of copper. The top surface was radiused to the cone centerline at $x=0.5263$ m so that the height of the trip above the payload surface did not depart substantially from 2 mm at any point.

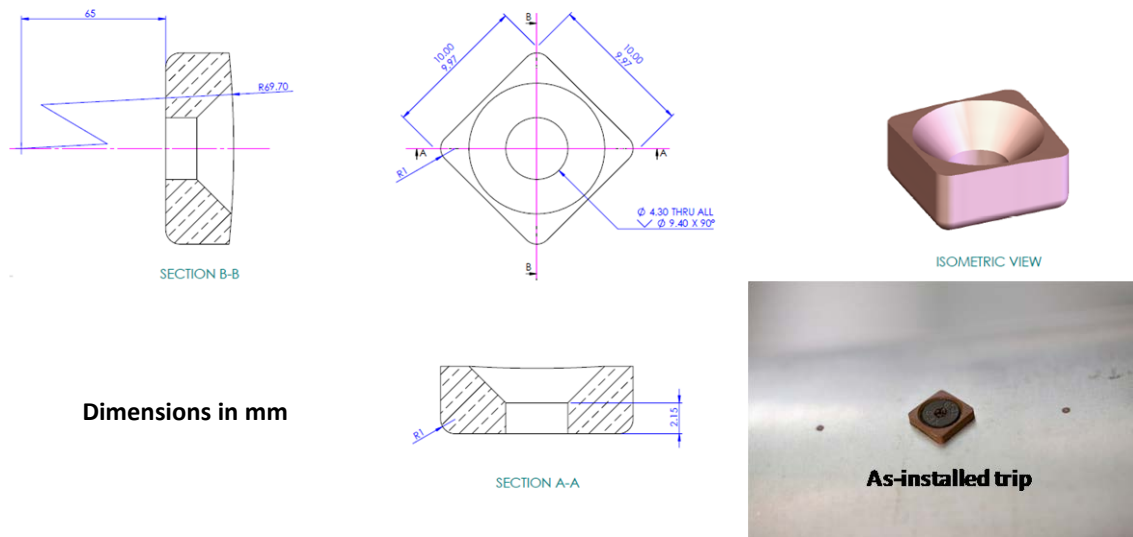


Figure 26 Boundary Layer Trip

Most of the rough side SBLI instrumentation was on TM stream 1, and this stream experienced high noise levels. Despite the high noise levels, trip effects could be extracted from these data. Figure 27 demonstrates the difference between rough-side and smooth-side transition. This figure shows data from Medtherm heat transfer gauges HT1 and HT2 on the smooth side, and HT6 and HT7 on the rough side. HT1 and HT6 were located at $x=0.90$ m and displaced 15 degrees from the primary thermocouple rays on their respective sides. HT2 and HT7 were located at $x=1.0$ m and displaced 30 degree from the primary thermocouple rays on their respective sides.

Some data points were displaced due to bit-shifts in the telemetry, and these points were removed. Figure 27 illustrates that the drop to laminar heat transfer occurred on the smooth side between 22 to 23 seconds for HT1 and HT2. Note that HT2 dropped to laminar about one second after HT1 since it was farther downstream. HT6 and HT7 did not register laminar heat transfer until $t=30$ seconds. The difference in transition time between these thermocouples is

not discernible, which is a reflection of the rapid movement typical of tripped transition. Both HT6 and HT7 showed heat transfer modulation due to the combination of vehicle spin and AoA.

The tripped side transitioned to fully laminar flow during ascent at $h=31.5$ km at $M=5.68$, with $Re_x=9 \times 10^5$. AoA at this time was 1 to 1.5 degrees. The trip was sized, based on wind tunnel tests,⁹ to be effective at a Reynolds number $Re_x=8 \times 10^5$ during descent at approximately 33 km at $M=7.2$. An effective trip is one which is large enough to move transition as close as possible to the roughness element.³⁵ This is contrasted with a “critical” trip, which is just large enough to affect transition. Since the heat transfer gauges are downstream of the roughness element, the trip at $t=30$ seconds is somewhat less than effective. However, given the rapid transition front movement observed in flight, there is probably a very little difference between critical and effective trips.

The intentionally tripped transition provided a test of the assertion that smooth-side transition after $t=19$ seconds was uninfluenced by the nose tip steps. The roughness Reynolds number, Re_{kk} of the large diamond trip at TL transition end, was approximately 2200.¹⁵ At $t=19$ seconds, when smooth-side transition appeared well-behaved and uninfluenced by any trips, Re_{kk} for the worst-case backward facing nose tip step ($k=2 \times 10^{-4}$ m at $x=0.1$ m) was approximately 700.¹⁵ This evidence further indicates that smooth-side transition for $t>19$ seconds was uninfluenced by the nose tip steps.

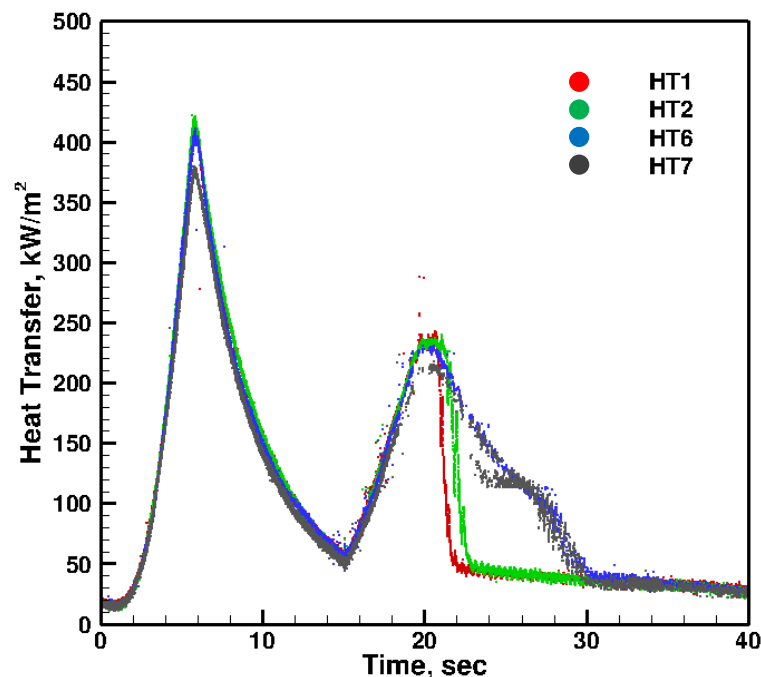


Figure 27 Comparison of rough-side to smooth-side heat transfer

5. Descent Phase Transition

The preliminary results given by Kimmel *et al.*¹⁶ provided a general description of the laminar-turbulent transition process during reentry. It was beyond the scope of this initial investigation to provide a more detailed description. This section expands upon the existing results providing a more detailed description of the three-dimensional, laminar-turbulent transition process during reentry of the HIFiRE-1 flight. Specifically, power spectra, cross-spectra, and correlation techniques were used to characterize surface pressure measurements, and investigate the periodic disturbances observed during laminar-turbulent transition. These techniques required the implementation of special methods to accurately describe the distortion caused by the unevenly spaced sampling scheme of the time series data collected during flight.²⁰ The results presented in this section utilized these methods to estimate power spectra of surface pressures measured underneath laminar, turbulent, and transitional boundary layers, and to determine the frequency, wavelength, and orientation of the periodic disturbances on the payload surface at different flight times. Other results in this section include spin rates and angles of attack, as functions of the flight time, and normalized root-mean-squared pressures mapped onto the Φ - Re plane.

For descent, the freestream conditions, p_∞ , T_∞ , M_∞ and Re , were obtained from the best-estimated trajectory. These estimated quantities are shown in Figure 28 and Figure 29. The relative uncertainties for p_∞ , T_∞ , M_∞ , ρ_∞ , Re , and U_∞ are 26.8%, 2.7%, 25.0%, 25.1%, and 0.8%, as determined from the BET. The uncertainties given are the maximum uncertainties corresponding to $t = 483.5$ seconds.

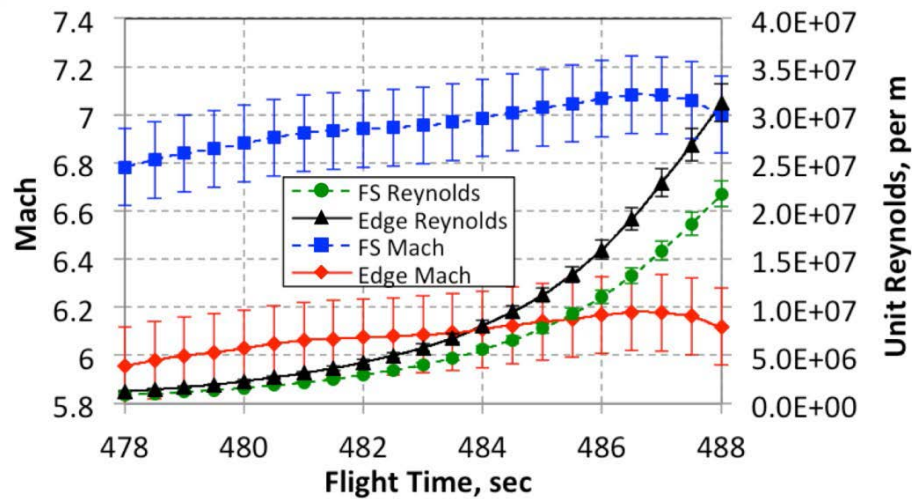


Figure 28 Descent Mach and Unit Reynolds Number

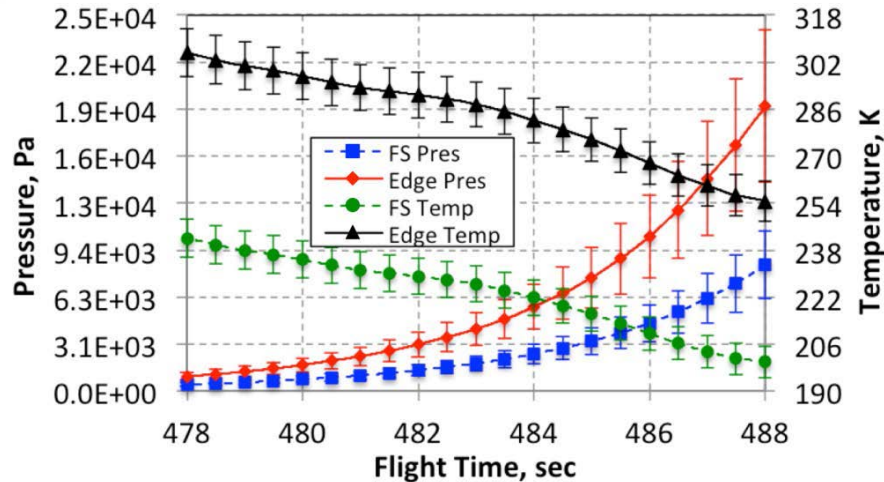


Figure 29 Descent Freestream Temperature and Pressure

The HIFiRE-1 GPS failed to provide data during flight. Although HIFiRE-1 contained several attitude measurement systems, including an IMU, magnetometer and horizon sensor, none of these instruments provided sufficient information or resolution to accurately determine the vehicle attitude with respect to the wind. Because of this, cone surface pressure measurements provided the best means to determine payload roll angle and AoA.

Surface pressure traces from four different stations located at body-fixed coordinates (0.7013 m, 55°), (0.7013 m, 325°), (0.9263 m, 10°), and (1.0513 m, 10°) are shown in Figure 30. These coordinates correspond to the transducers PLBW10, PLBW14, PLBW4, and PLBW5, respectively. As shown, the surface pressure traces were sinusoidal with troughs and crests corresponding to points on the leeward ray and the attachment line, respectively. Other pressure transducers recorded similar sinusoidal signatures. It should be noted that the leeside cone boundary layer would be expected to be separated for most of the period of interest.⁴⁰ The pressure traces in Figure 30 are consistent with a separated leeside boundary layer.⁴⁰ The pressure distributions in the vicinity of the lee meridian show a local peak, with local minima on either side. Pressure measurements recorded on cones at AoA by Stetson (Ref. 40) showed a similar shape near separation. Ref. 40 oil flow measurements showed that generally, the separation occurred inboard of the pressure minima, but the separation point could not be associated with any unique feature of the pressure distribution.

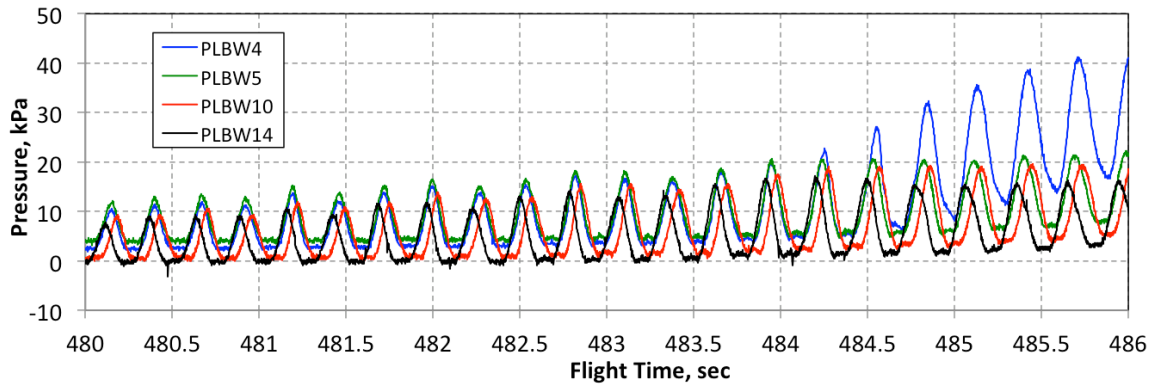


Figure 30 Surface Pressure Traces

The time coordinate of pressure measurements was mapped to a wind-fixed azimuthal coordinate by assuming the spin rate of the payload was constant during each 360° rotation, and by referencing the distinguishable, periodic attachment line and leeside ray pressures to $\Phi = 0^\circ$ or 360° , and $\Phi = 180^\circ$, respectively. The mapped azimuthal coordinates, designated as the roll angle, are shown in Figure 31 for the measurement times of pressure transducer PLBW3. The pressure trace of PLBW3 is shown for reference. As shown, the peaks in surface pressure corresponded to the attachment line, and were assigned a wind-fixed roll angle of 0 or 360 degrees. The troughs in the surface pressure correspond to the leeside ray, and were assigned a wind-fixed roll angle of 180 degrees. This mapping of wind-fixed roll angles to measurement times was used to map measurements of other transducers mounted along the same cone ray as PLBW3 ($\phi = 10^\circ$). Similar roll angle mappings were determined from the pressure traces from stations located on the 55 and 325 degree cone rays. The mapping of measurements recorded by transducers located at ϕ -coordinates other than 10° , 55° , and 325° was done by (1) interpolation, and (2) the spin rates. The results obtained from interpolation or using the spin rates were similar.

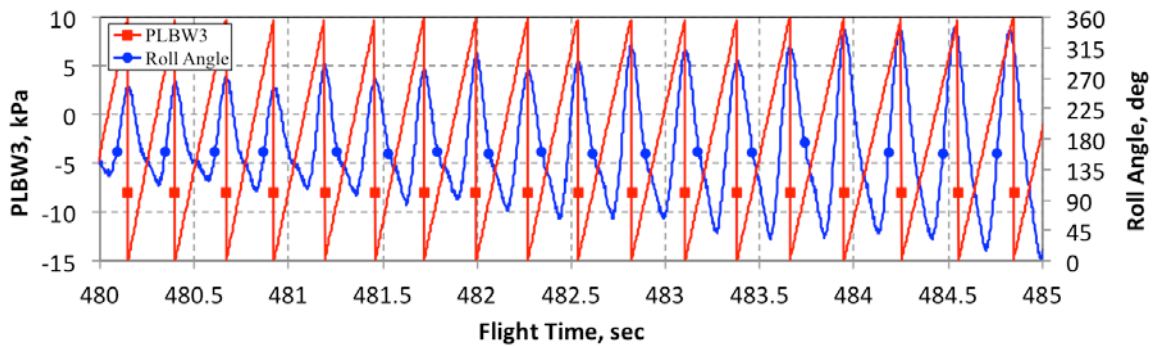


Figure 31 Roll Angle and PLBW3 Pressure Trace Versus Flight Time During Reentry

The spin rate was determined from surface pressure traces by two methods: (1) inverting the period of the roll angle and (2) computing the Fourier transform from a moving time window. The relative uncertainty for the spin rate was estimated at 6.0%, and was determined from the uncertainty of the pressure transducer and the time step of the pressure trace. The results from Methods 1 and 2 are shown in Figure 32. Both methods produce a similar spin rate. The differences between the results from Methods 1 and 2 are likely due to using the broadband

signal (Method 1) versus using the decomposed signal at the spin rate frequency (Method 2). From Figure 32, it is apparent that the spin rate is not constant as was assumed when determining the roll angle; however, the maximum change in the spin rate for any 360 degree rotation of the payload is ~ 0.09 degrees/sec or $\sim 2\%$, which has a minor effect on the roll angles presented in Figure 31.

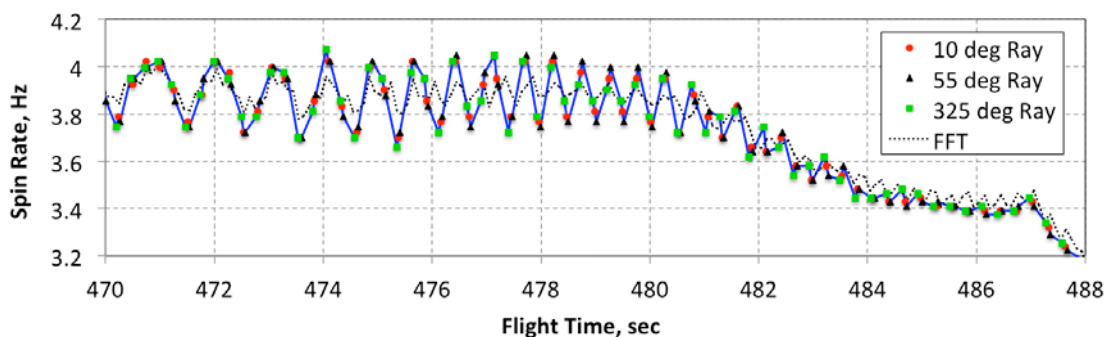


Figure 32 Spin Rate Versus Flight Time During Reentry

The total AoA during reentry was estimated indirectly from surface pressure traces recorded at stations located at body-fixed coordinates (1.0513 m, 10°) and (0.7013 m, 55°). It was assumed that changes in surface pressure during one 360 degree rotation of the payload were caused by changes in total AoA. The total AoA (α) was determined using two different methods. The first method, designated as Method 1, estimates α indirectly by comparing a measured surface pressure trace with surface pressure traces predicted at $\alpha = 0, 5, 8, 10, 12, 15$, and 18 degrees. The pressure traces were obtained from Navier-Stokes computations. The total AoA was estimated by interpolating the measured pressure trace with two bounding numerical pressure traces. The second method, designated as Method 2, is similar to Method 1, but determines α by comparing a measured pressure trace with pressure traces measured in a wind tunnel at different α values. The total AoA determined using Methods 1 and 2 are shown in Figure 33 and Figure 34. As shown, the results obtained from Method 1 are very similar to the results obtained from Method 2, providing a check of the accuracy of the theoretical traces. Due to this good agreement, and because Method 1 yields higher fidelity estimates of α , the α values referred to within this paper were obtained from Method 1. A scatter on the order of $\pm 3^\circ$ was estimated by comparing the results determined from the two measurement stations. The scatter is less for the times during transition.

Comparing α in Figure 33 to the spin rate in Figure 32 shows that both quantities are damped, sinusoidal functions with the same instantaneous frequency.

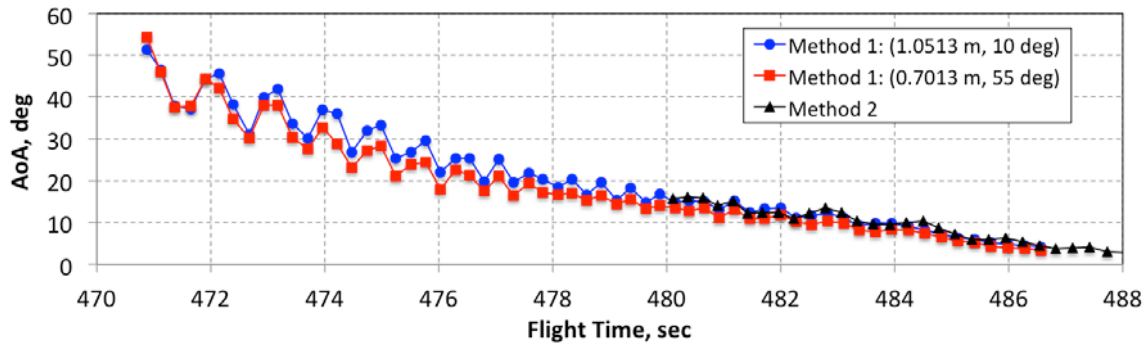


Figure 33 Total AoA Versus Flight Time During Reentry

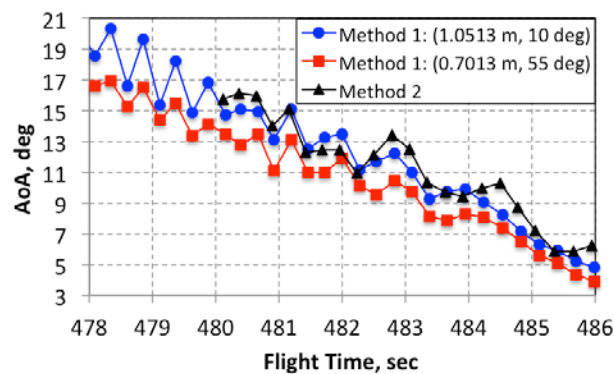


Figure 34 Total AoA Versus Flight Time During Laminar-Turbulent Transition

Surface temperature traces were normalized using the adiabatic wall temperature, as shown in Figure 35. The traces shown are from four different stations corresponding to the furthest upstream and downstream stations along the 0° and 270° rays. The body-fixed coordinates for these stations are $(0.3013 \text{ m}, 0^\circ)$, $(1.0513 \text{ m}, 0^\circ)$, $(0.5013 \text{ m}, 270^\circ)$, and $(0.9013 \text{ m}, 270^\circ)$. As shown, the normalized temperature traces have similar amplitude envelopes as the surface pressure traces shown in Figure 31 due to payload spin at AoA. The normalized temperatures were less than 0.19 during transitional flow, corresponding to a cold wall boundary condition.

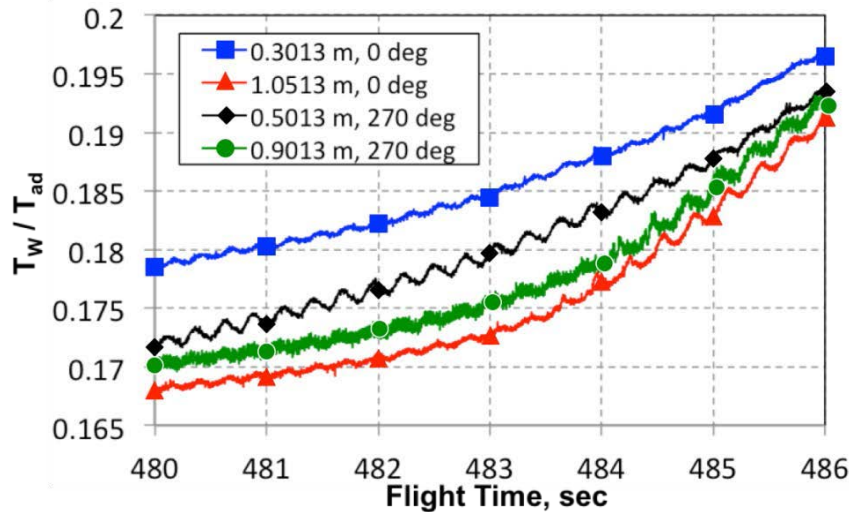


Figure 35 Normalized Surface Temperatures Versus Flight Time

The combination of vehicle spin and AoA on HIFiRE-1 during reentry requires careful examination of the data to extract meaningful transition results. It is well known that a cone at AoA experiences a three-dimensional transition front, with the axial transition location varying with the azimuthal coordinate. Thermographic phosphor images taken in preflight testing of transitional heat transfer on HIFiRE-1 at AoA illustrate this.¹³ Two related issues, the effect of the spin on the transition front, and the response of transducers must be addressed.

The maximum spin rate observed during reentry, 4 Hz, equates to a tangential velocity of less than 4 m/s at the downstream end of the cone. The missile velocity at this time was over 2090 m/s. Since the tangential velocity was less than 0.2 percent of the freestream velocity, it is unlikely that the missile spin had any significant fluid dynamic effect on transition. This supposition is further supported by wind tunnel tests conducted on a 9 degree half-angle spinning cone.³² In these tests, carried out at Mach 5 and 8, comparison of transition data on a spinning cone and a stationary cone showed no skewing of the transition front, at spin rates up to 6000 degrees/s (16.7 Hz roll rate) and angles of attack up to 6 degrees. It is evident from this experiment that the transition front on a spinning cone under these conditions is wind-fixed. It should be noted that this conclusion applies to smooth-body transition, and not necessarily to roughness-induced transition.

In the case of wind-fixed transition on a spinning cone at AoA, a transducer in the transitional zone can experience multiple transits in and out of turbulent flow during each spin revolution. It is clear that if the transducer does not possess sufficient frequency response, the transition from laminar-to-turbulent flow and vice versa will be smeared out, and perhaps unresolvable. This was demonstrated in wind tunnel experiments cited above. It will be shown that on HIFiRE-1 the thermocouples could not register the detailed 3D transition front, however, they could measure an average transition location. Higher bandwidth transducers, like Kulite pressure transducers and Vatell heat transfer gauges, had ample frequency response to resolve multiple turbulent-laminar and laminar-turbulent transitions during a spin revolution.

The average onset time for transition was inferred from front face temperature traces by noting when in time the rate of change in temperature increased.

The combination of vehicle spin and AoA on HIFiRE-1 during reentry requires careful examination of the data to extract meaningful transition results. It is well known that a cone at AoA experiences a three-dimensional transition front, with the axial transition location varying with the azimuthal coordinate. Thermographic phosphor images taken in preflight testing of transitional heat transfer on HIFiRE-1 at AoA illustrate this.¹³ Two related issues, the effect of the spin on the transition front, and the response of transducers must be addressed.

The maximum spin rate observed during reentry, 4 Hz, equates to a tangential velocity of less than 4 m/s at the downstream end of the cone. The missile velocity at this time was over 2090 m/s. Since the tangential velocity was less than 0.2 percent of the freestream velocity, it is unlikely that the missile spin had any significant fluid dynamic effect on transition. This supposition is further supported by wind tunnel tests conducted on a 9 degree half-angle spinning cone.³² In these tests, carried out at Mach 5 and 8, comparison of transition data on a spinning cone and a stationary cone showed no skewing of the transition front, at spin rates up to 6000 degrees/s (16.7 Hz roll rate) and angles of attack up to 6 degrees. It is evident from this experiment that the transition front on a spinning cone under these conditions is wind-fixed. It should be noted that this conclusion applies to smooth-body transition, and not necessarily to roughness-induced transition.

In the case of wind-fixed transition on a spinning cone at AoA, a transducer in the transitional zone can experience multiple transits in and out of turbulent flow during each spin revolution. It is clear that if the transducer does not possess sufficient frequency response, the transition from laminar-to-turbulent flow and vice versa will be smeared out, and perhaps unresolvable. This was demonstrated in wind tunnel experiments cited above. It will be shown that on HIFiRE-1 the thermocouples could not register the detailed 3D transition front, however, they could measure an average transition location. Higher bandwidth transducers, like Kulite pressure transducers and Vatel heat transfer gauges, had ample frequency response to resolve multiple turbulent-laminar and laminar-turbulent transitions during a spin revolution.

The average onset time for transition was inferred from front face temperature traces by noting when in time the rate of change in temperature increased. An example of onset transition times inferred from wall temperature traces recorded at stations (0.7013 m, 0°) and (1.0013 m, 0°) is shown in Figure 36. The onset transition times are inferred from the change in slope of the dashed lines. Measurements from station (1.0013 m, 0°) drifted, but were still useful in determining transition onset. The transition onset times inferred from all available thermocouple and heat transfer measurement stations are shown in Figure 37. The azimuthal coordinates indicated in the legend correspond to a body-fixed coordinate system. As shown, laminar-turbulent transition was detected initially on the aft end of the cone, at $Re = 4.8 \times 10^6 \pm 1.2 \times 10^6/m$, and then propagated upstream to $x = 0.5$ meters as Re increased to $Re = 11.9 \times 10^6 \pm 3.0 \times 10^6/m$.

Measurements from stations located at $x < 0.5$ meters remained laminar through the end of telemetry. The transition front swept upstream gradually which is indicative of a natural transition process. The transition Reynolds number was determined as $Re_x = 4.87 \times 10^6 \pm 1.2 \times 10^6$ and represents an average of the transition Reynolds numbers at each station shown in Figure 37. The standard deviation was 0.59×10^6 . The curve designated as “average Re” corresponds to the average transition Reynolds number. The dashed lines correspond to two standard deviations. As shown, an average transition Reynolds number fits the data well. The response times of the low bandwidth heat transfer and thermocouple gauges was too slow to resolve the azimuthal variation in the transition front. The transition times in Figure 37 thus represent an average transition time at a given x -station.

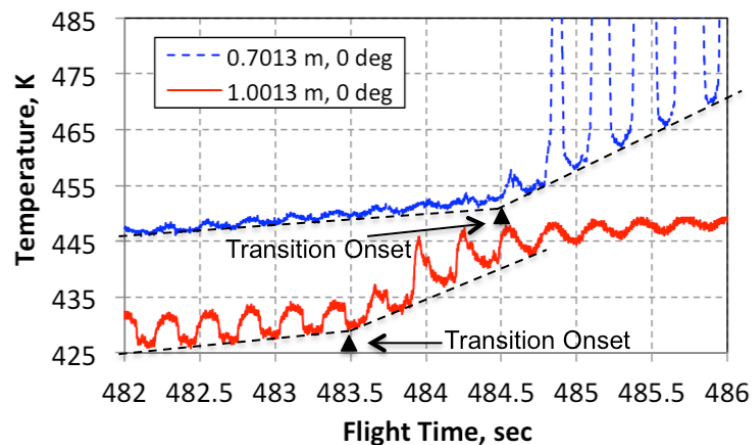


Figure 36 Transition Onset Times Inferred From Surface Temperature Traces

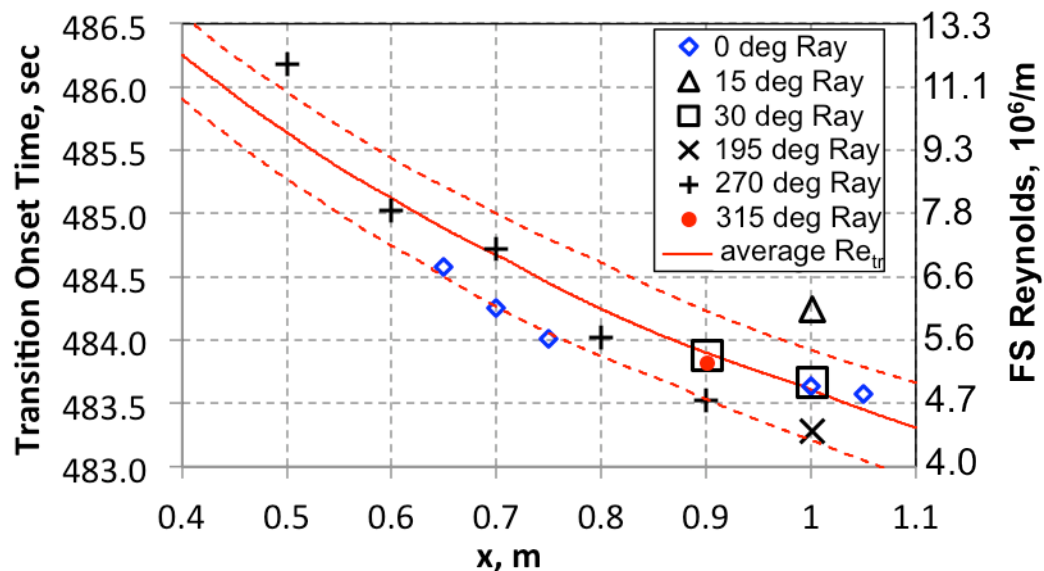


Figure 37 Transition Onset Times Along Different Cone Rays

Since the 3D transition front moved from the aft portion of the vehicle forward, a given transducer during each spin revolution would transit a different portion of the transitional zone. With each successive revolution, the transducer would spend a greater portion of that revolution immersed in turbulent flow, until the transition front had progressed fully over it, and the entire revolution was spent beneath turbulent flow. This variation in the transition front permits a kind of pseudo-map to be constructed showing the azimuthal transition location as a function of local Reynolds number (to be discussed later). The sample rates of the high-bandwidth instrumentation were sufficient to capture interesting features from this transient process that were not detectable from the low-bandwidth instrumentation. These features are labeled in the heat transfer trace shown in Figure 38, from HT3 located at (0.9013 m, 30°). Some of the interesting features are labeled in the figure including (a) laminar heating rates on the attachment line ($\Phi = 0^\circ$), (b) heating rates underneath a separated boundary layer, (c) periodic disturbances in the heating rates on the payload shoulders, (d) laminar-turbulent breakdown of periodic disturbances, and (e) attachment line transition. The labels (f) through (h) in Figure 38 show the intermittency of the laminar-turbulent transition process as HT3 transits beneath laminar and turbulent regions. Specifically, the azimuthal span of the turbulent boundary layer on the shoulder and on the attachment line expand circumferentially until merging, resulting in a turbulent boundary layer around the entire circumference of the payload.

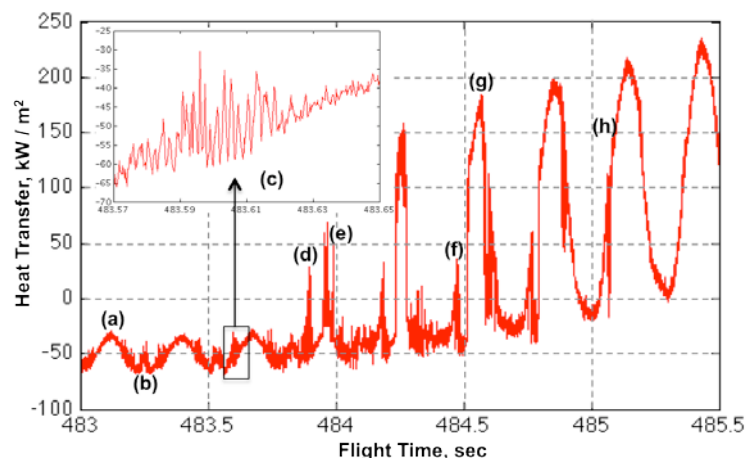


Figure 38 Heat Transfer Trace From the Measurement Station (0.9013 m, 15°)

The features in the heat transfer trace and morphology of the boundary layer transition process were measured with better signal-to-noise levels and higher frequency resolution by transducers PHBW1, PHBW2, and PHBW3, located at body-fixed coordinates of (0.8513 m, 10°), (0.8563 m, 10°), and (0.8513 m, 15°), respectively. A fluctuating pressure trace from PHBW1 is shown in Figure 39 for one full rotation of the payload. The fluctuating pressure trace in Figure 39 was digitally high-pass filtered at a cutoff frequency of 100 Hz to remove low-frequency content that passed through the onboard analog high-pass filter. The periodic, fluctuating pressure trace shown in Figure 39 was observed repeatedly in the time traces measured by each high bandwidth transducer (PHBW1, PHBW2, PHBW3, and HT3). Specifically, the periodic fluctuations were observed twenty three times in each high

bandwidth pressure trace during the 5 seconds of laminar-turbulent transition. High bandwidth data before and after this 5 second window corresponded to measurements underneath a laminar and turbulent boundary layer, respectively. The periodic traces were not observed when the boundary layer was laminar, and did not persist long in what was interpreted as a turbulent boundary layer. The root mean square (RMS) pressure shown in Figure 39 was normalized with the mean surface pressure. The features in the fluctuating pressure trace are correlated to the structures in the normalized RMS, as shown in Figure 39. The RMS pressure was normalized with the local mean surface pressure. Fluctuating pressure trace was from station (0.8513 m, 10°) and the mean surface pressure trace was from station (0.9263 m, 10°). The autospectrum of the laminar, transitional, and turbulent pressure fluctuation traces, labeled as (1), (2), and (3) in Figure 39, are shown in Figure 40, and were computed using the method described in Ref. 20. The noise floor in this figure corresponds to the autospectrum of exoatmospheric data. The uncertainty levels in power are large due to the short time traces; however, the autospectral densities computed still illustrate important spectral characteristics of the laminar, transitional, and turbulent pressure traces. In particular, turbulent power levels are around four orders of magnitude greater than laminar levels, but are substantially lower than transitional levels for $f < 600$ Hz. The transitional power levels roll off rapidly and merge with the laminar and noise floor levels at about $f = 2.5$ kHz. The turbulent power levels are fairly constant until about $f = 7$ kHz, and then roll off to about two orders of magnitude greater than the noise floor levels at $f = 20$ kHz. The different spectral characteristics of the contributions from the transitional and turbulent fluctuations to the broadband fluctuating pressure will be shown later to be useful for separating these contributions.

The contour plot of the normalized RMS pressures on the Φ - Re plane for PHBW1 is shown in Figure 41. The dashed line in Figure 41 shows the part of the contour plot corresponding to the time trace in Figure 39. The periodic pressure fluctuations correspond to two regions labeled as (2) in Figure 39. These fluctuations correspond to the area enclosed by the diamonds in Figure 41. The location of the attachment line transition front is indicated by the triangles, and squares indicate the local leeside pressure minima. As shown in Figure 39 and Figure 41, the normalized RMS levels of the periodic and turbulent fluctuations are similar, making it difficult to distinguish between the two. It was found useful to separate the normalized RMS into its lower and higher frequency contributions. Contributions from higher frequencies were determined by computing the area underneath the autospectral density function for $f > 4$ kHz. This sum is designated as the normalized high-frequency RMS, (RMS/P). Contributions from lower frequencies were determined by computing the area underneath the autospectral density function for $f < 1$ kHz. This sum is designated within this paper as the normalized low-frequency RMS, (RMS/P).

The amplitude, azimuthal span, and frequency of these periodic, fluctuating pressure signatures changed as the vehicle descended. The change in amplitude and azimuthal span can be observed in the contour plots of the normalized low-frequency RMS on the Φ - Re plane, as shown in Figure 42(a), Figure 43(a), and Figure 44(a). In Figure 42, diamonds indicate the start and end of periodic disturbances. In Figures 43 and 44, regions of periodic disturbances are enclosed in (a), and the transition front is outlined in (b). The azimuthal extent and time duration of the periodic disturbances are summarized in Figure 45. There are

two regions enclosed on the contour plots corresponding to the periodic disturbances. These regions are sharply circumscribed, lying between about $50 \leq \Phi \leq 90$ degrees and $225 \leq \Phi \leq 300$ degrees. The periodic disturbances are first evident in the pressure signals at about $t = 481.3$ seconds. The Reynolds number is about $2.0 \times 10^6 \pm 5.0 \times 10^5$. This region grows in azimuthal extent until a Reynolds number of about $3.0 \times 10^6 \pm 7.5 \times 10^5$. At this point the inboard extent of this region is sharply circumscribed by the pressure minima. The relative fluctuation level increases with Reynolds number until reaching a maximum at $Rex = 3.2 \times 10^6$ to $3.6 \times 10^6 \pm 9.0 \times 10^5$. The angle of attack was $\sim 13 \pm 3^\circ$ when the periodic disturbances were first evident, and had decreased to $\sim 9 \pm 3^\circ$ when the normalized low-frequency RMS reached a maximum level. The fluctuation level corresponding to this maximum level in the normalized low-frequency RMS is $3.1 \pm 0.4\%$. This local maximum corresponds to the maximum amplitude reached by the periodic fluctuations.

The windward boundary of the periodic fluctuations continues to expand toward the windward meridian of the vehicle until $Rex = 4.0 \times 10^6 \pm 1.0 \times 10^6$. As Reynolds number increases beyond this value, the windward extent of the region remains at about 45 degrees on either side of the windward meridian. Transition begins to propagate outward from the lee side of the vehicle and serves as a lee-side limit to the region with periodic fluctuations. This region has become largely turbulent by $Rex = 5.6 \times 10^6 \pm 1.4 \times 10^6$, as shown by the normalized high-frequency RMS contour plots in Figure 42, Figure 43, and Figure 44. The results from HT3 are included in Figure 42, and are in agreement with the PHBW transducers. The diamond markers correspond to periodic fluctuations in the heat transfer.

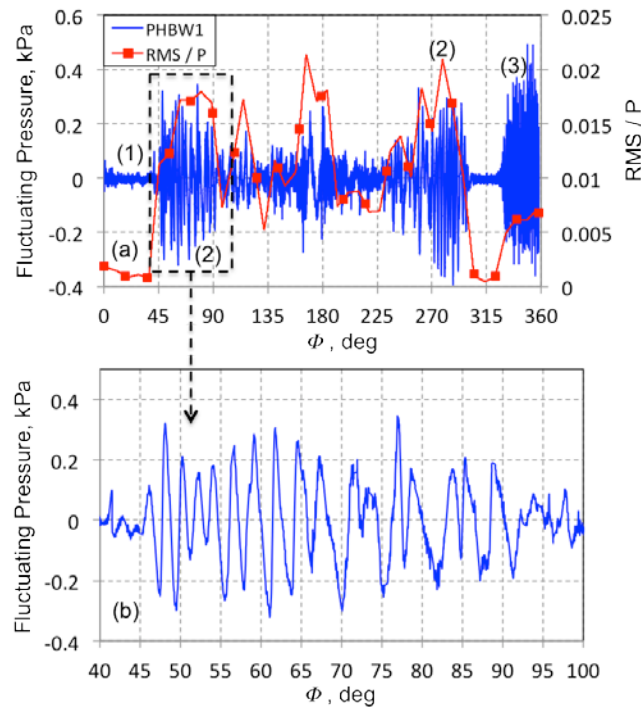


Figure 39 Fluctuating Pressure and Normalized RMS Pressure for One Full Rotation (Top) and Periodic Waves in the Fluctuating Pressure Trace (Bottom)

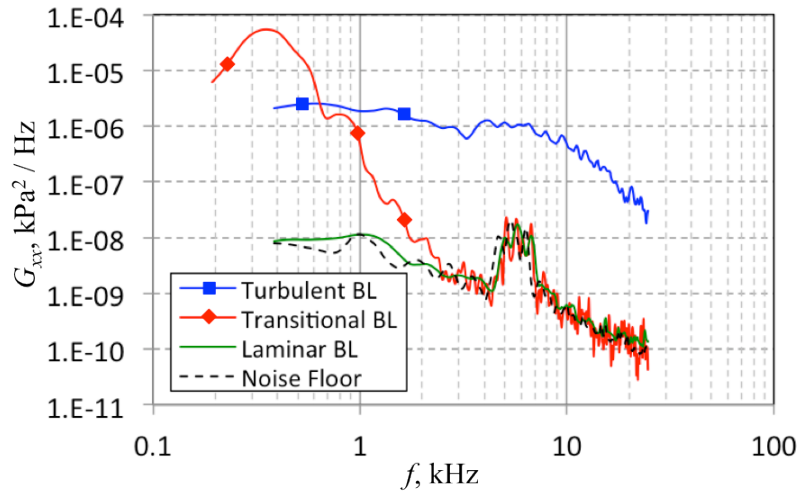


Figure 40 Autospectral Density Function for Pressure Fluctuations Underneath Laminar Boundary, Transitional Boundary Layer, and Turbulent Boundary Layer

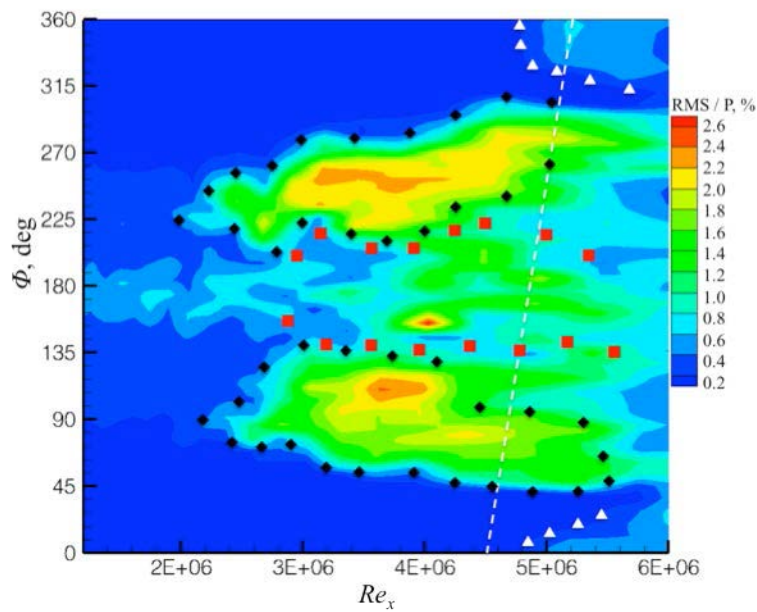


Figure 41 Contour Plot of Normalized RMS Surface Pressures Mapped Onto the ϕ - Re Plane

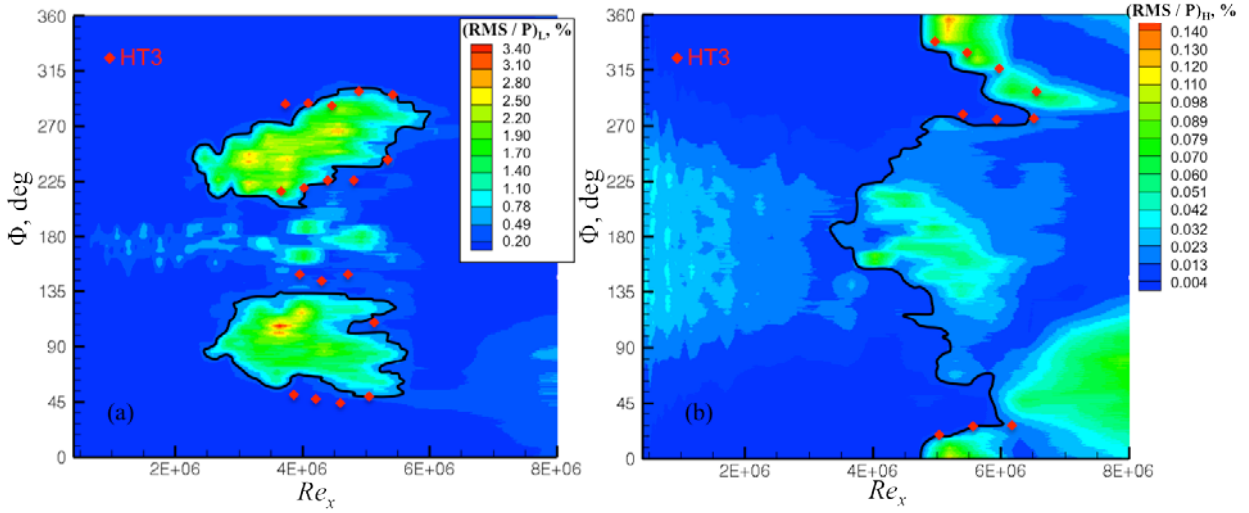


Figure 42 Contour Plots of (a) Normalized Low-Frequency RMS, and (b) Normalized High-Frequency RMS of PHBW1/PLBW4

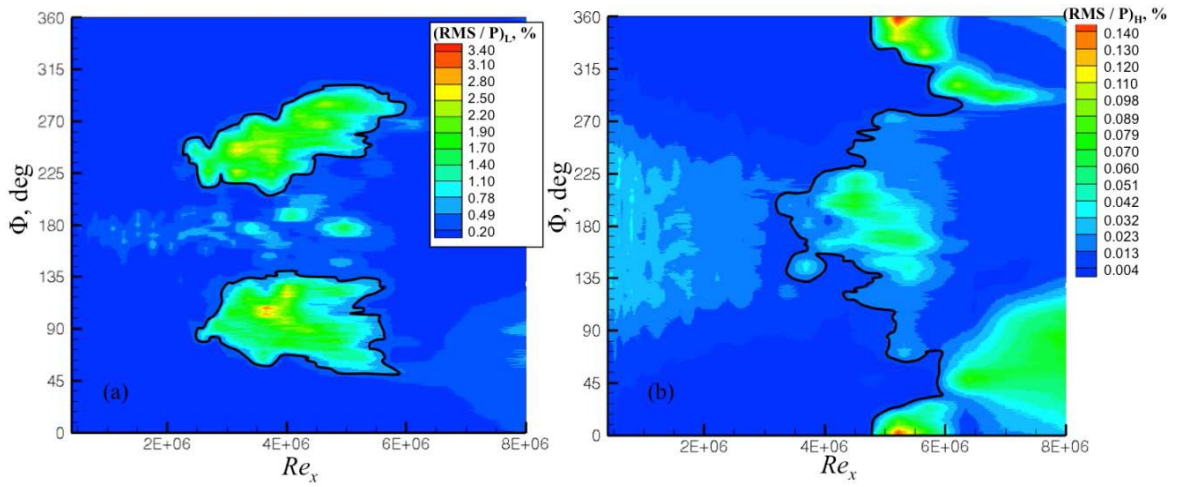


Figure 43 Contour Plots of (a) Normalized Low-Frequency RMS of PHBW2/PLBW4, and (b) Normalized High-Frequency RMS of PHBW2/PLBW4

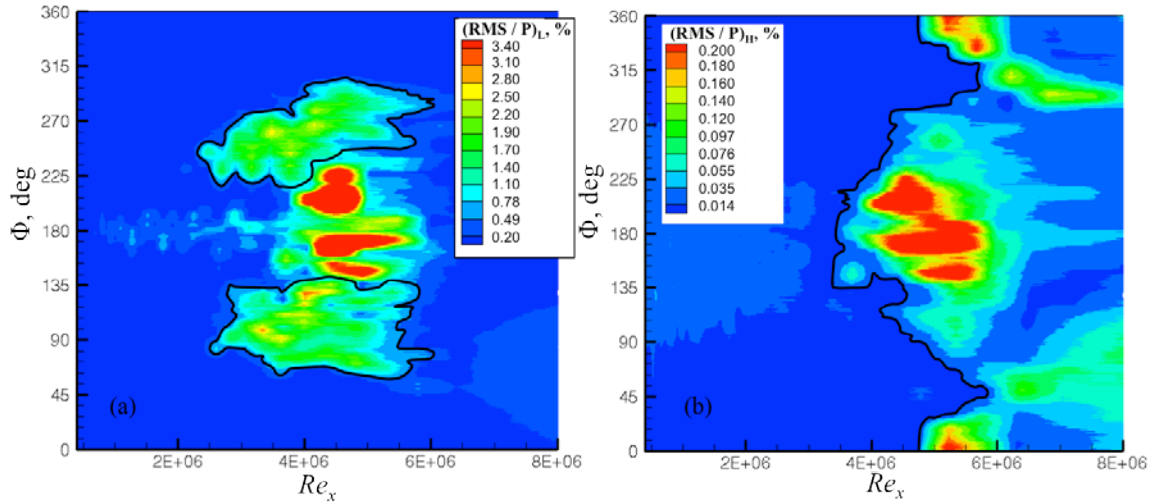


Figure 44 Contour Plots of (a) Normalized Low-Frequency RMS of PHBW3/PLBW4, and (b) Normalized High-Frequency RMS of PHBW3/PLBW4

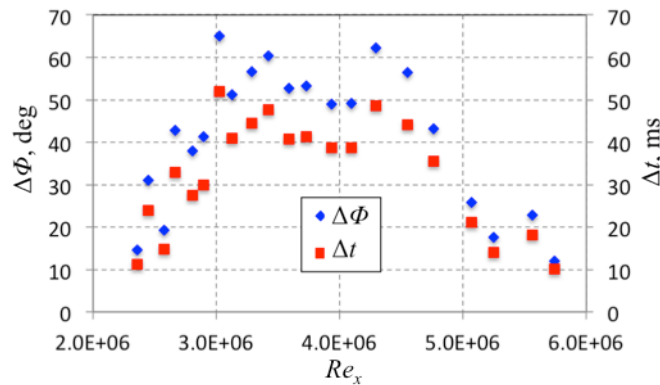


Figure 45 Azimuthal Extent of Shoulder Disturbances, $\Delta\Phi$, and Duration in Time, Δt , With Respect to Re_x

The autospectral density function of the first eleven periodic traces lying between $50 < \Phi < 90$ degrees, and for the first ten periodic traces lying between $225 < \Phi < 300$ degrees, are shown in Figure 46 and Figure 47, respectively. The autospectra shown was computed from the normalized fluctuating pressure traces of PHBW2 (0.8563 m , 10^0). The disturbances recorded at stations PHBW1 and PHBW3 featured similar spectral features. The time intervals of the disturbance traces were short, ranging from 10 to 50 ms, and included only 10 to 25 periodic disturbances per trace. This limited the frequency resolution to 25 to 115 Hz, and resulted in higher variance in the estimated autospectra than desired. Despite these limitations the spectra provided important information about the development of the disturbances. As shown, the autospectral density function featured a single, low amplitude peak centered at about 270 Hz at $Re_x = 2.38 \times 10^6$. The amplitude and frequency of this peak increased as Re_x increased to 2.60×10^6 . A second peak centered at 570 Hz developed once Re_x increased to $Re_x = 2.84 \times 10^6$.

The amplitude of the first peak reached a maximum at $Re_x = 3.06 \times 10^6$ which corresponds to the maximum in the normalized low-frequency RMS. The amplitudes of the first peak decreased while the second peak increased as Re_x increased. The amplitude of the second peak (centered at 570 Hz) reached an amplitude similar to the first peak by $Re_x = 3.98 \times 10^6$. The amplitude of the first peak decreased rapidly as Re_x increased beyond 3.98×10^6 , whereas, the amplitude of the second peak decreased at a slower rate. By $Re_x = 5.12 \times 10^6$, the first peak was no longer detectible. The amplitude of the second peak was significantly reduced by $Re_x = 5.29 \times 10^6$, and the full width at half maximum increased from 100 Hz to 400 Hz. This broadening of the second peak occurred with an increase in power levels at frequencies up to the maximum resolvable frequency of the transducer (24.9 kHz), and corresponded to the beginning of turbulent breakdown of the disturbances. This correlates to the end of the periodic disturbances indicated in the normalized low-frequency RMS contours (Figure 42, Figure 43 and Figure 44). The properties of the disturbance traces from $50 < \Phi < 90$ degrees and $225 < \Phi < 300$ degrees vary with Φ . The boundary layer is thinner at $\Phi = 50$ and 225 degrees than at $\Phi = 90$ and 300 degrees. The frequency of the disturbances is at a maximum at the beginning of the trace and then shifts to lower frequencies, as shown in Figure 48 for the disturbance trace at $Re_x = 3.06 \times 10^6$. The autospectrum in Figure 48 corresponds to the Fourier transform of a 0.01 second window moved 0.005 seconds through the time window $483.99 < t < 484.06$ seconds. The spectrum features a single peak between $52 < \Phi < 75$ degrees. An additional peak appears between $75 < \Phi < 90$ degrees. The disturbances at the beginning of the time trace are sinusoidal, but are complex periodic later in the trace. In summary, these disturbance traces represent nonstationary time series data, and the results shown in Figure 46 and Figure 47 represent the sum contribution of the entire trace.

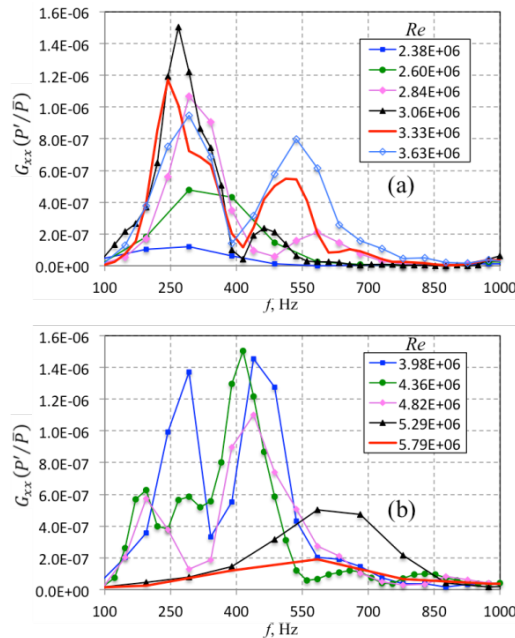


Figure 46 Autospectral Density Function of Periodic Disturbances Lying Between $50 < \Phi < 90$ Degrees at Station (0.8513 m, 10^0)

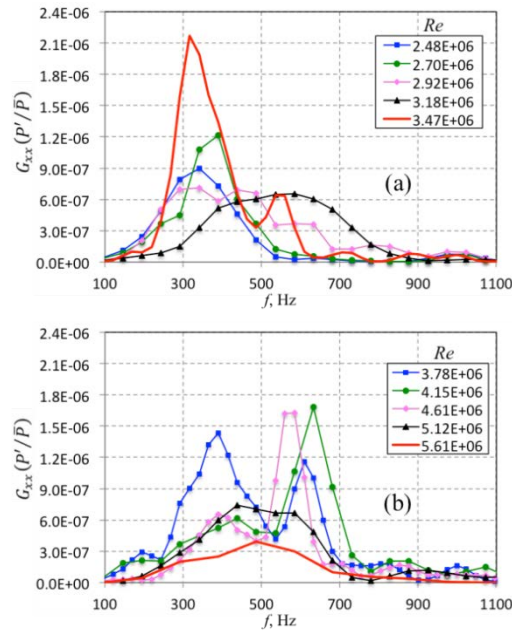


Figure 47 Autospectral Density Function of Periodic Disturbances Lying Between $200 < \Phi < 280$ Degrees at Station $(0.8513 \text{ m}, 10^0)$

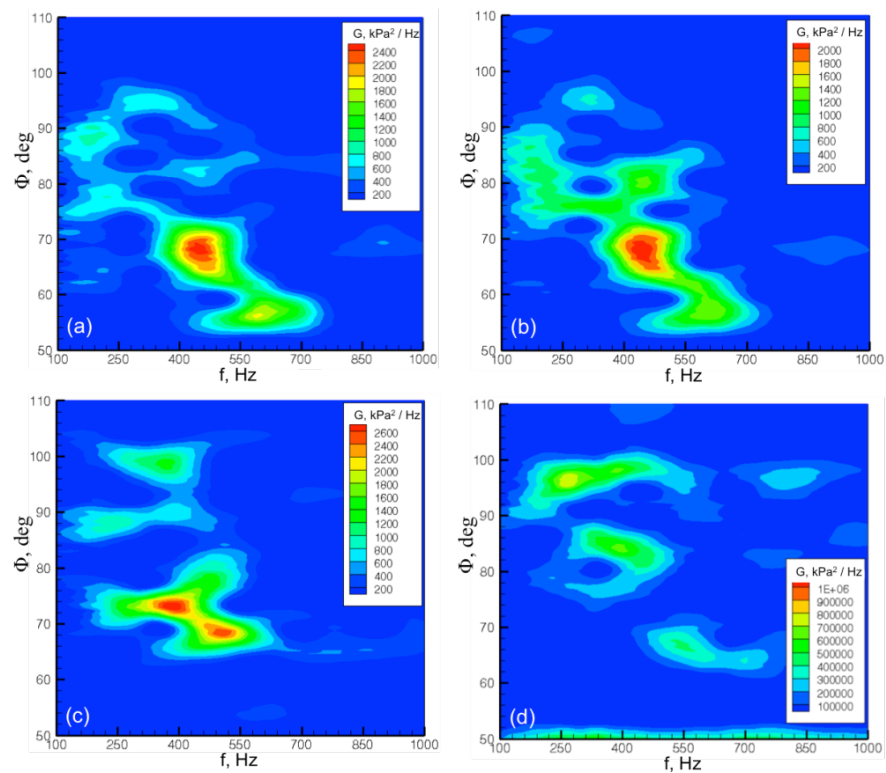


Figure 48 Power Spectra Contours In the Wind-Fixed Azimuthal Coordinate System for (a) PHBW1, (b) PHBW2, PHBW3, and (d) HT3

The three dimensional transition front can be observed in the contour plots of the normalized high-frequency RMS on the Φ - Re_x plane, as shown in Figure 42, Figure 43, and Figure 44. As shown, the transition Reynolds number is dependent on the wind-fixed azimuthal coordinate. The smallest and largest transition Reynolds number of $3.1 \times 10^6 \pm 8.0 \times 10^5$ and $6.0 \times 10^6 \pm 1.5 \times 10^6$ occurred along the leeside meridian and the 280 degree ray, respectively. The corresponding angles of attack were $13 \pm 3^\circ$ and $8 \pm 3^\circ$. Transition on the leeside spread rapidly in Φ as Re_x increased and α decreased until merging with the periodic disturbances on the shoulders, at $Re_x = 4.0 \times 10^6 \pm 1.0 \times 10^6$, $\alpha = 9 \pm 3^\circ$, and $\Phi = 135^\circ$ and 225° . Fluctuating pressure levels on the leeside peaked at 2.4% at $Re_x = 4.1 \times 10^6 \pm 1.0 \times 10^6$, and $\Phi = 155^\circ$, but averaged around 1.6% after transition. Transition on the attachment line started at $Re_x = 4.7 \times 10^6 \pm 1.2 \times 10^6$ at $\alpha = 9 \pm 3^\circ$, and spread azimuthally as Re_x increased and α decreased until merging with the transition front on the shoulders at $Re_x = 6.0 \times 10^6 \pm 1.5 \times 10^6$ and $\Phi = 30^\circ$ and 280° . The locations where the leeside and shoulder transition fronts merged, $\Phi = 135^\circ$ and 225° , was symmetric about the leeside meridian; however, the location where the attachment line and shoulder transition fronts merged, $\Phi = 30^\circ$ and 280° , were asymmetric. The fluctuating pressure level on the attachment line peaked at 1.2% behind the transition front at $Re_x = 5.1 \times 10^6 \pm 1.3 \times 10^6$, $\alpha = 9 \pm 3^\circ$ and $\Phi = 355^\circ$. The boundary layer was turbulent for $Re_x > 6.0 \times 10^6 \pm 1.5 \times 10^6$ around the circumference of the cone. Similar transition fronts have been obtained from wind tunnel experiments for cones at angle of attack.⁴⁰

The results reported in Figure 42, Figure 43, and Figure 44, corresponding to PHBW1, PHBW2, and PHBW3, are compared in Figure 49. Results from HT3 are also included. As shown, the results for the periodic disturbances obtained from the four different transducers are consistent. The results obtained from PHBW1 and PHBW2 are almost identical due to the close proximity of these transducers, whereas, the results from PHBW3 are slightly different. The filled diamond markers correspond to the onset and end times of the periodic fluctuations, and the open diamond markers are the onset and end times of the leeside fluctuations. The results for the transition front are compared in Figure 49. The average transition Reynolds number obtained from the low bandwidth data (depicted in the figure as Re_{tr}) is in excellent agreement with the transition Reynolds number obtained from the high bandwidth data. In fact, the transition Reynolds number of the low bandwidth data is almost identical to the average of the transition Reynolds number of the high bandwidth data with Φ .

The comparison shown also includes wind tunnel results from the H2K facility for a 64% scaled HIFiRE-1 model at Reynolds numbers, angles of attack, and Mach numbers similar to the flight conditions.^{41,42} The bluntness of the nosetips tested were 1.6 and 2.5 mm. The 2.5 mm bluntness matched the full-scale flight vehicle. The wall temperature of the H2K experiments was 0.56, which is greater than the flight experiment (0.18). The wind tunnel experiment featured PCB surface pressure measurements along the 0, 45, 90, 135, and 180 degree rays, and infrared thermography images of the leeside, windward side, and cone shoulder. The transition front measurements for $\alpha = 6^\circ$ and 12° are included in Figure 49(b) since these angles bound the angles-of-attack encountered in the flight experiment. Surprisingly, the transition Reynolds numbers from the wind tunnel experiment were slightly higher than the transition Reynolds numbers from the flight experiment.

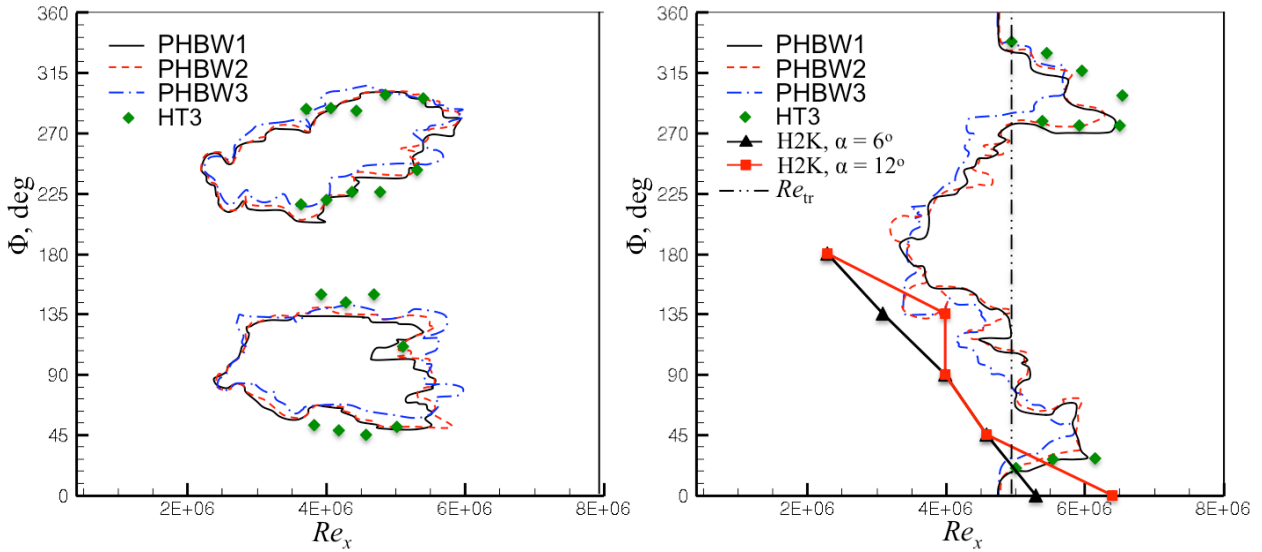


Figure 49 Comparison of the PHBW1, PHBW2, PHBW3, and HT3 Results for (a) Periodic Disturbances, and (b) Transition Front

It is interesting to note that regions of periodic disturbances overlapped with the transition front. These regions are labeled as “Breakdown of disturbances” in Figure 50. The turbulent and periodic structures were observed to coexist after transition. Similar regions were observed in the heat transfer measurements of HT3, as shown in Figure 51. The marker designating turbulent, periodic disturbances in Figure 51 corresponds to label “d” in the time trace shown in Figure 38. As shown in the time trace, the disturbances labeled “d” have much higher heating rates than the disturbances labeled “c”. The higher heating rates are due to turbulent breakdown of the disturbances.

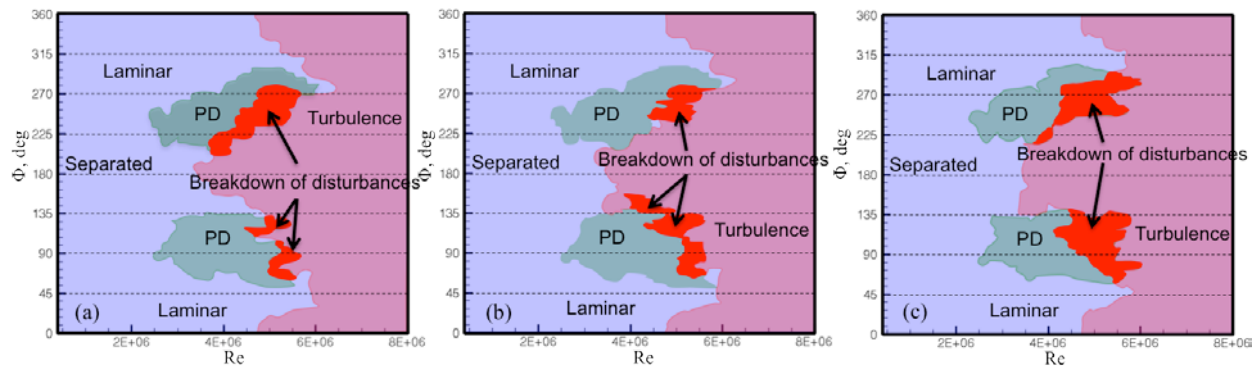


Figure 50 Contour Plots Depicting Location of Turbulent Breakdown of Periodic Disturbances on (a) PHBW1, (b) PHBW2, and (c) PHBW3

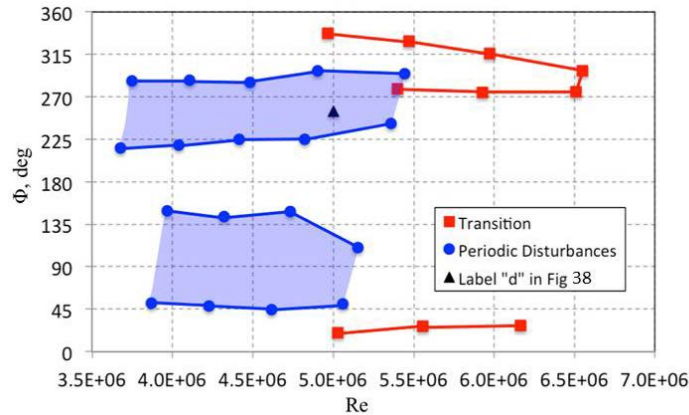


Figure 51 Periodic Disturbances and Transition Front Determined From HT3

It is instructive to compare the HIFiRE-1 flight test results to ground tests, both to examine data quality and to compare ground test to flight test trends. In particular, the HIFiRE flight vehicle showed two peculiar transition features at AoA during reentry. First, the windward transition Reynolds number during reentry at $M=7$ was less than the 0 degree AoA transition Reynolds number observed during ascent. Second, the transition pattern at angle of attack showed an indented front, with the lowest transition Reynolds number occurring on the leeward side of the vehicle, and the highest transition Reynolds number occurring between the leeward and windward meridians. Both of these transition features have been observed in ground test.

Past ground tests have indicated complex trends in transition movement on cones at angle of attack. Several investigators (as compiled by Stetson,⁴³ for example) have noted that for sharp cones, as AoA increased, windward transition moved downstream, and leeward transition moved upstream. Reda⁴⁴ observed similar trends in range tests at $M=4.5$. For blunt cones, the transition trends are less straightforward. Stetson⁴³ tested a $\theta=8$ degree cone with a variety of spherical bluntness at $M=5.9$. In these tests the wall-temperature ratio was $0.52 < T_w/T_0 < 0.58$. In these experiments, leeward transition moved upstream as AoA increased. Windward transition at first moved downstream as AoA increased, like a sharp cone. The maximum rearward movement occurred at 0.5 to 2 degree, depending on cone bluntness. As AoA increased beyond this level, transition trended upstream as AoA increased. In some cases, windward transition at AoA occurred upstream of the $\alpha=0$ transition location. In all cases however, windward transition occurred downstream of leeward transition.

Shock tunnel experiments by Stetson and Rushton⁴⁵ showed a slightly different windward transition trend with AoA. These tests were carried out on an 8 degree cone at $M=5.5$ at $T_w/T_0 = 0.32$. These experiments showed that, for two bluntnesses, both windward and leeward transition moved upstream as AoA increased. It should be noted that the lowest nonzero AoA for these cases was 2 degrees, so trends for $0 < \alpha < 2$ degrees were not captured. As in the Stetson $M=5.9$ experiments,⁴³ leeward transition movement was more pronounced than windward movement, so that the windward transition always occurred downstream of the leeward transition.

Several researchers have experimentally observed indented transition fronts. Holden⁴⁶ and Holden *et al.*⁴⁷ measured transition on sharp and blunt cones at $M=11$ and 13. In these tests the wall-temperature ratio was $T_w/T_{ad} \sim 0.14$. For the sharp cone and a 6% blunt cone, these tests showed windward transition moving downstream and leeward transition moving upstream as AoA increased. A notable feature of these tests was that at AoA, the rear-most transition location for the sharp and 6% blunt configurations did not occur on the windward or leeward meridians, but occurred near the shoulder of the model, about 90 degrees off of the pitch-plane. Experiments by Dicristina⁴⁸ on cones at AoA presented a similar indented transition front. These tests were carried out in VKF Tunnel C at freestream Mach 10. Wall temperature ratio was $T_w/T_0 = 0.28$. This model was an 8 degree sharp cone.

Since numerous investigators in different experiments examined AoA effects episodically, specific trends with freestream and model parameters are difficult to quantify. In general, for sharp cones, and blunt cones with either small bluntness and/or at low angle of attack, it can be concluded that windward transition moves downstream and leeward transition moves upstream, as AoA increases. For moderate bluntness, at larger AoA, both windward and leeward transition move upstream. With the exception of very large bluntness,^{46,47,49} leeward transition moves upstream faster than windward, so the windward transition still occurs downstream of the leeward transition. Indented transition fronts have also been observed. Anecdotal evidence suggests that this indented front may be associated with high wall-cooling. In summary, the transition behavior observed on HIFiRE-1 at AoA is consistent with past observations of cone transition in general.

Two preflight and one postflight test of HIFiRE-1 showed mixed trends regarding windward transition. Preflight tests were conducted at CUBRC^{4,6,11,12} and NASA LaRC.¹³ Since the high AoA reentry was not anticipated, the maximum AoA in these tests was limited to 5°. Postflight tests at the DLR H2K wind tunnel were carried out at a variety of angles of attack, based on as-flown conditions. CUBRC tests, conducted on the full-scale model, included attitudes of 0, 1, 2, and 5 degree AoA at Mach numbers of 6.6 and 7.2. Results for the windward meridian⁴⁷ showed transition moving upstream relative to the 0 degree transition location. Wall temperature ratio for the CUBRC tests was $T_w/T_0 = 0.13$, relatively close to the flight value of 0.18. Windward transition at $\alpha=5^\circ$ occurred in CUBRC at $M=6.6$ at $2.7 \times 10^6 < Rex < 4.3 \times 10^6$. At $\alpha=0^\circ$, transition occurred at $Rex < 5.8 \times 10^6$.

In contrast to the CUBRC results, tests in the NASA LaRC 20-inch Mach 6 wind tunnel at $\alpha=0, 3, \text{ and } 5^\circ$ showed a rearward transition movement as AoA increased, although the change was modest.¹³ Leeward transition moved forward with increasing AoA for these cases. These tests had $T_w/T_0 = 0.6$. The nosetip for the LaRC model was, relative to the model length, slightly blunter than the flight vehicle nosetip. For $\alpha=0^\circ$, windward transition occurred at $4 \times 10^6 < Rex < 4.4 \times 10^6$. For the $\alpha=5^\circ$ case, windward transition occurred at $Rex=4.6 \times 10^6$.

In postflight tests at DLR H2K, the windward transition moved aft as AoA increased. Transition at $\alpha=0^\circ$ occurred at $Rex=3.6 \times 10^6$, $\alpha=6^\circ$ at $Rex=4.6 \times 10^6$ and at $\alpha=9^\circ$, transition occurred at $Rex=5.2 \times 10^6$. The ratio of wall-to-total temperature in the H2K experiment was 0.56, comparable to the NASA LaRC $M=6$ tests.

Two possible explanations exist for the relatively early windward flight transition. One possibility is the presence of a roughness-induced transition in flight, promoted by the relatively thin windward boundary layer. A second possible source for this behavior is the level of wall cooling in ground test compared to flight. During ascent, low (less than 1°) AoA transition occurred at Reynolds numbers of approximately 10×10^6 to 12×10^6 and Mach numbers of 5.22 to 5.25. Pre- and postflight tests at a variety of Mach numbers showed $\alpha=0^\circ$ transition Reynolds numbers anywhere from 40 to 60% of flight transition Reynolds numbers. During descent, windward transition occurred at a Reynolds number of 4.7×10^6 at $\alpha=9.6^\circ$ at $M=7$. Although transition in CUBRC at $\alpha=5^\circ$ occurred at a lower Reynolds number than flight, transition in the LaRC $M=6$ wind tunnel and the DLR H2K wind tunnel occurred at slightly higher Reynolds numbers than in flight. It is well known that wall cooling destabilizes Mack-mode instabilities.⁵⁰

Stability analyses by Li⁵¹ of two flight cases showed strong Mack mode instability on the windward meridian. Li noted that a flight case at $\alpha=6.14^\circ$ showed that Mack modes reached higher N -factors on the windward meridian than on the leeward meridian. It is reasonable to expect that with increased wall cooling, the LaRC and H2K transition Reynolds numbers would be less than flight, consistent with the CUBRC data and our expectations of wind tunnel noise effects. With sufficient cooling, a transition scenario with a Mack-mode induced, turbulent windward lobe merging with crossflow-induced, turbulent side-lobe to create an indented transition contour might be observed in ground test.

6. Ascent Shock-Boundary Layer Interaction Experiment

Since the high AoA encountered during reentry made analysis of the SBLI experiment difficult for this phase of flight, the SBLI results for ascent only are presented in this report. Table 3 summarizes flight conditions for $3 < t < 22$ seconds where these data are analyzed.

Table 3 Aerodynamic Values For 3 to 22 Seconds

Time (sec)	Altitude (m)	Density (kg/m ³)	Pressure (kPa)	Mach	Re (1/m)	AoA (degrees)
3	826.5	1.0987	92.923	1.58	32.75	NA
4	1465.1	1.0362	86.288	2.27	44.51	0.12
5	2325.3	0.9524	77.961	2.95	53.53	0.1
6	3389.5	0.8618	68.545	3.45	57.06	0.2
7	4476.9	0.7634	59.928	3.28	48.29	0.14
8	5498.3	0.6893	52.683	3.14	42.04	0.06
9	6464.8	0.6162	46.528	3	36.07	0.16
10	7384.2	0.5594	41.251	2.9	31.85	0.23
11	8263.5	0.5121	36.645	2.83	28.68	0.17
12	9106.2	0.466	32.629	2.74	25.53	0.21
13	9917.7	0.4276	29.09	2.69	23.21	0.28
14	10700.4	0.3917	25.958	2.64	21.01	0.33
15	11455.7	0.3573	23.194	2.58	18.85	0.21
16	12239.1	0.3266	20.568	2.95	19.88	0.3
17	13135.5	0.2892	17.861	3.44	20.7	0.22
18	14164.8	0.2511	15.138	3.99	21.01	0.14
19	15330	0.2113	12.503	4.53	20.22	0.2
20	16625.4	0.1738	10.068	4.98	18.4	0.4
21	18016.7	0.1392	7.931	5.26	15.66	0.42
22	19431.1	0.1071	6.258	5.22	11.85	0.64

Several factors affected the quality of the data acquired in the shock boundary layer interaction. All telemetry channels experienced significant noise at the beginning of the second-stage burn, from about 15 to 17 seconds, either due to signal absorption in the rocket plume, or pointing errors due to transient vehicle motions. Lower-range pressure transducers on the cone experienced some transient sensitivity to axial acceleration during first-stage burn, but this did not appear to be a significant problem for the higher-range transducers in the SBLI. Although all low-bandwidth SBLI pressure transducers except one were within 2 kPa of each other at the beginning of flight, offsets as high as 25 kPa were observed by the time the vehicle went exoatmospheric. These zero offsets are the most significant source of

error in the mean pressure measurements. The offsets are presented as error bars on the mean pressure distributions.

Generally, the offsets were stable during exoatmospheric flight. When these offsets were accounted for in the data, a comparison of smooth and rough-side transducers indicated good agreement for $t > 16$ seconds. For $t < 12$ seconds, smooth and rough side unshifted data showed good agreement. Therefore, the offsets are presumed to have occurred between about $t=12$ and 16 seconds. Mean pressure distribution data in this report therefore presents as a best estimate the unshifted data prior to $t=12$ seconds, and shifted data for $t>16$ seconds, with the offsets included as error bars.

All high-bandwidth pressure transducers showed some degree of saturation at times during the ascent. Saturation occurred for a period of time near maximum dynamic pressure ($t=6$ seconds). Although saturation did not appear to have a significant impact on RMS fluctuation levels, it did impact signal power spectra. Power spectra were computed using the methods reported in Ref. 20 for time windows having less than 1% saturated data. Mean pressures at $x = 1.5213, 1.5313, 1.5413, 1.5513$ and 1.5613 meters on the cylinder for times ranging from 3 to 22 seconds are shown in Figure 52. All transducers showed a sharp drop in pressure shortly after 3 seconds, as the vehicle went supersonic and the interaction set up.

Presumably, this pressure drop occurred as a shock swept downstream over the transducers. The shock remained downstream of the transducer at $x=1.5213$ meters for the rest of the measurement period shown. The four other transducers on the cylinder downstream of this one each showed periods of elevated pressure as the separation-induced shock swept upstream over them and then downstream again. This shock motion was due to changes in Mach and Reynolds number during flight. The period of time that a transducer spent downstream of the separation-induced shock was proportional to its x -location. The transducer at $x=1.5313$ was downstream of the shock from 13 to 16 seconds, and the transducer most downstream of the group at $x=1.5612$ meters was downstream of the shock from 6 to 21 seconds. Some unsteadiness was observed during periods of shock motion. Spectral analysis of the low-bandwidth transducer at $x=1.5413$ meters showed that this unsteadiness occurred at 3.4 Hz, which was equal to the vehicle roll rate. Since the vehicle was at a small AoA, small movements of the separation-induced shock occurred as the transducer spun from wind-side to lee-side. This very low frequency unsteadiness due to the vehicle dynamics is distinguished from higher frequency unsteadiness, described below, that arose from fluid dynamic fluctuations.

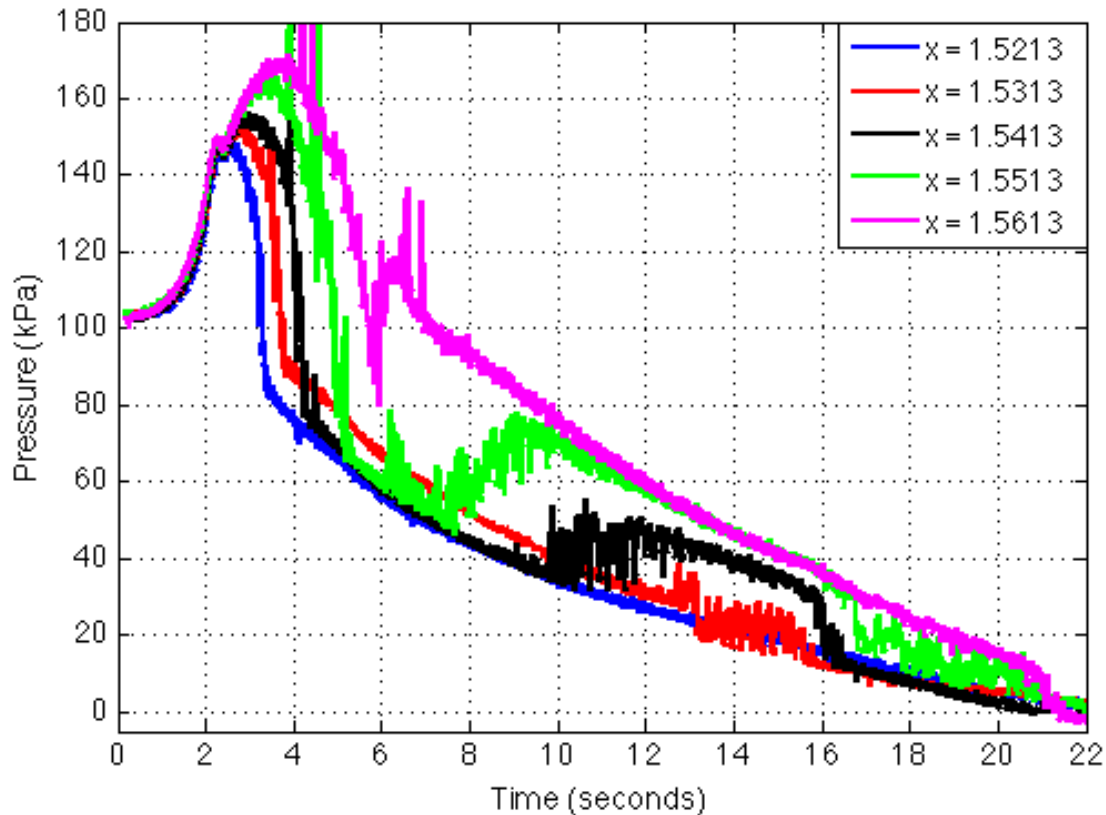


Figure 52 Mean Pressures Recorded From Low Bandwidth Pressure Transducers

Distributions of the mean surface pressure, normalized with the freestream pressure, along the length of the cylinder and flare are shown in Figure 53 for times between 3 and 22 seconds. The vertical black line in the figure represents the corner location. The error bars correspond to the zero shift of each transducer at 60 seconds. This period was chosen since it represents the period of supersonic turbulent flow over the flare during ascent. The flight vehicle went supersonic at $t=2.2$ seconds. At least a portion of the forecone possessed turbulent or transitional flow from this time up to $t=22$ seconds. At about $t=22$ seconds, the smooth-side pressures and temperatures on the flare began to deviate from the rough (tripped) side measurements. High-bandwidth fluctuating pressures also begin to drop at about this time. The pressure distributions show steady changes over time, consistent with the vehicle Mach and Reynolds numbers. Shortly after the vehicle went supersonic at approximately $t=2.2$ seconds, a definable upstream influence became observable in the pressure distribution (Figure 53, upper left). Pressure distributions upstream of the flare are inflected, typical of a separated interaction. The extent of the upstream influence decreased as the vehicle accelerated until first-stage burnout at $t=6$ seconds. During the coast phase, between 6 to 15 seconds, the upstream influence increased in extent as the vehicle decelerated and Reynolds number dropped. After the second stage firing, upstream influence again moved downstream as the vehicle accelerated and Reynolds number increased, until about $t=20$ seconds.

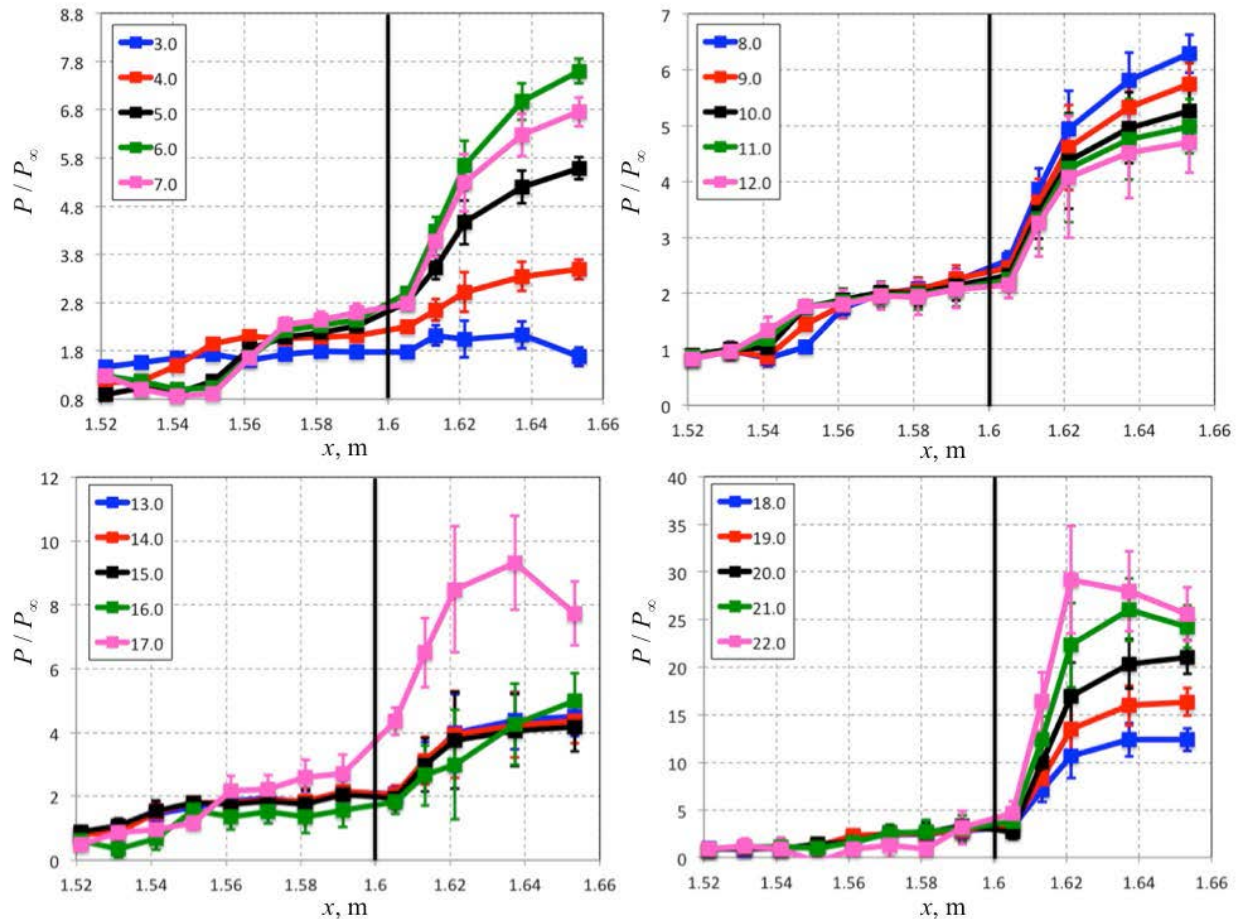


Figure 53 Normalized Mean Surface Pressure Distributions Along the Length of the Cylinder and Flare

The normalized pressure in the region upstream of the flare was relatively constant at about twice the freestream pressure after the vehicle went supersonic. Normalized pressure on the flare increased proportionally with Mach number, reaching a peak value of about 30 times the freestream pressure at the end of the analysis period at $t=22$ seconds. Until $t=21$ seconds, pressure on the flare increased with x up to the most downstream transducer. No pressure overshoot on the flare was observed until $t=21$ seconds. It should be noted that the flare was originally sized to create a separated SBLI with reattachment on the flare face at Mach 7, based on wind tunnel schlieren images. Subsequent wind tunnel heat transfer and pressure measurements indicated that the pressure and heat transfer peaks actually occurred downstream of the visualized reattachment point, near the end of the flare, and that the pressure and heat transfer on the flare did not fully relax to equilibrium values by the end of the flare.¹¹ It is not clear if reattachment occurred on the flare face in flight during ascent.

Heat transfer was computed using a 1-D conduction model as described in the Introduction. Axial conduction effects were confined mainly to the aft region of the flare where it joined the aft cylinder. A flat plate conduction model was also assumed. Data reduced with the flat plate model were compared to limited calculations carried out with a cylindrical coordinate

system, and the effect of geometry was negligible due to the relatively large radius of curvature of the vehicle. The uncertainty in the heat transfer coefficient was estimated to be at least 10%. This estimated value did not include contributions from the uncertainties of ρ_∞ , U_∞ , h_0 , and h_w . Distributions of the heat transfer coefficient along the length of the cylinder and flare for times between 3 and 22 seconds are shown in Figure 54. In Figure 54, the vertical black line at $x = 1.6$ meters represents the location of the corner between the cylinder and flare. Heat transfer measurements during the latter portion of the coast phase, and early in the second-stage boost phase, showed considerable scatter. This is because heat transfer during this portion of the flight was relatively low, resulting in poor signal-to-noise ratio. Measurements taken near first stage burnout (maximum dynamic pressure) and during the second stage burn (after $t=16$ seconds) showed better signal-to-noise ratios. Unlike the pressure distributions, many of the heat transfer distributions showed heat transfer decreasing near the back of the flare. Since the corresponding pressure measurements before $t=21$ seconds do not show a corresponding drop, this heating drop may be due to axial conduction. Nondimensional peak heat transfer rates at $t=18$ to 22 seconds ($4 < M < 5.2$, $21 \times 10^6 > Re > 12 \times 10^6$ per meter) are similar to those measured on the full-scale model at CUBRC for run 30 ($M=7.2$, $Re=9.5 \times 10^6$ per meter).⁵⁶

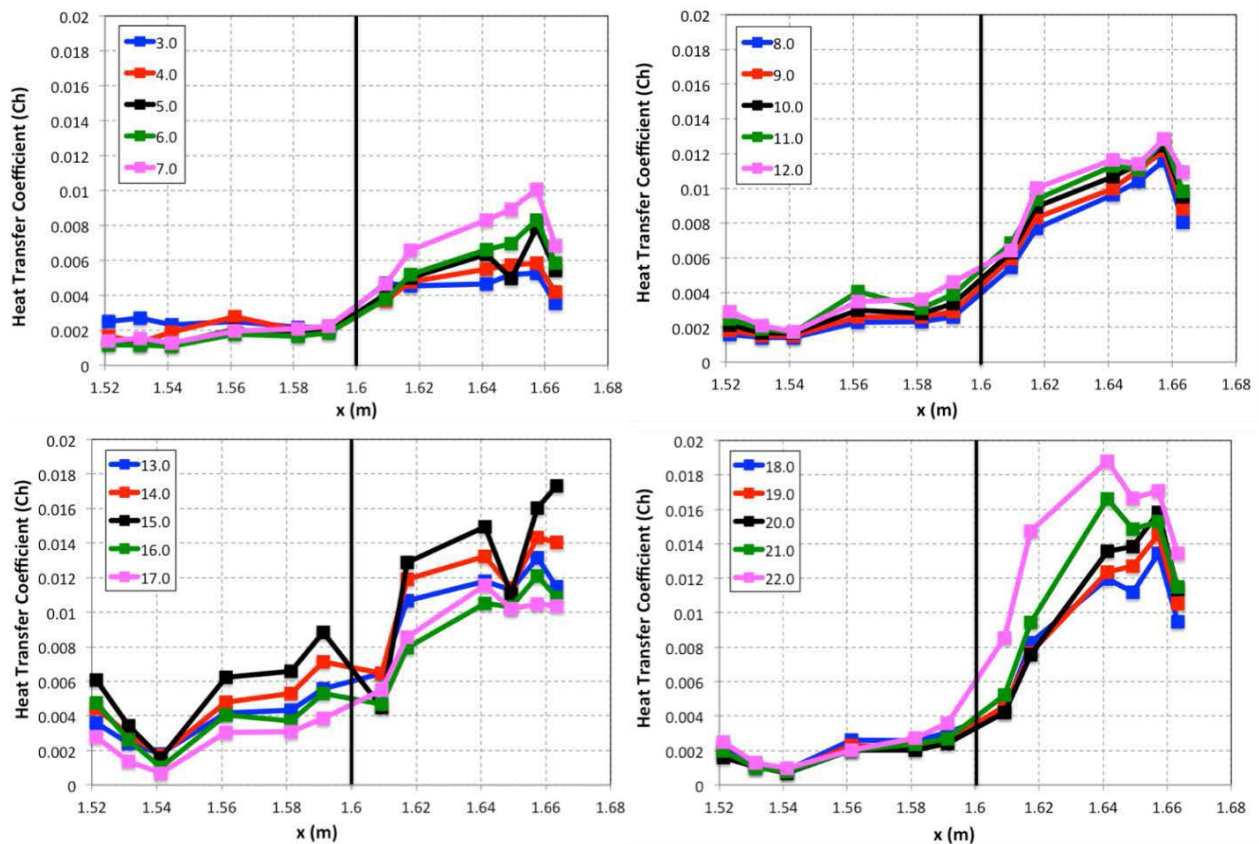


Figure 54 Heat Transfer Coefficient Distributions Along Cylinder and Flare

The RMS of the high bandwidth pressure transducers normalized by the mean pressure was computed for a 0.05 second window. The mean pressure used to normalize the RMS

corresponded to the average of the pressure trace measured with a low bandwidth pressure transducer located next to the high bandwidth pressure transducer. The pressure signal measured using the high bandwidth pressure transducers contained some saturated data points. The number of saturated data points for each 0.05 second time window for each high bandwidth pressure transducer are shown in Figure 55. In Figure 55, the total number of saturation points per time window was normalized using the total number of data points per time window. As shown, the number of saturated data points is significant for times less than 12.0 seconds. Also, saturation on the flare was significantly less than saturation on the cylinder.

Other sources of uncertainty in the normalized RMS pressures include the percent change in flight conditions for a given time window. The percent change of the Mach number for a 0.05 second window was as high as 2.7% and decreased to 1.0% during the first stage burn. During the coasting period the percent change ranged from 0.1 to 0.23%, and during the second stage burn ranged from 0.5 to 0.7%. The percentage change of the Reynolds number was very similar, only slightly lower than those for the Mach number. The percentage change in surface pressure was even smaller. The magnitude of condition changes over the measurement window was sufficiently small that it did not materially influence the results described below.

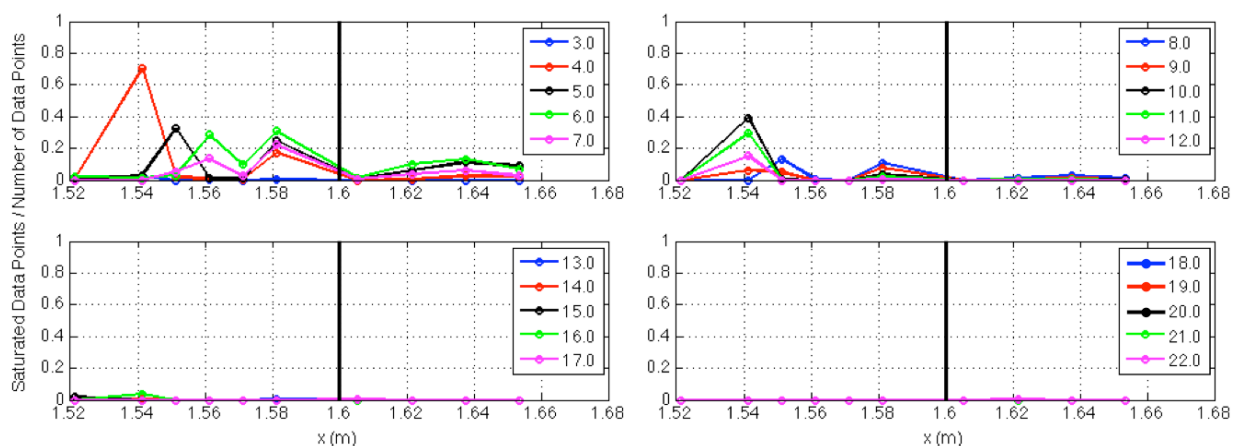


Figure 55 Normalized Saturated Data Points for the High Bandwidth Pressure Transducers

Distributions of the normalized RMS pressures along the length of the cylinder and flare are shown in Figure 56. RMS pressure distributions at $t=16$ and 17 seconds were noisy and not shown. The noise was due to the start of the second stage rocket burn. The peaks in normalized RMS pressures on the cylinder upstream of the flare are consistent with wind tunnel observations of separation-induced-shock unsteadiness in turbulent SBLI (Ref. 52, for example). The RMS pressure peaks occurred near the most upstream portion of the interaction. The RMS pressure peak generally appeared to fall between the undisturbed upstream pressure and the pressure plateau upstream of the corner, similar to SBLI measurements obtained in wind tunnels.⁵² The movement of the RMS pressure peak over the course of the trajectory is similar to the movement of the upstream influence as measured

by the mean pressure, described above. For times 4.0, 5.0 and 6.0 seconds, the Mach and Reynolds numbers increased and the location of the peak RMS on the cylinder moved downstream towards the corner. During the coasting period, the Mach and Reynolds numbers decreased and the location of the peak RMS moved upstream away from the corner. During the second stage burn, the Mach number increased while the Reynolds number initially increased and then decreased. The location of the RMS peak follows the motion of the mean upstream influence during this time period also.

Figure 57 further illustrates the motion of the upstream RMS peak. Figure 57 shows the normalized RMS as a function of time for $2.5 < t < 5.5$ seconds, for transducers on the cylinder upstream of the flare. The transducers at $x = 1.5213$, 1.5413 and 1.5513 meters measured peaks that are thought to result from the separation-induced shock motion. Transducers at $x = 1.5613$, 1.5713 , and 1.5813 meters were downstream of the separation-induced shock between 2.5 and 5.5 seconds, and therefore did not register RMS peaks. Figure 56 and Figure 57 indicate that the RMS peak varied at least 4 cm in the streamwise direction over this time period.

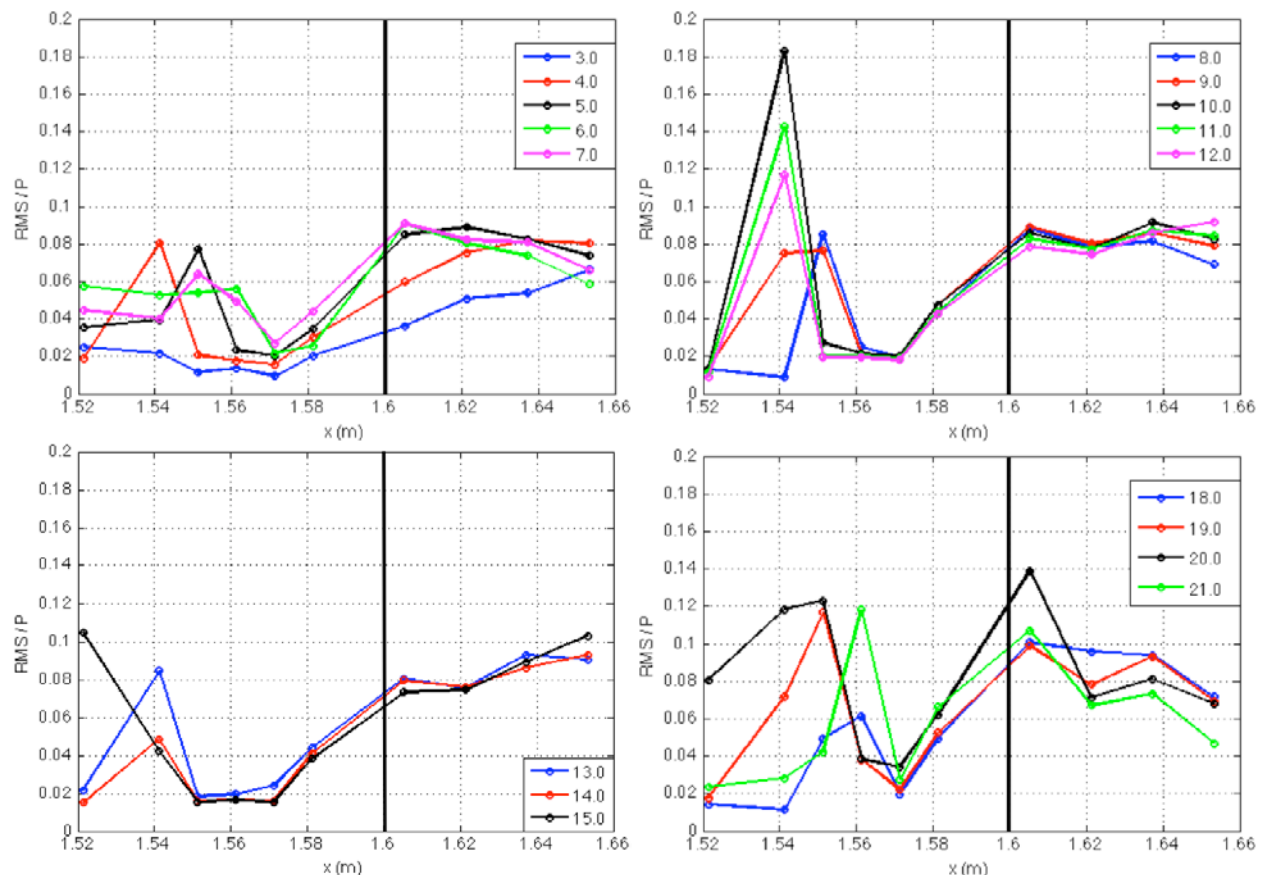


Figure 56 Normalized RMS Pressure Distributions Along Cylinder and Flare

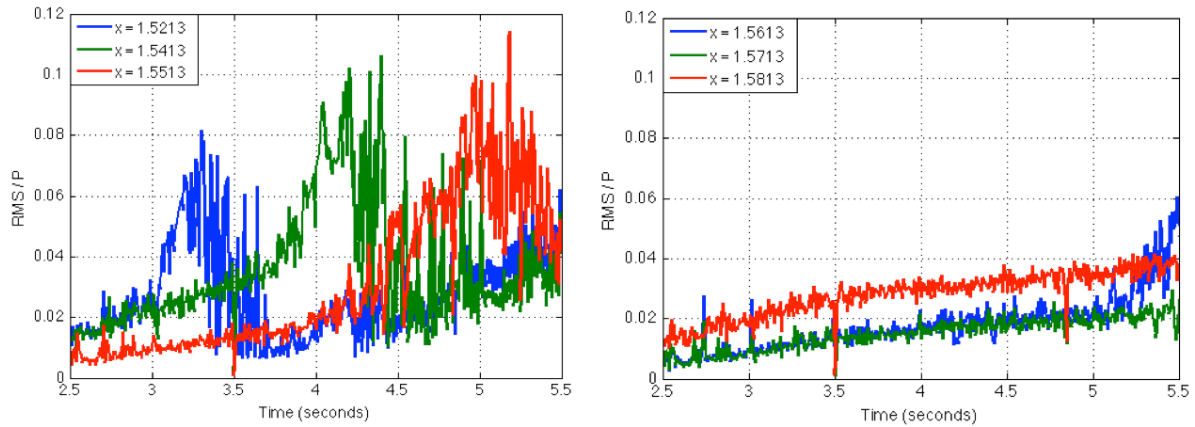


Figure 57 Normalized RMS Pressures at Versus Time

In Figure 58, the number of saturated data points normalized with the total number of data points for each high bandwidth transducer is shown. The number of saturated data points before 6 seconds, corresponding to when the initial shock wave swept across the transducers, is large. The high bandwidth pressure transducer located at $x=1.5213$ meters did not have much saturation after 3.65 seconds. Data from this transducer is sufficient for spectral analysis. In Figure 59, which shows the fluctuating pressure recorded by the high bandwidth pressure transducer at $x=1.5213$ meters, there is a bimodal distribution in an unsaturated portion of the fluctuating pressure. There are also unsaturated time windows with normal distributions. These time windows were selected for spectral analysis.

In Figure 60, power spectra for two bimodal pressure traces measured at stations located at $x=1.5213$ meters and $\phi=172$ and 352 degrees, a laminar pressure trace (measurement station located on the cone), a turbulent pressure trace (measurement station located on the cone), and the noise floor (exoatmospheric) are shown. The power levels for the bimodal pressure distribution (trace shown in Figure 59) were several orders of magnitude greater than power levels of turbulent pressure traces. Similar results were obtained for normal and bimodal pressure distributions recorded between 7.6 to 8.5 and 5.8 to 7.27 seconds, respectively with the transducer located at $x=1.5413$ meters.

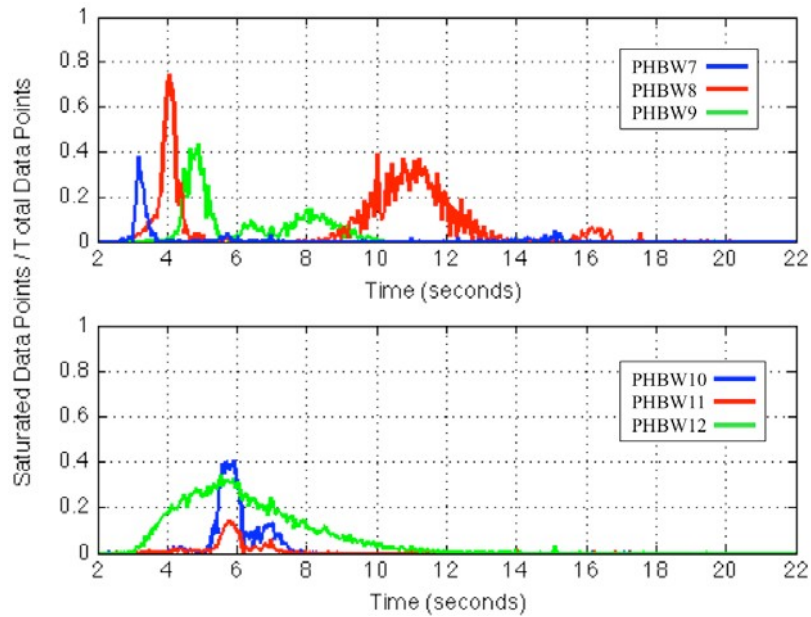


Figure 58 Saturated Data Points

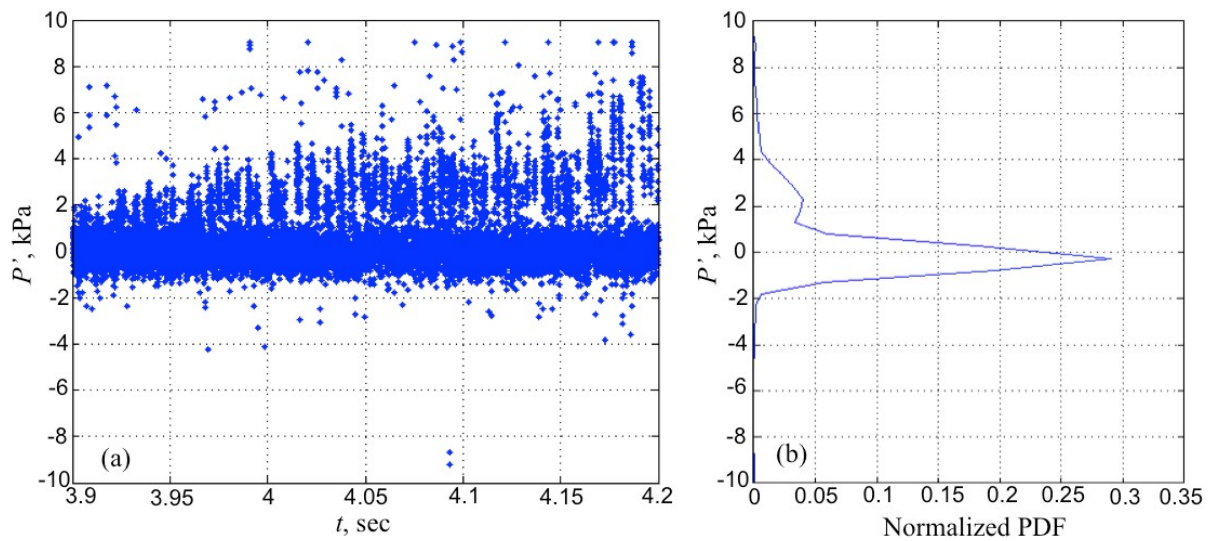


Figure 59 (a) Fluctuating Pressure Versus Time at $x=1.5213$, and (b) Normalized Histogram

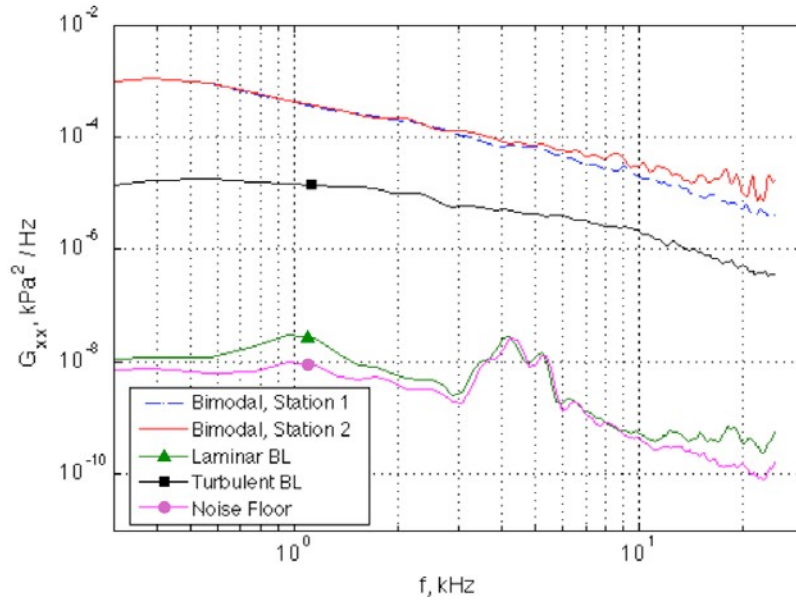


Figure 60 Pressure Transducer Power Spectra

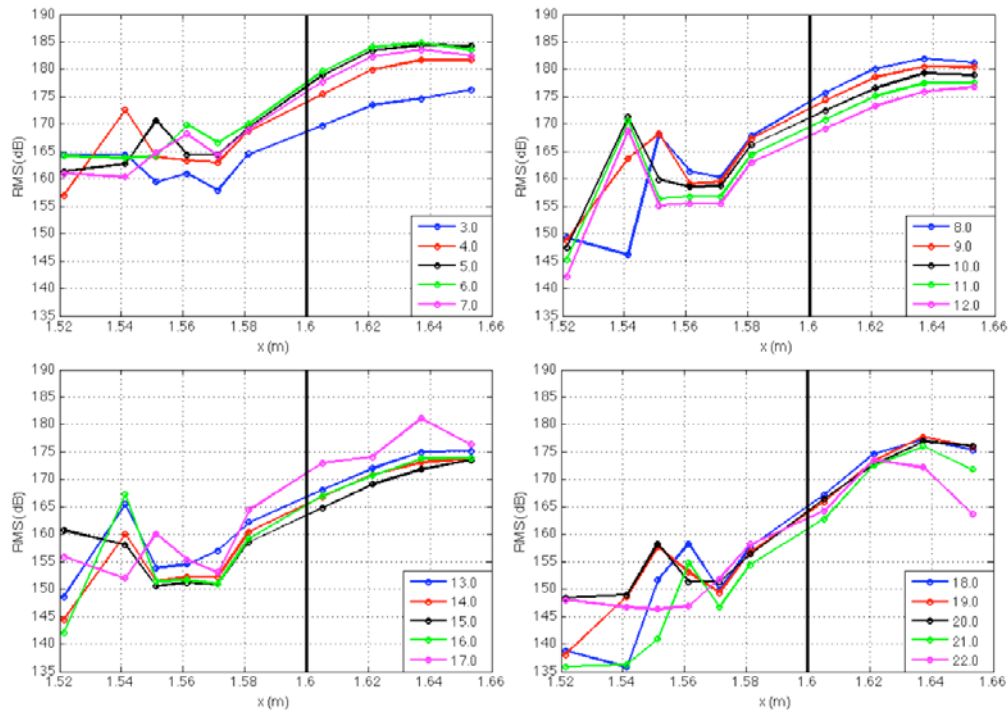


Figure 61 Sound level distributions along the length of the cylinder and flare for times 3 to 22 seconds. The black vertical line depicts the location of the corner

Distributions of fluctuating pressure levels along the length of the cylinder and flare are shown in Figure 61. In this figure, the vertical black line indicates the location of the cylinder-flare corner. The fluctuating pressure level is defined as $dB = 20 \log_{10}(p_{rms}/p_{ref})$, where $p_{ref} = 2 \times 10^{-5}$ Pa. Fluctuating pressure levels peaked at 185 dB on the flare at 6.0 seconds or the end of

the first stage burn, when the Reynolds number was at a maximum of $57 \times 10^6/\text{m}$. With the exception of the RMS pressure peak located near the beginning of the interaction, fluctuating pressure levels in the interaction were generally proportional to the mean pressure. Fluctuating pressure levels on the flare were higher than on the cylinder, due to the higher mean pressure on the flare. Upstream of the flare, the sound levels were elevated and peaked at 173 dB at 4.0 seconds. High fluctuation levels occurred even at later times in the trajectory at high altitude, especially on the flare face, where mean pressures were elevated due to the higher Mach number at these times.

7. HIFiRE-5 Flight Test Analysis

7.1. Vehicle Description

The HIFiRE-5 configuration is described in a prior paper.⁵³ The configuration consisted of a payload mounted atop an S-30 first stage⁵⁴ and Improved Orion⁵⁵ second stage motor, shown in Figure 62. The term “payload” refers to all test equipment mounted to the second stage booster, including the instrumented test article and additional control and support sections situated between the test article and the second stage motor. The test article consisted of a blunt-nosed elliptic cone of 2:1 aspect ratio, 0.86 meters in length. The vehicle was spin-stabilized. Cant-angle on the first and second-stage fins caused the vehicle to spin passively. Because of this, the payload was rolling throughout the entire trajectory.

The elliptic cone configuration was chosen as the test-article geometry based on extensive previous testing and analysis on elliptic cones.^{56,57,58,59,60,61,62,63} This prior work^{56,57,58} demonstrated that the 2:1 elliptic cone would generate significant crossflow instability at hypersonic flight conditions and potentially exhibit leading-edge transition. Figure 63 illustrates the elliptic cone geometry and coordinate system.

Figure 64 presents a dimensioned drawing of the payload, including nosetip detail. The half-angle of the elliptic cone test article in the minor axis (x - y) plane was 7 degrees, and 13.797 degrees in the major axis. The nosetip cross-section in the minor axis was a 2.5 mm radius circular arc, tangent to the cone ray describing the minor axis, and retained a 2:1 elliptical cross-section to the stagnation point. The elliptic cone major axis diameter was 431.8 mm at the base, and the cone overhung the 355.6 mm diameter second-stage booster in the yaw (x - z) plane. A section with minimal instrumentation blended the elliptical cone cross-section into the circular booster cross section. Small canards for material tests were incorporated on the transition section.⁶⁴ A cylindrical can containing GPS, antennas and other equipment resided between the transition section and the Orion booster.

The HIFiRE-5 nosetip construction was similar to that of HIFiRE-1.⁶⁶ The nosetip consisted of an iridium-coated TZM tip, followed by a carbon-steel isolator, a stainless steel joiner, and an aluminum frustum. Figure 65 illustrates the nosetip construction. Small backward facing steps were intentionally placed at the nosetip material interfaces to accommodate differential thermal expansion, with the intent that during descent these steps would have closed to present a smooth external surface. These steps were measured using a Mitutoyo SurfTest SJ-301 profilometer after the vehicle was assembled at the range. The measured step heights are presented in Figure 66. With the exception of the isolator-joiner joint, all steps were 200 microns or less. Generally, the minor axis presented lower step heights than the major axis.

The 20 mm thick aluminum frustum that served as the primary instrumented surface was constructed from two clamshell-like panels and two leading edges, described in a prior reference.⁵³ One side of the payload, the 0 to 90 and 270 to 360 degree quadrants, was reserved for transition measurement and was devoid of fasteners. The other side of the payload contained countersunk bolts that fastened the closeout panel to the leading edges. This side also contained a small closeout in the nosetip assembly that permitted final assembly of the nosetip (Figure 65). All countersinks were filled flush to the vehicle outer surface with Permatex[®] Ultra-Copper[®] RTV gasket compound prior to flight.

Figure 67, which shows the payload mounted in a handling fixture, illustrates the row of bolt holes on the closeout side. Prior tests in the NASA Langley 20-inch Mach 6 wind tunnel demonstrated that roughness-induced transition from these fasteners would not propagate to the instrumented side of the payload.⁶⁵

The primary aerothermal instrumentation for HIFiRE-5 consisted of Medtherm Corporation coaxial thermocouples. Type T (copper-constantan) thermocouples were installed in aluminum portions of the aeroshell and Type E (chromel-constantan) were installed in the steel portions. The Medtherm coaxial thermocouples were finished flush with the vehicle surface. These thermocouples were dual-junction thermocouples with one junction at the cone external surface, and the other on the back face. Kulite[®] pressure transducers measured local static pressures. Several pressure transducers were operated in differential mode to measure differential pressures 180 degrees apart on the vehicle to aid in attitude determination. Other Kulite[®] transducers were sampled at up to 60 kHz to measure high-frequency pressure fluctuations. Several Medtherm 20850-07 Schmidt-Boelter gauges provided direct heat transfer measurements.

The 0 to 90 degree quadrant of the test article was the primary instrumented surface. It contained thermocouple rays at $\phi=0$, 45 and 90 degrees. In addition, three x-stations in this quadrant, $x=400$, 600 and 800 mm, were instrumented with thermocouples at closely spaced angular locations. The other quadrant on the smooth side of the test article, 270 to 360 degrees, served as a secondary instrumented surface. It contained the Kulite pressure transducers and a limited amount of thermocouples to provide a symmetry check of the primary instrumentation quadrant.

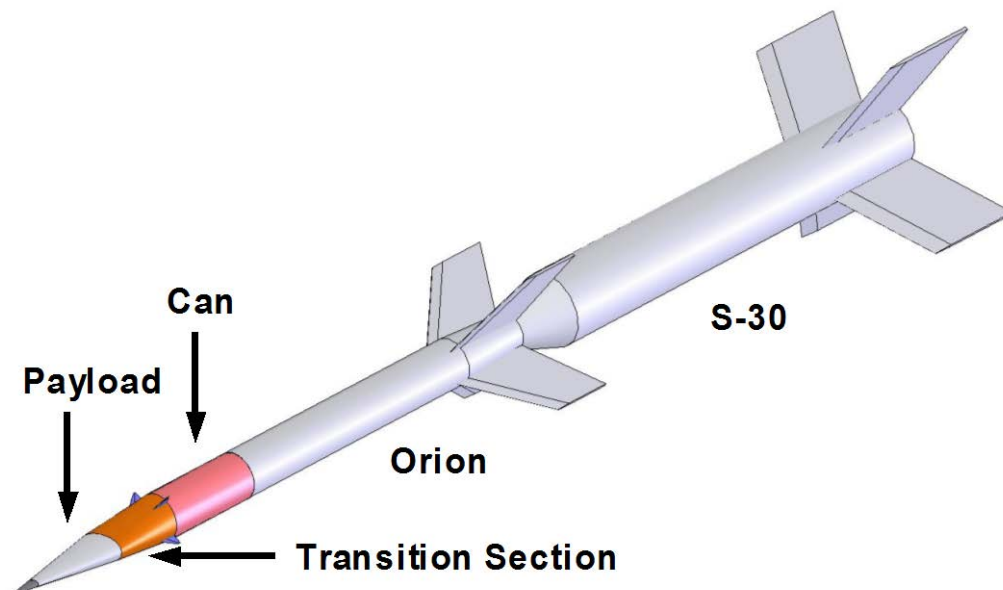


Figure 62 HIFiRE-5 Stack

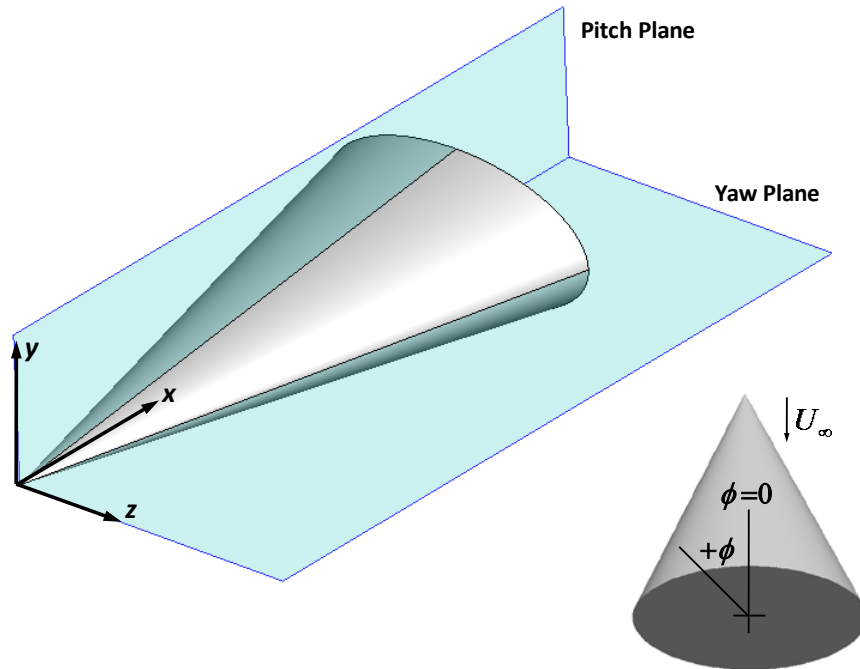


Figure 63 Elliptic Cone Geometry and Coordinate System

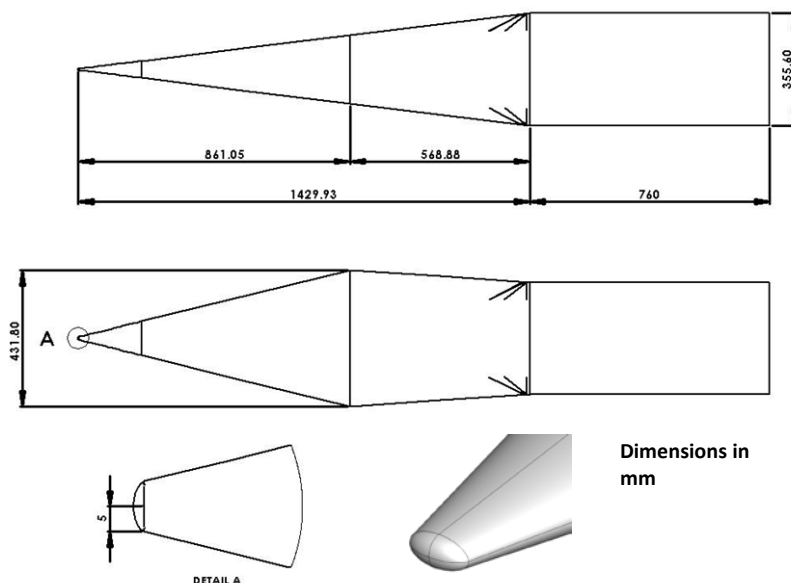


Figure 64 HIFiRE-5 Payload, Including Nosetip Detail

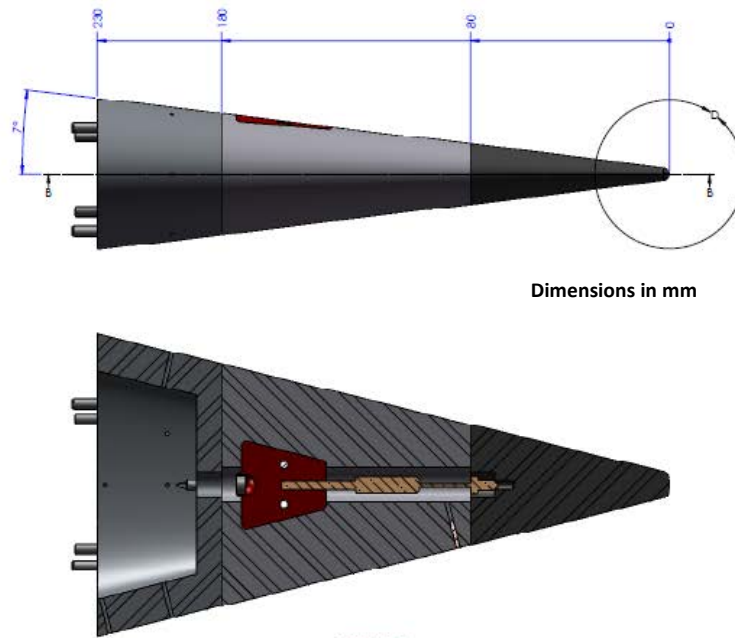


Figure 65 HIFiRE-5 Nosetip Detail

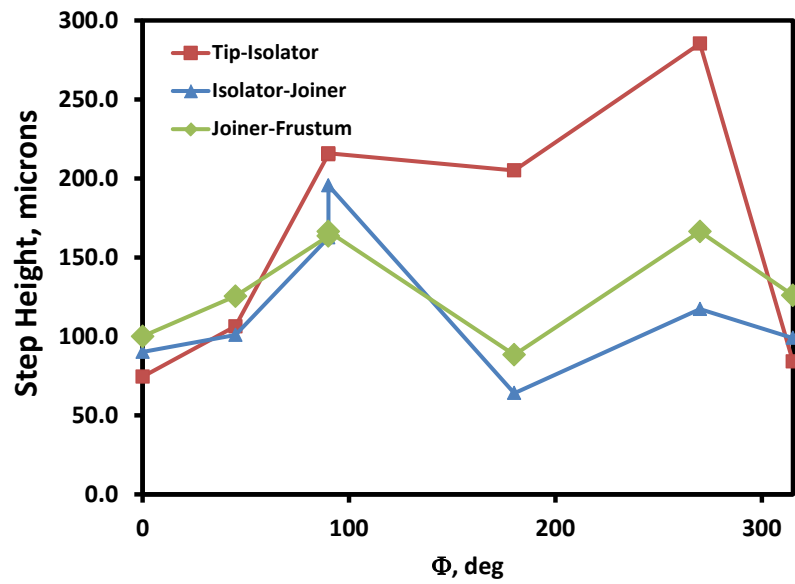


Figure 66 Nosetip Assembly Cold Step Height



Figure 67 Closeout Side of Payload Showing Fasteners (Red Circles)

7.2. Trajectory and Vehicle Attitude

HIFiRE-5 was the first HIFiRE flight to use both the Inertial Sciences Digital Miniature Attitude Reference System (DMARS-R) IMU and Ashtech DG14 Global Positioning System receiver. This permitted a cross-check of measured flight parameters between both instruments. In addition, with the flight path angle and azimuth known from either instrument, the IMU could provide vehicle AoA and yaw.

Figure 68 illustrates the vehicle altitude and velocity as measured by the onboard DMARS inertial measurement unit and GPS. Both instruments showed good agreement. A short dropout in the GPS signal occurred immediately after launch. Since the second stage failed to light, the maximum altitude achieved was only about 50 km, compared to a planned 300 km apogee. A peak velocity of just over 900 m/s was attained during ascent. Telemetry was received during descent down to 150 meters altitude.

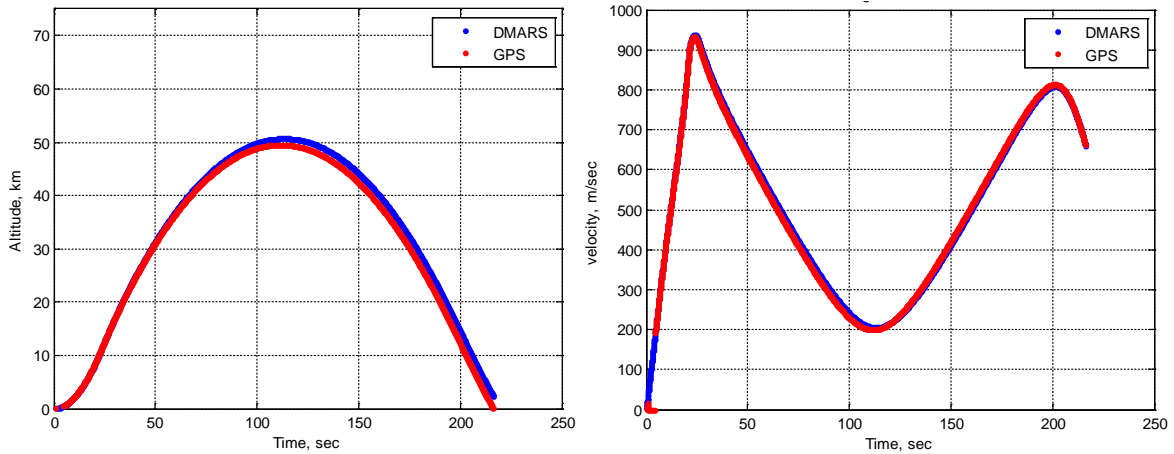


Figure 68 Vehicle Altitude (Left) and Velocity (Right)

Figure 69 illustrates the vehicle pitch and azimuth during flight. The red and green points indicate the vehicle flight path angles relative to earth, as derived from the DMARS IMU and the GPS. The blue lines represent the instantaneous vehicle pitch (θ) and azimuth (ψ) orientation as derived from the DMARS IMU. These angles were measured in vertical and horizontal planes, respectively, relative to the local horizontal and north. Both instruments were in good agreement. Some oscillations in both pitch and azimuth occurred as the vehicle exited the atmosphere (50 to 100) seconds, and during the vehicle descent (125 to 175 seconds).

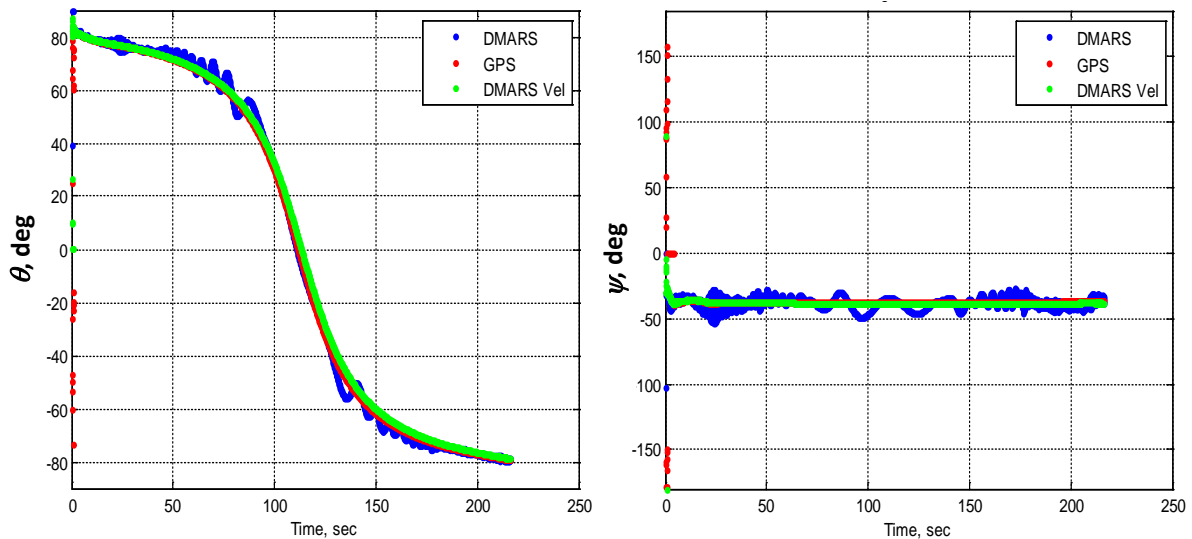


Figure 69 Vehicle Pitch Angle (Left) and Azimuth (Right)

The vehicle AoA and yaw, relative to wind, may be obtained by differencing the vehicle's measured instantaneous pitch or azimuth orientation relative to Earth (derived by integrating angular body rates from the IMU), and the flight path pitch and azimuth relative to earth (derived from the vehicle velocity vector obtained from either the IMU or GPS). This difference produces AoA and yaw relative to the flight path. Naming and sign conventions for AoA and

yaw are indicated in Figure 70. The vehicle AoA and yaw are shown in Figure 71. The vehicle experienced angles of attack approaching 4 degrees during first-stage burnout and separation. Pitch oscillations continued for a period of time after this. During descent, pitch oscillations damped with time as the vehicle descended. By the time boundary layer transition began to occur during descent, AoA was less than two degrees.

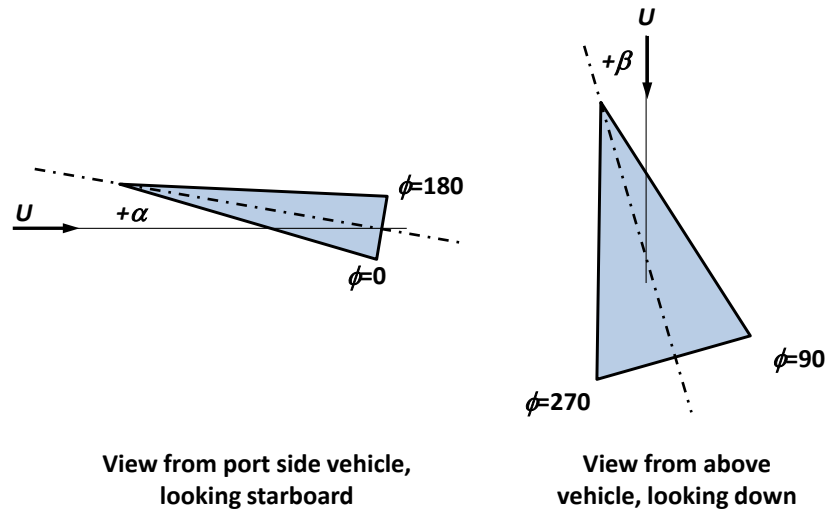


Figure 70 Vehicle Attitude Angles and Conventions

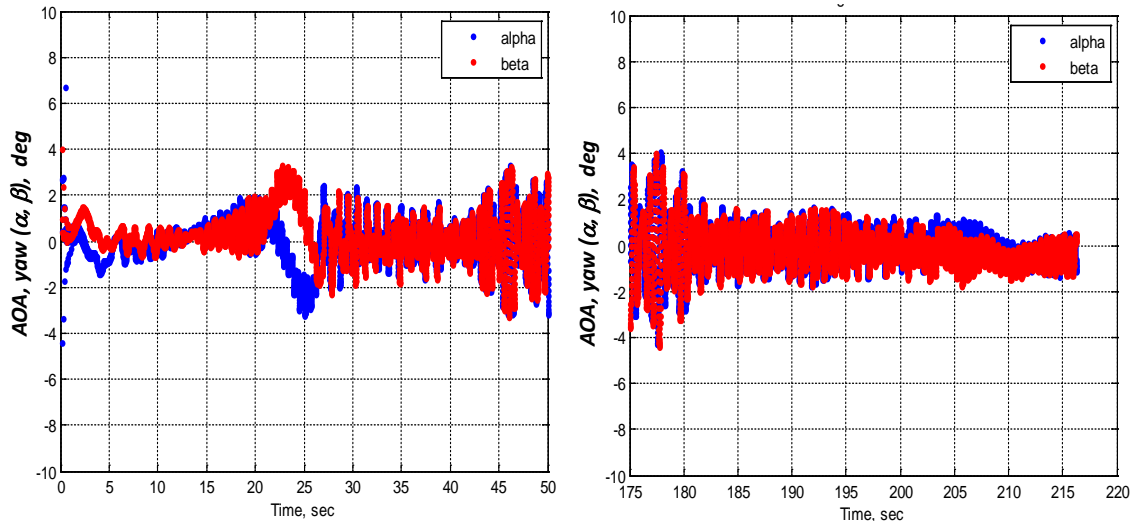


Figure 71 Vehicle AoA and Yaw During Ascent (Left) and Descent (Right)

A combination of balloon and satellite data were used to create a best-estimated-atmosphere (BEA). High-altitude weather balloons were released before and after launch from three stations to provide meteorological data. Balloons were released simultaneously from the range head at Andøya, and from down-range stations at Bjørnaya and Jan Mayen islands. Balloon data were combined with GEOS-5 satellite data to provide conditions during flight at times and locations

derived from the GPS. Freestream unit Reynolds number, per meter, is expressed Figure 72 as a function of Mach number during the flight. The peak Mach number of just over 3 occurred during ascent near first stage burnout. The maximum unit Reynolds number of $3 \times 10^7 \text{ m}^{-1}$ occurred during first stage burn. Mach number during descent was between two and three. Transition occurred during descent at Mach numbers between 2.4 and 2.7.

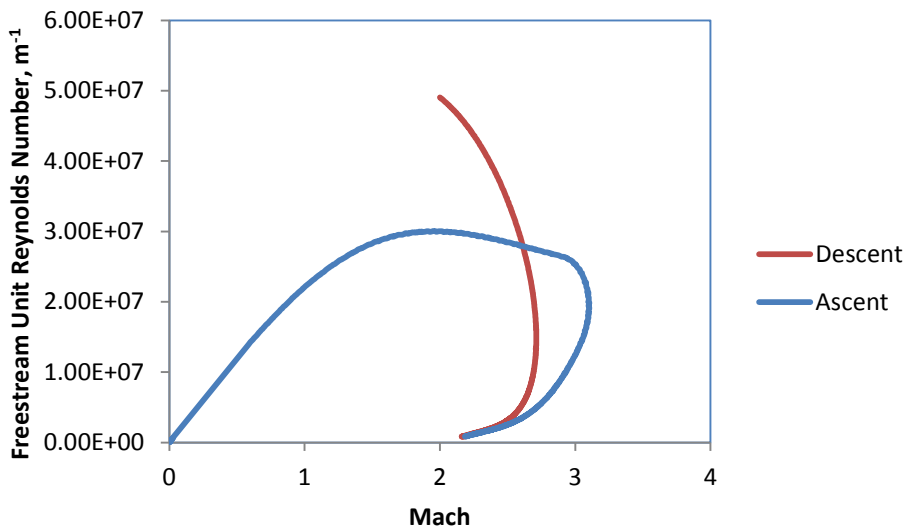


Figure 72 Reynolds Number Per Meter and Mach Number During Flight

Sample low-bandwidth absolute surface pressure measurements for transducers PLBW30 and PLBW32 are illustrated in Figure 73 and compared to AoA to assess the consistency between the two measurements. Both transducers were located on the minor axis at $x=0.82 \text{ m}$. PLBW30 was at an angular location of 0 degrees, and PLBW32 was located at 180 degrees. With the exception of some oscillations due to vehicle motion and a pressure jump during transonic flight at approximately 8 seconds after liftoff, pressure dropped monotonically during ascent. Pressure gradually increased during descent. The mean pressures on opposite sides of the vehicle showed periods of divergence from each other, for example between about 12 and 23 seconds. This indicates that even though the vehicle was spinning, one side was preferentially offered to windward or leeward, indicative of a phase-locking between the spin and its precession, or a “lunar” motion. This is supported by the AoA data. AoA during ascent showed periodic fluctuations due to the spin of the vehicle, but these were periodically biased to positive or negative. During descent, AoA fluctuations tended to oscillate about zero.

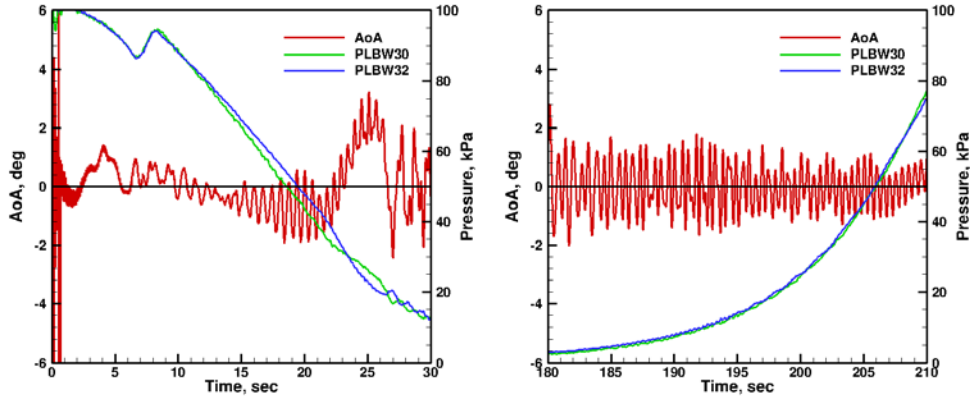


Figure 73 Sample Surface Pressure Measurements During Ascent (Left) and Descent (Right)

The AoA and yaw derived from the DMARS IMU may be further confirmed by comparing them to differential pressures. Differential pressures were measured during flight by differential pressure transducers connected to two ports located 180 degrees opposite each other on the vehicle. The differential transducer PLBW21d was located on the minor axis and primarily sensitive to AoA, and PLBW25D was located on the major axis and primarily sensitive to yaw. Both were located at $x=0.775$ m. Figure 74 compares pressures measured with these transducers to AoA and yaw. Differential pressures were normalized by freestream static pressure. The ascent AoA and yaw qualitatively resembled the respective differential pressures. This was also true during descent, although the correlation between vehicle attitude and differential pressure was less pronounced. There was generally good qualitative agreement to about 195 seconds. After this time, additional fluctuations appeared in the pressure signal, although the overall envelope of the differential pressures was similar to that of the body angles.

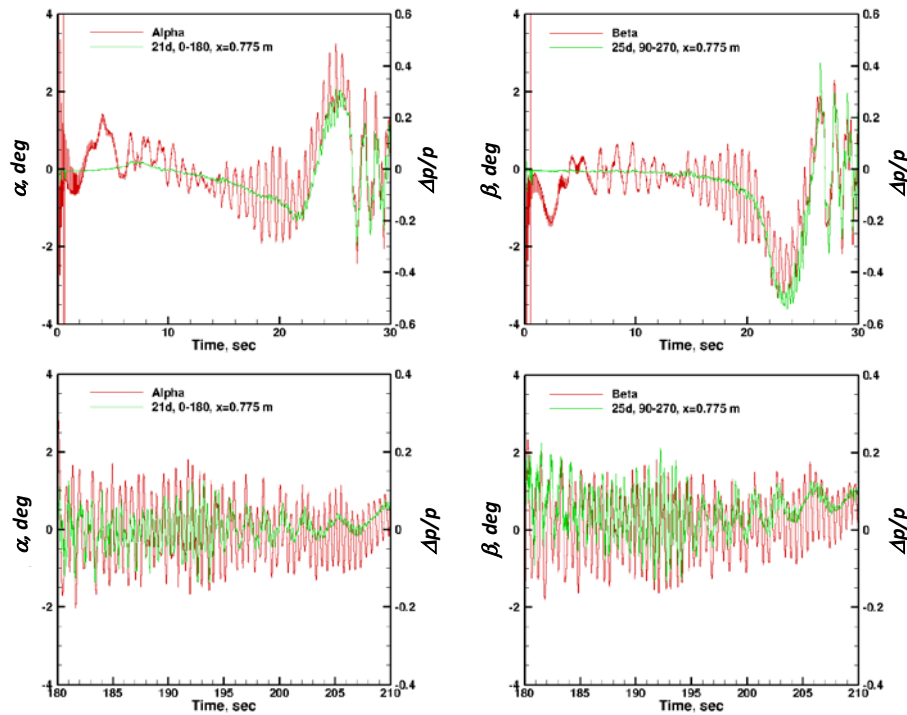


Figure 74 Ascent (Top) and Descent (Bottom) AoA (Left) and Yaw (Right), Compared to Differential Pressures

7.3. Transition Results

Sample heat transfer measurements at upstream and downstream locations on the major and minor axes illustrate major features of the transition behavior. Heat transfer results were obtained by applying an inverse heat transfer solution to thermocouple temperature measurements from the front face (wetted surface) and back face (interior surface) of the aeroshell.⁶⁶ The analysis presented in this paper is a 1D inverse heat transfer solution, including curvature terms.⁶⁶ Based on HIFiRE-1 results, axial and lateral conduction effects were expected to be minimal, and this will be assessed quantitatively at a later date. Measured front face and back face temperatures were used as boundary conditions for the inverse analysis. The resulting heat transfer rates were smoothed using a 200 point (0.25 sec) moving average. Front and back face thermocouples were zero-shifted to the same temperature prior to launch to create a zero heat flux starting condition. Ambient temperature at launch was approximately 280 K. Heat generation within the payload was neglected in the thermal analysis. Total payload electrical power consumption was approximately 240W, but most of that was confined to the payload support module, or “can” aft of the payload, and some of this power was radiated through telemetry antennas. The primary source of power dissipation in the elliptic cone test article itself was the sensor collection boards. This power generation was estimated to be less than 10W.

Measured heat transfer was compared to predicted fully laminar and fully turbulent heat transfer rates to graphically indicate when transition occurs. Laminar and turbulent heating rates were computed using a correlation developed from sharp elliptic cone wind tunnel data.⁵⁶ These

predicted levels are approximate and only intended to illustrate trends.

Figure 75 (left) presents heat transfer on the major axis during ascent and descent. Predicted turbulent heating levels were well above measured heating rates, but this quantitative disagreement was not unexpected given the approximate nature of the prediction. Both transducers were located on the vehicle leading edge (major axis) at $\phi=90$ degrees. Sensor 051 is located at $x=0.35$ m, and sensor 281 is located at $x=0.85$ m. Heat transfer peaked at about $t=21$ seconds and then decreased as first-stage thrust tailed off. The heat transfer began to drop from turbulent to laminar trends at $t=25$ to 26 seconds. Shortly after this, at about $t=27.2$ seconds, heating returned briefly to turbulent trends, then resumed its progression to laminar levels. This unsteady transition progress was coincident with AoA and yaw excursions caused by first-stage separation.

It is noteworthy that the transition events on the two transducers occurred almost simultaneously. The initial departure from turbulent heating levels occurred first on the upstream transducer, at $t=24.8$ seconds and a length Reynolds number of 3.4×10^6 . The downstream transducer registered a similar departure at $t=25.9$ seconds and a Reynolds number of 12.1×10^6 . This rapid movement of the transition front is typical of a tripped transition, and is similar to behavior observed on HIFiRE-1 during ascent.⁶⁶ The most likely source of the trip was the nosetip steps described above.

On at least one sensor, 281 ($x=0.85$ m), the heating level after ascent did not drop to fully laminar levels, but remained at an elevated level. The most likely cause for this bias was a shift in one of the thermocouples. At $t=150$ seconds, which is near the minimum temperature condition between ascent and descent, the measured front face/back face temperature differential at this location was 2.2 degrees C. All descent heat transfer results presented below were zero-shifted to zero heat transfer at $t=150$ seconds.

During descent, both leading-edge transducers showed a steady increase in heat transfer beginning near $t=170$ seconds consistent with expected laminar heating trends. A sharp increase in heating rates occurred near $t=198$ seconds. This rapid increase in heating rate occurred on the downstream transducer slightly before it occurred on the upstream transducer. This event is consistent with a transition from laminar to turbulent flow, proceeding from the aft region of the elliptic cone toward the front. The entire leading edge transitioned rapidly, as it did during ascent. The aft-most thermocouple registered transition at $t=197.62$ seconds ($Re_x=10.6 \times 10^6$), and the forward thermocouple transitioned at 198.54 seconds ($Re_x=4 \times 10^6$). This rapid transition movement again indicates a tripping event.

Previous work suggested that leading edge roughness effects might be correlated with local diameter-based Reynolds number.⁵³ During ascent, earliest (highest Reynolds number) leading edge transition occurred when Re_D reached 2.1×10^5 at the most upstream (nosedip/isolator) joint. During descent, latest (highest Reynolds number) leading edge transition occurred when the diameter Reynolds number at the most upstream joint was 1.8×10^5 . Although not conclusive, these numbers are consistent with maximum values of Re_D at which laminar flow can still be maintained in the presence of large roughness. Typical values derived hypersonic wind tunnel experiments are from Bushnell and Huffman⁶⁷ ($Re_D=2 \times 10^5$) and Murakami et al.⁶⁸ ($1.5 \times 10^5 < Re_D < 3.3 \times 10^5$).

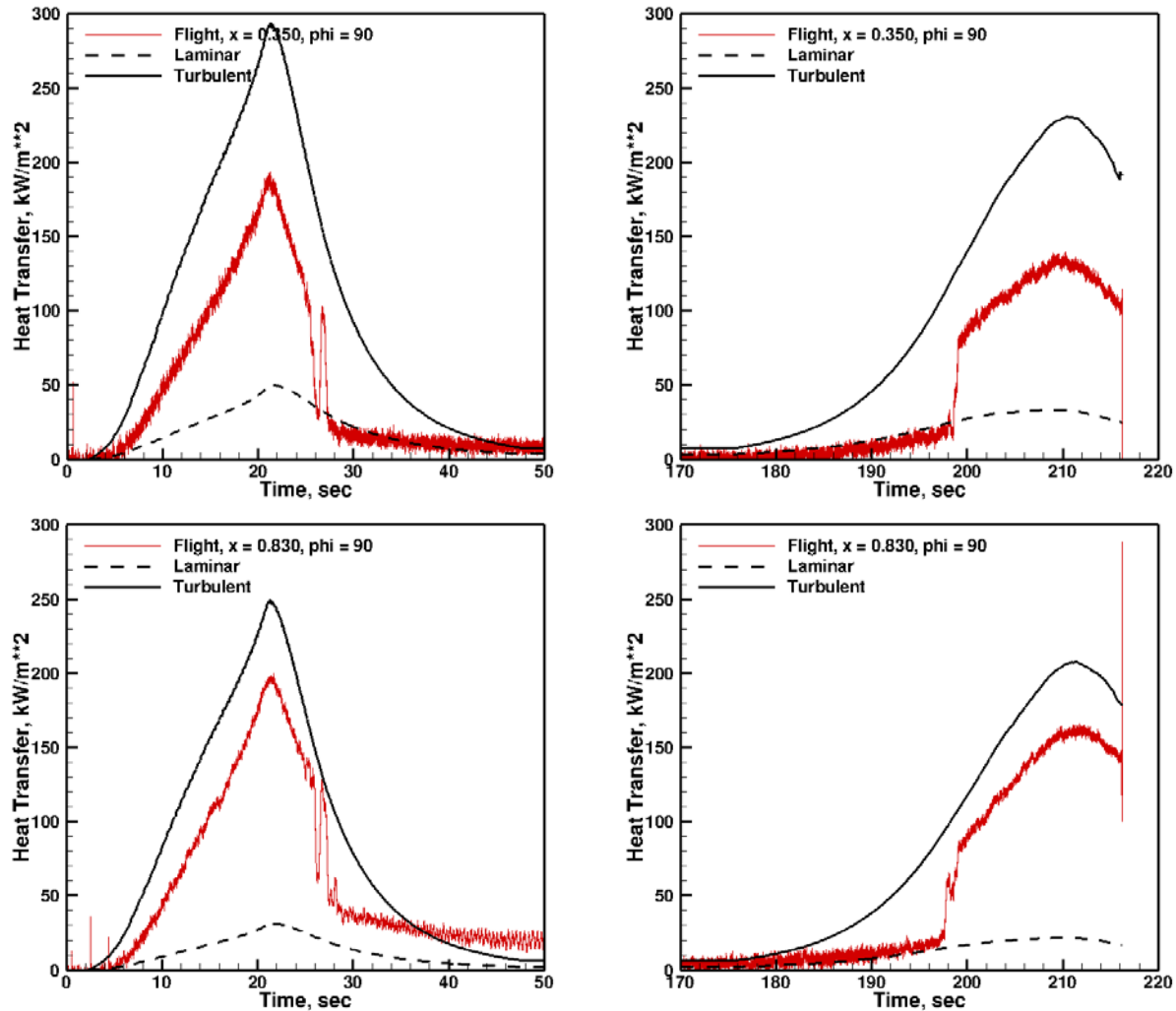


Figure 75 Heat Transfer at Upstream (Top) and Downstream (Bottom) Locations on the Leading Edge (Major Axis) During Ascent (Left) and Descent (Right)

The minor axis (centerline) transitioned at a lower Reynolds number than the leading edge, which is consistent with prior CFD^{69,70} and wind tunnel measurements^{53,65} at hypersonic conditions that indicated that the centerline is more unstable and prone to lower Reynolds number transition. Centerline transition also showed a more gradual progression over time than the leading edge transition. Heat transfer as a function of time at upstream and downstream locations on the minor axis is illustrated in Figure 76. These transducers were located at similar x -locations as the leading edge transducers, whose results are illustrated in Figure 75. Upstream transducer 047 was located at $x=0.35$ and downstream transducer 277 was located at $x=0.83$. Overall heat transfer levels for the Figure 76 transducers were lower than those shown in Figure 75, consistent with the greater radius of curvature and smaller cone angle on the minor axis. Heating rates remained at turbulent levels well through ascent. It appears that the upstream thermocouple (047, $x=0.35$) may have begun to register laminar levels shortly after $t=30$ seconds, but heating rates at this time were low, and signal-to-noise ratio is poor. During descent, heat transfer on the downstream thermocouple (277, $x=0.83$) tracked turbulent trends as

early as $t=182$ seconds. Again, since heating rates at this condition were low, and there was little difference between laminar and turbulent levels, the precise transition time is difficult to discern. Heat transfer on the upstream thermocouple during descent however, did not show a marked departure from laminar levels until approximately $t=191$ seconds. The transition process on the centerline was clearly more gradual than on the leading edge.

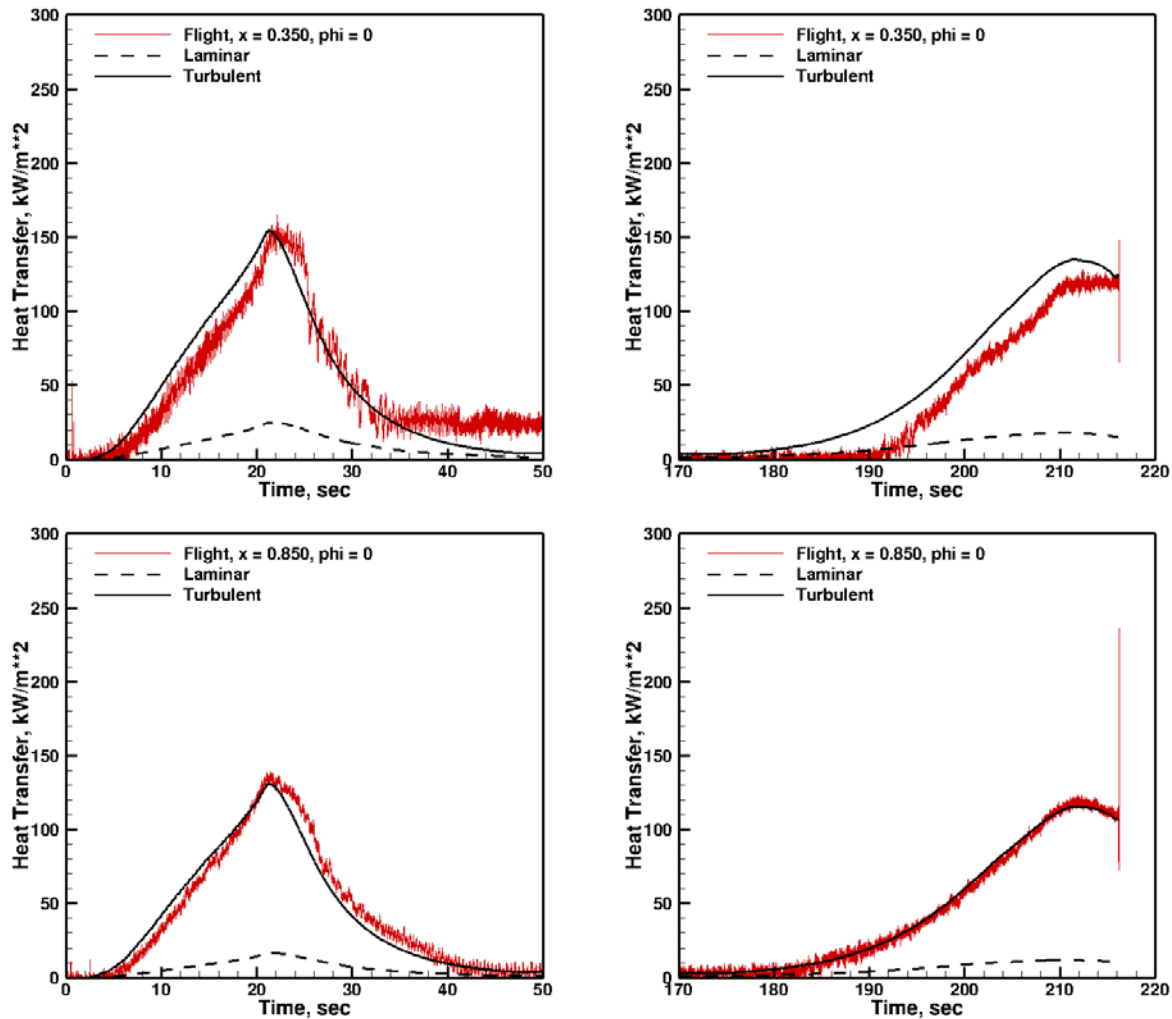


Figure 76 Heat Transfer for Upstream (Top) and Downstream (Bottom) Transducers on the Minor Axis During Ascent (Left) and Descent (Right)

Spanwise cuts of transition Reynolds numbers, obtained as a function of angular location around the test article with x -station as a parameter, provide an overall picture of the transition front. Figure 77 shows results for selected transducers at three x -locations during descent. The descent portion of the trajectory was chosen for this analysis since the angles of attack were lower, and the data are easier to interpret. The selection of transition times was somewhat subjective for two reasons. First, for early transition times near the centerline ($\phi=0$), the difference between laminar and turbulent heating is small and the first departure from laminar heating is somewhat indistinct. Also, as noted above, in some cases the transition process was intermittent, showing

one or more departures from and returns to laminar heating rates. For this reason, early and late transition times were determined, and these were used to determine an average transition time. Early transition corresponds to the first discernible departure from laminar heating rates, and late corresponds to the final discernible departure from laminar flow, after which the flow remained turbulent. The early and late bounds are indicated by dashed lines in Figure 77. For clarity, only the bounds on the most downstream station, $x=800$ mm, are indicated. Also, transition results from thermocouples on the secondary instrumentation quadrant are shown as open symbols in Figure 77 to demonstrate lateral transition symmetry. The angular location of instrumentation on the secondary quadrant has been shifted by 360 degrees in Figure 77, so that the instrument locations coincide with their mirror image location on the primary quadrant.

Given the conical shape of the test article and minor variations in Mach number during descent, smooth-body transition Reynolds number should be approximately equal at any angular location, barring nose bluntness effects or variations in the vehicle orientation. This was true for locations away from the leading edge. The variation between early and late transition at $x=800$ mm varies by about $\pm 15\%$, and the average transition location at the other x -stations generally fell within these bounds. This behavior indicates that the average transition appears to have been uninfluenced by tripped transition at the leading edge. The transition pattern agrees qualitatively with patterns observed in hypersonic wind tunnel experiments and computations^{69,70} for hypersonic flight Mach numbers, with centerline transition occurring earlier than leading edge transition, due to the more unstable centerline boundary layer.

The region near the leading edge of the test article showed a non-similar transition behavior, as expected based upon inspection of individual transducer results described above. At $x=600$ mm, transition at angular locations greater than $\phi=70$ degrees appear compromised. At $x=400$ mm, locations for $\phi>60$ degrees are non-similar. This transition pattern suggests a tripped transition near the leading edge that spilled inboard and contaminated an increasing portion of the acreage as time progressed.

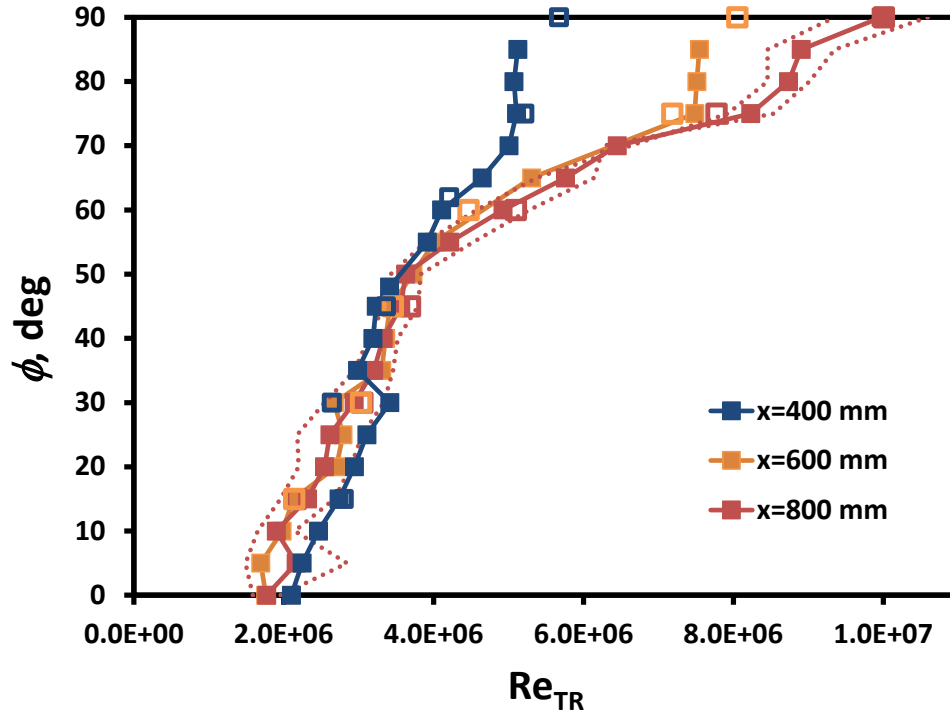


Figure 77 Transition Reynolds Numbers During Descent

Transition data obtained at varying x -locations with angular location as a parameter were used to derive transition Reynolds number in a more systematic fashion. Figure 78 shows the transition location as a function of freestream Reynolds number for several angular locations. Transition was defined in this case as the thermocouple location where the heating rate exceeded a given threshold. The threshold was selected as the local predicted laminar heating rate plus 30% of the difference between predicted laminar and turbulent rates, i.e., $\dot{q}_{TH} = 0.3(\dot{q}_T - \dot{q}_L) + \dot{q}_L$. Along these four densely instrumented rays, the thermocouples were installed in 50 mm increments from $x = 200$ to 900 mm, hence the granularity and limits of the indicated transition locations. For the $\phi=0$ and 45 degree locations, a line of constant Re_{TR} was fit to the data using the Matlab[®] function “fit” from the Curve Fitting Toolbox. The $\phi=90$ and 270 degree leading-edge rays were not curve fit, since as noted above, transition on these rays did not appear to be correlated by a constant transition Reynolds number. These curve fits indicate a transition Reynolds number of 2.2×10^6 on the $\phi=0$ degree ray and 3.1×10^6 on the $\phi=45$ degree ray. The results in Figure 78 at $x=400$, 600 and 800 mm are similar to the transition Reynolds numbers for $\phi=0$, 45 and 90 degrees plotted in Figure 77.

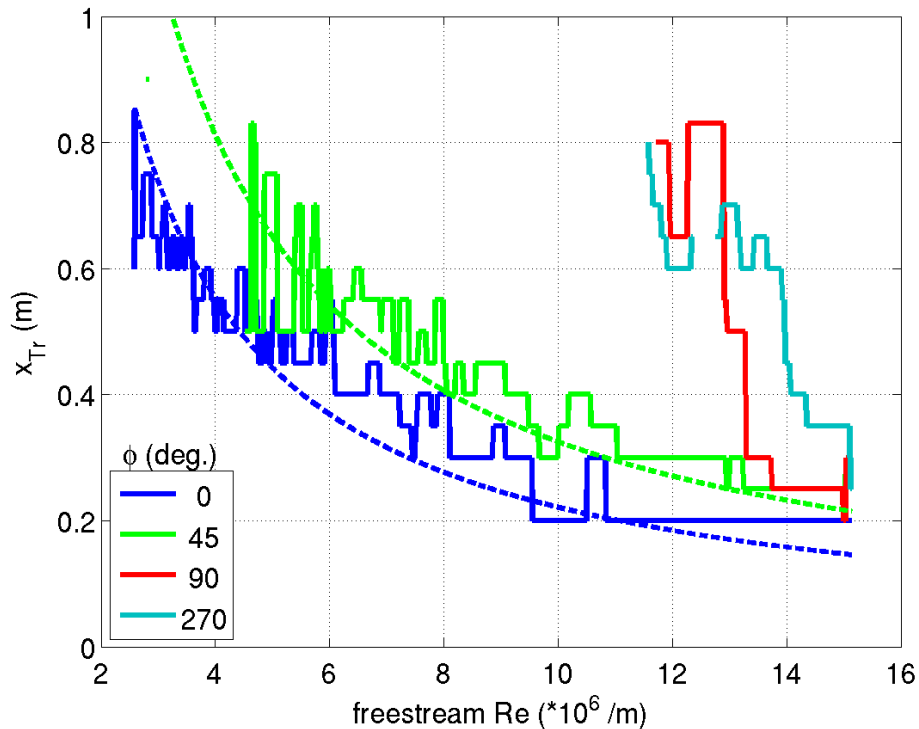


Figure 78 Transition Location as a Function of Freestream Reynolds Number at Various Angular Locations

7.4. HIFiRE-5 Conclusions and Future Work

Although HIFiRE-5 failed to reach its desired hypersonic flight conditions, the experiment acquired useful supersonic transition data. The experiment demonstrated that meaningful supersonic transition data may be obtained by using surface-mounted instrumentation on a spin-stabilized sounding rocket, even on a three-dimensional body undergoing some attitude excursions. In addition, the flight demonstrated GPS and IMU hardware new to the HIFiRE program. Although transition near the leading-edge appeared to have been affected by backward facing steps on the nosetip, the rest of the payload did not appear to demonstrate any gross effects of tripping. Since the nosetip steps were measured prior to flight, it is hoped that the leading edge data may be used to determine leading edge trip correlations for supersonic flight.

Generally, the descent portion of the trajectory provided lower angles of attack and cleaner transition behavior than did ascent. The overall transition front on the vehicle, with the exception of leading edge transition, showed a pattern similar to wind tunnel experiments and CFD, with a low-Reynolds number transition on the centerline, and higher Reynolds number transition on the leading edge. The leading edge diameter Reynolds numbers corresponding to leading edge transition were consistent with similar values measured in wind tunnel tests.

Further analysis of all the HIFiRE-5 sensors will provide a fuller picture of the test article transition behavior. Conduction analysis of the leading edge will quantify the effects of lateral conduction on heat transfer. Navier-Stokes analysis of selected trajectory points will aid in determining leading edge trip correlations and will help to validate vehicle attitude

measurements by comparing measured and computed surface pressures. These computations will include cases with non-zero yaw and AoA. Analysis of additional thermocouples and direct-read heat transfer gauges will provide more detailed maps of the transition front. These data will be combined with instantaneous attitude data to examine the effect of body attitude on transition, including the ascent phase. High bandwidth pressure data will be analyzed for spectral content and broad-band RMS.

8. HIFiRE-5 Ground Test

8.1. Background

An effort was made to document the properties of apparent traveling crossflow disturbances on the HIFiRE-5 configuration that had been noted in ground test.^{71,72} For 3D vehicle configurations with significant crossflow, the crossflow instability can become the dominant path to boundary layer transition. Both stationary and traveling modes are possible with stationary vortices nearly aligned with the inviscid streamline direction, and traveling waves inclined at a steep angle to the inviscid streamlines. The wave vector of the most unstable traveling mode has a spanwise component opposite to the direction of the crossflow.⁷³ For incompressible flows the stationary modes are typically dominant in low noise environments of flight and “quiet” wind tunnels, while the traveling modes tend to dominate in conventional tunnels.⁷⁴ The stationary mode is thought to be seeded by natural surface roughness, while the travelling mode is generated by vortical disturbances in the freestream which are entrained in the boundary layer.⁷⁵ Saric^{74,76} suggested that the same behavior should be seen for compressible flows.

Considerable effort has been given to crossflow instabilities for incompressible flow.^{75, 77, 78, 79} Saric and Reed⁷⁴ detail the pertinence of nonlinear effects when predicting crossflow instability growth and transition for incompressible flow. It has been well established that stationary modes, after a period of linear growth, saturate nonlinearly and give rise to secondary instabilities that then rapidly lead to transition (see, for instance, White⁸⁰). Most of the extant crossflow work has focused on stationary modes, since this is expected to be the dominant crossflow instability in the low-noise flight environment.

Despite much effort to understand the crossflow instability, little of it has focused on the hypersonic regime. King⁸¹ made measurements of crossflow-dominated transition at Mach 3.5 in quiet and noisy flow. Poggie and Kimmel⁸² measured traveling crossflow waves at Mach 8 on an elliptic cone with hot films, but were not able to get good agreement with computational results. They suggest that the poor agreement was due to the limitations of the computations. Malik⁸³ detailed results from a crossflow-dominated hypersonic flight test including stability computations. Choudhari⁶⁹ details stability computations for HIFiRE-5 for both flight and wind tunnel conditions. Swanson⁸⁴ measured stationary crossflow vortices at Mach 6 in a quiet wind tunnel. Borg⁷¹ describes previous experiments for the HIFiRE-5 geometry that primarily focused on stationary crossflow modes in the BAM6QT. Traveling crossflow waves were also detected, but were not the main focus of the previous studies.

Although the highly nonlinear development of the crossflow instability modes has been well-documented for incompressible flows, the contribution of nonlinear processes at hypersonic Mach numbers is not well understood. The current experiments attempt to verify the presence of the traveling crossflow instability as well as help establish the extent of nonlinear interactions for the traveling crossflow instability in the hypersonic regime. Experimental crossflow instability properties are compared to computations to verify that the measured disturbances are crossflow and not some other instability mechanism.

8.2. Test Article and Methods

The model, shown in Figure 79, is a 38.1% scale model of the flight vehicle. It includes the vehicle features from the nose to the payload/transition-section interface. The model is 328.1 mm long and has a base diameter of 164.6 mm in the major-axis direction and maintains 2:1 ellipticity from the base to the tip. The 76.2 mm long nosetip is fabricated from 15-5 stainless steel, followed by a frustum made of 7075T6 aluminum. For the present experiments, much of the model acreage was spray-painted black. The paint was left on the model after previous florescent oil flow visualization. The edges of the paint were sanded with fine-grit sand paper to more smoothly transition the model surface from the bare aluminum finish to the paint layer. A more complete description of the model can be found in Juliano.⁸⁵



Figure 79 HIFiRE-5 Wind Tunnel Model

Experiments were performed in Purdue University's Boeing AFOSR/Mach-6 Quiet Tunnel (BAM6QT). Quiet flow was realized for freestream Reynolds numbers up to $12.2 \times 10^6 / m$. The Purdue tunnel achieves quiet noise levels by maintaining a laminar boundary layer on the tunnel walls. A laminar boundary layer is achieved by removing the nozzle boundary layer just upstream of the throat via a bleed suction system. A new, laminar boundary layer then begins near the nozzle throat. The boundary layer is kept laminar by maintaining a highly-polished nozzle wall to reduce roughness effects. The divergence of the nozzle is intentionally very gradual to mitigate the centrifugal Görtler instability on the tunnel walls.⁸⁶ The experimental results presented in this paper were obtained with the model at 0 degrees AoA and yaw.

Kulite XCQ-062-15A and XCE-062-15A pressure transducers with A-screens were mounted flush with the model surface to detect traveling crossflow waves. The Kulite sensors are mechanically stopped at about 1 bar so that they can survive the full stagnation pressure in the BAM6QT and still maintain the sensitivity of a 1 bar full-scale sensor. These sensors typically have flat frequency response up to about 30 to 40% of their roughly 270 to 285 kHz resonant frequency.⁸⁷

For the current experiments, five instrumentation holes were available in the model. Table 4 shows the locations of the instrumentation holes. Figure 80 shows a sketch of the model and sensor holes. The holes were located in a region of the model that had previously shown strong stationary crossflow vortices.^{71, 85, 88} Although there were five holes, there were only four

available pressure sensors for most of the quiet experiments, so some repositioning of the sensors was necessary to gather data from all five sensor hole locations.

Table 4 Sensor Locations

Hole Number	x (mm)	y (mm)
1	310.14	41.21
2	312.56	45.09
3	312.56	39.78
4	315.48	43.04
5	318.07	39.78

Sixteen unique runs comprised a Reynolds number sweep from $Re=5.9 \times 10^6$ to 12.2×10^6 /m with a fine gradation in Reynolds number (changes of about 35 kPa in initial stagnation pressure). This allowed the development and evolution of the traveling crossflow waves to be studied in great detail. Figure 81 shows power spectral densities (PSD) for some of the Reynolds numbers tested for sensors 1, 3, and 5. A sensor was also installed in hole 4, but at some unknown point during the experiments, it came loose from the hole. Thus, data from sensor 4 are regarded as unreliable and are not shown.

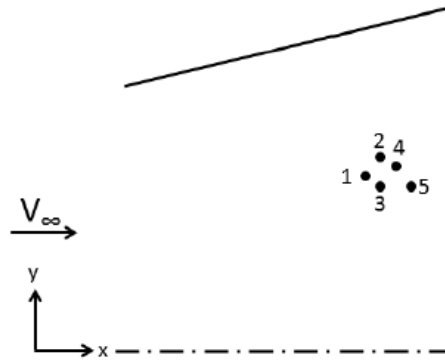


Figure 80 Schematic of Instrumentation Holes

Data were sampled at 5 MHz. The time traces at the conditions of interest were divided into 243 windowed segments of 4096 samples, meaning that each PSD is for 199 ms of data. For the BAM6QT, the time it takes for the expansion wave to traverse the length of the driver tube, reflect, and return is approximately 200 ms. Thus, each PSD is computed for quasi-steady conditions with at most one 5 to 6% reduction in Reynolds number due to the reflecting expansion wave. Freestream Reynolds numbers were estimated using a method developed previously⁸⁹. Uncertainty in the calculated freestream Reynolds number is largely due to 2 s of massively separated nozzle wall boundary layer just subsequent to tunnel startup.

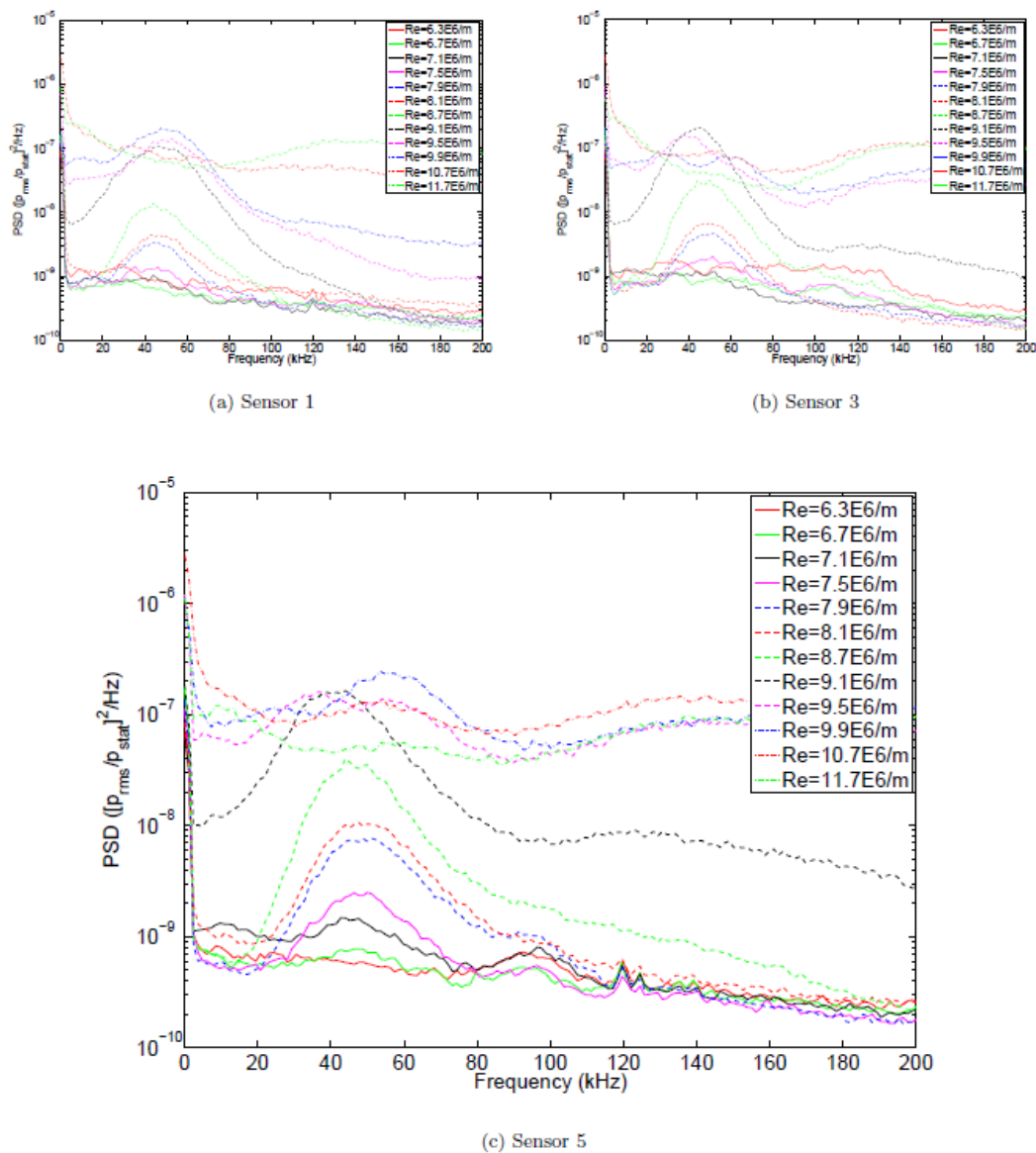


Figure 81 PSDs for Quiet Reynolds Number Sweep, Sensors 1, 3, and 5

8.3. HIFiRE-5 Ground Test Pressure Sensor Array Results

For all three sensor locations, the spectra at $Re=6.3 \times 10^6$ /m appear to be laminar without measurable disturbances. For each sensor, as Re is increased, a small peak in the spectra centered near 45 kHz begins to grow above the laminar spectra, which is essentially the noise floor. The magnitude of the peak centered at 45 kHz continues to increase with Re until apparent transition onset is evidenced by peak broadening and elevated power at all frequencies. As Re continues to increase, the main 45 kHz disturbance peak begins to be overwhelmed by power at all other frequencies as the boundary layer begins to transition. For the highest Reynolds numbers, the boundary layer is fully turbulent, and little or no evidence of the traveling crossflow waves remains.

For sensors 1 and 3, the 45 kHz traveling wave is not seen until $Re=7.2 \times 10^6$ to 7.6×10^6 /m. For sensor 5, the disturbance can barely be seen for $Re=6.8 \times 10^6$ /m. For sensor 1, the boundary layer has not completely transitioned at the highest Reynolds number. The spectra for $Re=11.1$ and 12.2×10^6 /m do not quite fall on top of each other. For sensors 3 and 5, however, the spectra for $Re=11.1$ and 12.2×10^6 /m fall nearly on top of each other, indicating that the boundary layer at sensors 3 and 5 is turbulent for $Re \geq 11.1 \times 10^6$ /m. Additionally, the unit Reynolds numbers for which spectral broadening starts to be significant decreases with increasing downstream sensor location.

Computations for $Re=8.3 \times 10^6$ /m predicted a peak N -factor of 11.5 for traveling crossflow waves near the sensor locations at 40 kHz,⁷² in good agreement with the experimental peak shown in Figure 81. For reference, an N -factor contour plot (reproduced from Ref. 69, with sensor locations and notation added), for traveling crossflow at $Re=9.8 \times 10^6$ /m is shown in Figure 82. The computations for $Re=8.1 \times 10^6$ /m also show that the pressure eigenfunction for traveling crossflow waves near the sensor locations has its peak amplitude away from the surface. However, the amplitude at the surface is still around 73% of the peak amplitude.⁷² Thus, conditions are not unfavorable for detection of traveling crossflow waves with surface-mounted pressure sensors. All of these data are consistent with traveling 45 kHz crossflow instability waves that grow in amplitude for increasing Reynolds number.

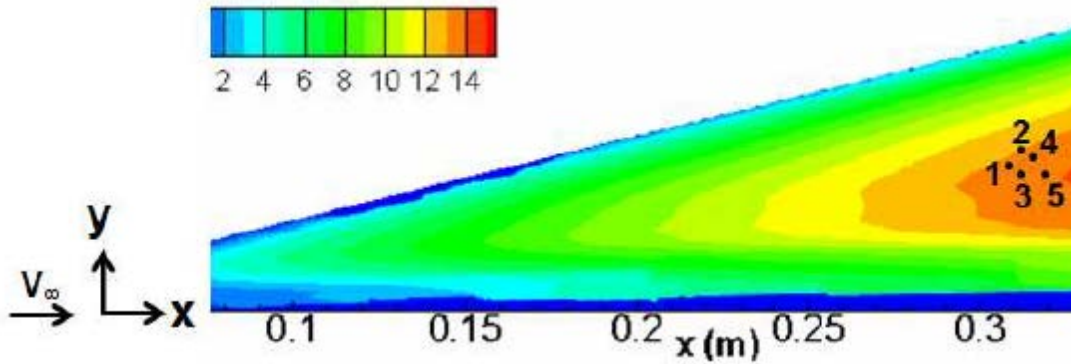


Figure 82 N-factor Contour for Traveling Crossflow for $Re= 9.8 \times 10^6$ /m

The utilization of four sensors allows the calculation of disturbance phase speed and wave angle as a function of frequency using the cross spectrum. Although the more general case allows four sensors, the minimum number of sensors needed to calculate the quantities of interest is three, since two unique sensor pairs are needed. The method of Ref. 90 as used in Ref. 82 was followed to calculate the wave angle and phase speed. The autospectrum of a sensor's signal is given by

$$G(f) = 2 \lim_{\tau \rightarrow \infty} (1/\tau) (E[|\hat{s}(f, \tau)|^2]) \quad (4)$$

Here, the Fourier transform of a measured signal $s(t)$ is $\hat{s}(f)$, and the expected value operator is $E[\cdot]$.

The cross spectrum of two signals is similarly

$$G(f) = 2 \lim_{\tau \rightarrow \infty} (1/\tau) (E[\hat{s}_1^*(f, \tau) \hat{s}_2(f, \tau)]) \quad (5)$$

where $*$ denotes a complex conjugate. A convenient, real-valued method of measuring the amplitude of the cross spectrum is the coherence, given by

$$\gamma^2(f) = \frac{|S_{12}(f)|^2}{S_{11}(f)S_{22}(f)} \quad (6)$$

The coherence is essentially a frequency-dependent cross correlation of the signals. The normalization factor is the maximum value that the cross spectrum can achieve. Thus, normalizing by this value yields coherence values from 0 to 1, with 0 meaning no correlation between the signals and 1 signifying perfect correlation.

The phase spectrum can then be found by

$$\theta(f) = \tan^{-1} \left(\frac{I[S_{12}]}{R[S_{12}]} \right) \quad (7)$$

where $I[]$ and $R[]$ represent the real and imaginary components, respectively. The time delay associated with the phase spectrum is given by

$$\tau(f) = \Theta(f)/2\pi f \quad (8)$$

An arbitrary configuration of four probes and incident planar waves is sketched in Figure 83a. Rotating the coordinate system by Ψ , the angle between the wave propagation direction and the E axis, transforms the arrangement to that shown in Figure 83. Here, E and η are the axial and circumferential surface coordinates projected onto the $x - y$ plane. This method is valid for regions of small local surface curvature.

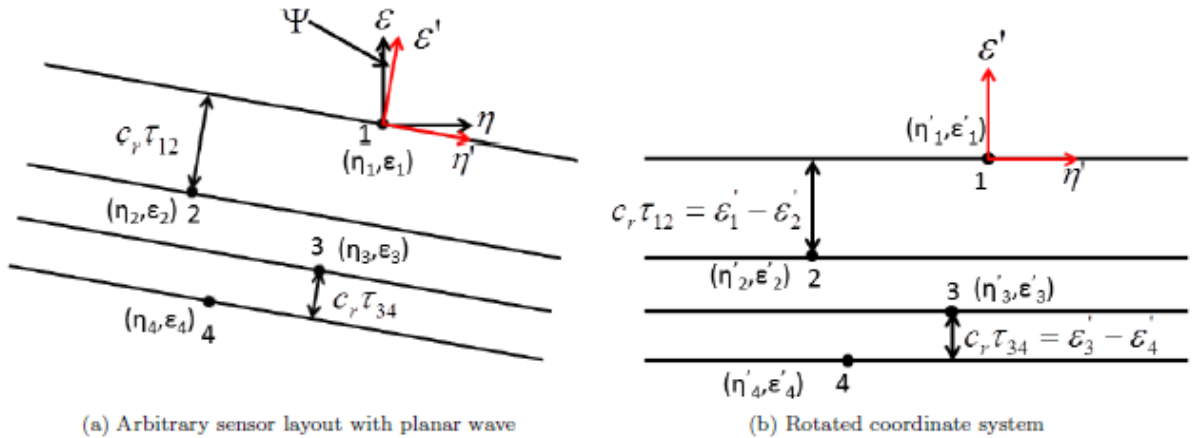


Figure 83 Notional Sensor Layout for Cross-Spectral Analysis

The relation between points in the original coordinate system (E, η) and the rotated system (E', η') is given by

$$\eta' = \eta \cos \Psi - \epsilon \sin \Psi \quad (9)$$

$$\epsilon' = \eta \sin \Psi + \epsilon \cos \Psi \quad (10)$$

The time delay between the arrival of a particular phase surface at sensors a and b is given by

$$c_r \tau_{12} = \varepsilon'_1 - \varepsilon'_2 \quad (11)$$

where c_r is the phase speed and τ_{12} is the time delay between a particular phase surface arriving at sensors 1 and 2. Two unique sensor pair sets ab and cd are chosen. Here, a , b , c , and d can be any of the four sensors, subject to the constraints that $a \neq b$ and $c \neq d$. Using Equations 10 and 11 for both sensor pairs and solving the resultant system of equations, the propagation angle, Ψ and phase speed, c_r can be found from

$$\Psi = \tan^{-1} \left[\frac{\tau_{ab}(\epsilon_d - \epsilon_c) - \tau_{cd}(\epsilon_b - \epsilon_a)}{-\tau_{ab}(\eta_d - \eta_c) + \tau_{cd}(\eta_b - \eta_a)} \right] \quad (12)$$

and

$$c_r = \frac{\sin \Psi (\eta_a - \eta_b) + \cos \Psi (\epsilon_a - \epsilon_b)}{\tau_{ab}} \quad (13)$$

8.4. Traveling Crossflow Wave Properties

Using Equations 12 and 13 and the pressure traces from sensors 1, 3, and 5, the wave angle and phase velocity of the traveling crossflow waves were calculated for $Re=6.8 \times 10^6$ to 9.0×10^6 /m. Typical plots of PSD, coherence, phase delay, and time delay for $Re=8.5 \times 10^6$ /m are shown in Figure 84.

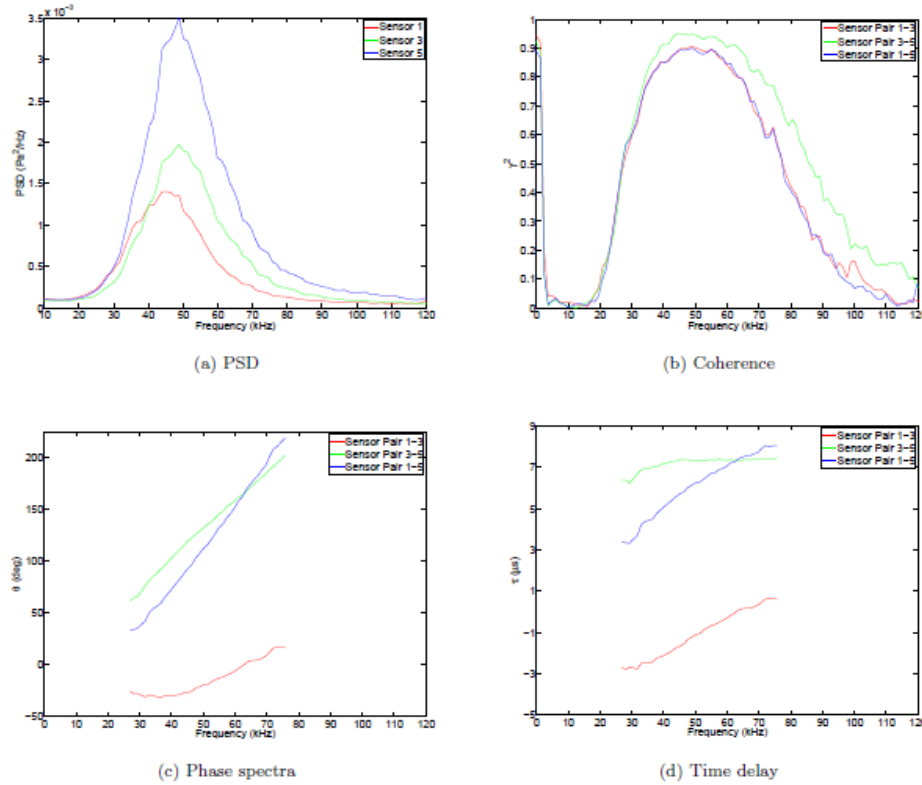


Figure 84 Typical PSD, Coherence, Phase Angle and Time Delay

Figure 85 shows Ψ and c_r for $Re=6.8 \times 10^6$ to 9.0×10^6 /m. Additionally, a few computational data points for traveling crossflow are shown.⁹¹ For portions of the spectra with low coherence (≤ 0.2), there are little or no correlated disturbances common among the sensors, and derived quantities such as Ψ and c_r are meaningless. The coherence was typically greatest for $25 \leq f \leq 80$ kHz and insignificant outside this band. Thus, Ψ and c_r are shown only for this frequency band.

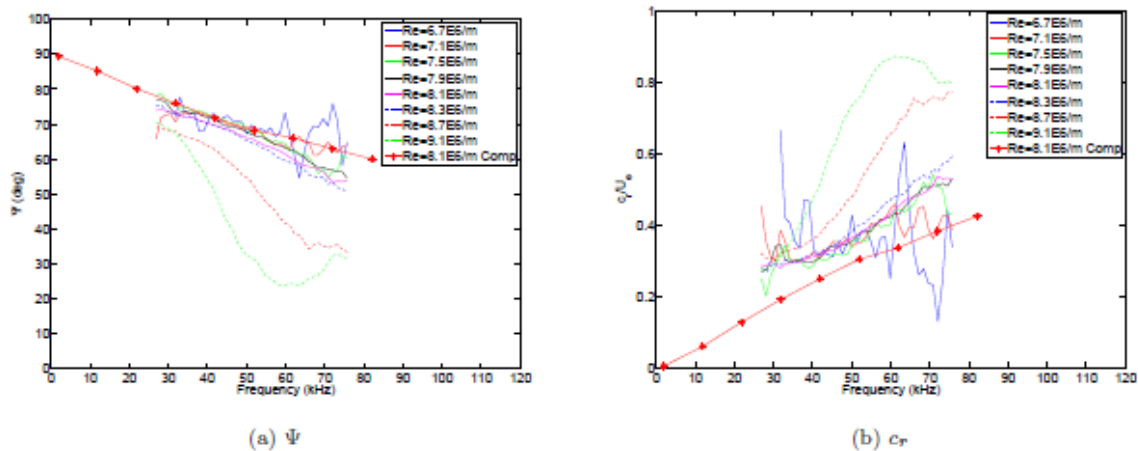


Figure 85 Wave Angle and Phase Velocity for Traveling Crossflow Instability

Here, Ψ is the direction of propagation of wavefronts with respect to the x axis. Thus, for a wave angle of $\Psi=70^\circ$, lines tangent to the wavefronts are inclined 20° with respect to the x axis, and propagate in an outward direction inclined 20° downstream of the y axis. As shown in Figure 84a, good agreement among the various Reynolds numbers and with the computational curve is seen for $6.8 \leq Re \leq 8.5 \times 10^6$ /m. For the two highest Reynolds numbers shown, $Re=8.9$ and 9.0×10^6 /m, the curves diverge significantly from those in good agreement with each other. This attributed to nonlinear processes becoming significant at these higher Reynolds numbers. Evaluation of the cross spectrum assumes linear processes. When nonlinear effects become significant, this assumption is no longer valid and the resultant quantities lose significance. The observed nonlinearities are further investigated and discussed below.

In the range of 30 to 55 kHz, the experimentally calculated values of Ψ for $Re=6.8 \times 10^6$ to 8.5×10^6 /m match both the values and slope of the computations. Above 55 kHz, the computational values of Ψ depart from the nearly linear trend with frequency exhibited for lower frequencies. Here, the computational values depart from the experimental wave angles by as much as 15%. In the range of 30 to 55 kHz, the computationally calculated values of c_r vary from 35% at 30 kHz and decrease to about 15% below the experimental values at 55 kHz. For frequencies above 55 kHz, the difference increases to about 25%.

For both Ψ and c_r , the curves for $Re=6.8 \times 10^6$ to 8.5×10^6 /m show good agreement among themselves, even though they differ from the computational values. It is somewhat surprising that the wave angles over a range of Reynolds numbers and disturbance frequency agree so well with the computational values, while the experimental c_r is markedly higher than the computation for all frequencies and Reynolds numbers.

The reason for this discrepancy is unknown, but is possibly due to experimental uncertainties such as sensor hole locations and the fact that sensors do not provide point measurements, but rather an integrated value over a finite area. For both Ψ and c_r , the curves for $Re=6.8 \times 10^6 /m$ show a considerable amount of scatter. This is because the surface pressure signature of the traveling crossflow waves is very small at this low Reynolds number, resulting in low coherence and more scatter in the measured values of Ψ and c_r .

Neither Ψ nor c_r seem to exhibit any major dependence on Reynolds number for $Re=6.8 \times 10^6$ to $8.5 \times 10^6 /m$. It does appear that Ψ becomes slightly more sensitive to frequency as Re increases. The lack of any significant dependence on Reynolds number is possibly due to the fairly narrow Reynolds number range for which nonlinear processes are absent and for which the crossflow waves are of measureable amplitude, $Re=6.8 \times 10^6$ to $8.5 \times 10^6 /m$. This is a fairly modest increase in Re of only 24%. If the boundary layer thickness scales with $1/\sqrt{Re}$, this is a decrease in boundary layer thickness of only 10%. If Ψ and c_r scale with the boundary layer thickness, changes in these quantities could be overwhelmed by the uncertainties of the measurements.

8.5. Repeatability at $Re=8.1 \times 10^6 /m$

Repeatability was checked with duplicate runs for all Reynolds numbers. For $Re=8.1 \times 10^6 /m$, 11 separate runs were performed. The results are shown in Figure 86. Figure 86a shows PSDs for 11 runs at $Re=8.1 \times 10^6 /m$. Excellent agreement is shown for the peak frequency of about 45 to 47 kHz. However, the root-mean-square (RMS) amplitude of the disturbance varies by about a factor of 2.8. Runs 25, 29, 32, 33, and 36 were completed over several days with various other runs at different conditions in between them. Runs 37 to 42 were completed consecutively on the same day with a 40-60 minute delay between runs. There is no obvious trend for the RMS amplitudes of the PSDs for runs 25, 29, 32, 33, and 36. Runs 37 to 42 exhibit a clear trend, however. Each subsequent run shows a marked increase in peak amplitude. Over the span of those 6 runs, the amplitude increased by a factor of about 1.9. The exact cause of this apparent amplitude increase is unknown.

It is possible that the change is due to the increasing temperature of the model throughout the course of a day. With each run, the model temperature increases due to convective heating while the air is flowing over the model. It is generally time prohibitive to allow the model to return to room temperature before each subsequent run. The increase in model surface temperature from the beginning of Run 37 to the end of Run 42 is estimated to be on the order of 10 to 15 K, as measured in Ref. 55. It is possible that this temperature increase modifies the calibration of the pressure sensors, causes the model to expand altering the fit of the sensors in the holes and thus the sensor output, or that the increased surface temperature destabilizes the traveling crossflow instability, leading to larger amplitudes.

The Kulite sensors are quoted as being temperature compensated in the range from 299 to 353 K. Per Kulite specifications, in this range, the thermal zero shift is $\pm 1\%$ full scale per 56 K temperature change. The thermal sensitivity change is $\pm 1\%$ per 56 K temperature change. For a 15 K temperature increase, the expected thermal zero shift is about 300 Pa. The calibration slope would change by about 25 Pa/V. The resultant change in the PSD amplitudes from the change in the calibration curve due to a 15 K temperature increase is estimated to be less than 1%. It seems unlikely that shifts in the Kulite calibration due to temperature changes can account for the observed amplitude variations.

It would be somewhat surprising if such modest temperature changes, about 5%, would destabilize the traveling crossflow instability to this degree, a shift in N -factor of about $N=\ln(2.8/1)=1.0$. However, Malik et al.⁸³ found that a large surface temperature increase of about 100 K increased the computed stationary crossflow N -factor by about 10 at Mach 4-5. Scaling these results linearly to the present data suggests an N -factor increase of 1.5.

Although this result suggests that increased surface temperature destabilizes the crossflow instability, the surface temperatures observed by Malik et al. were an order of magnitude larger than those observed during the present experiments. Eppink⁹² found that a small surface temperature increase of 3.9 K at Mach 0.24 increased the N -factor by 0.32. This N -factor change represents an amplitude increase of 38%. The experimentally measured amplitude change was 23%. The findings of Malik and Eppink suggest that the observed PSD amplitude increase in the present experiments may be due to destabilization of the boundary layer by the increased surface temperature. Investigation into this effect is ongoing.

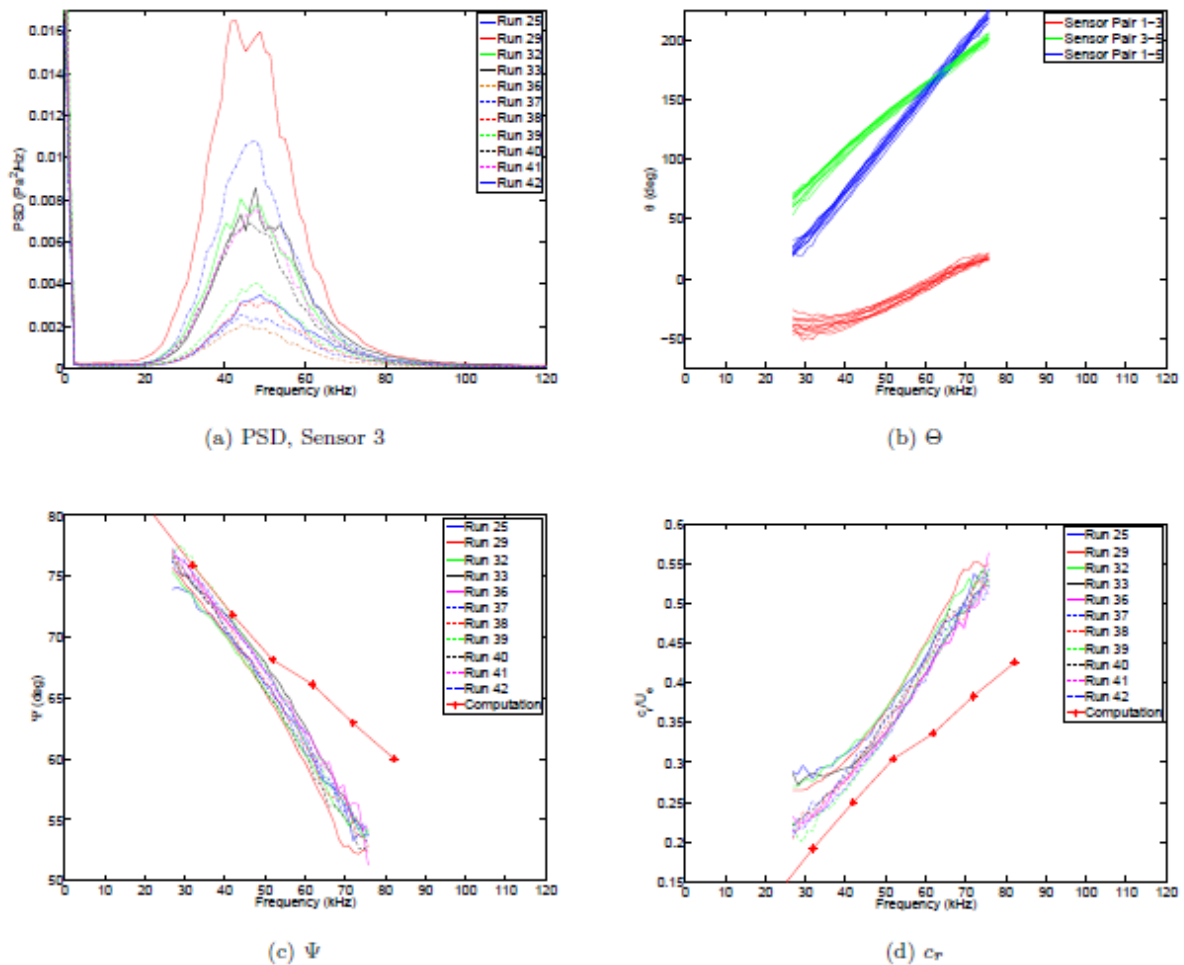


Figure 86 PSD, Phase Angle, Wave Angle and Time Delay for 11 Runs With $Re=8.1 \times 10^6/m$

Figure 86b shows values of Θ_{31} , Θ_{35} , and Θ_{15} for all 11 runs at $Re=8.1 \times 10^6/m$. Here, the subscripted numbers refer to the sensors of interest (e.g. Θ_{31} refers to the phase difference between the signals for sensors 3 and 1). In this case, the band of curves are colored to correspond to the phase delay between two particular sensors. The standard deviation of each Θ

band can be used to give an estimate of experimental uncertainty. Figure 86c and Figure 86d show values of Ψ and c_r , as well as the computational data points, for all 11 runs. As shown, both Ψ and c_r are very repeatable. Excellent agreement with the computation is shown for Ψ for frequencies between 30 to 55 kHz. The agreement is not as good for higher frequencies, but still within about 15% of the computations. The agreement in c_r is not quite as good, but is still close. Table 5 shows the mean, standard deviation, and range of Θ , Ψ , and c_r for the 11 runs. These statistics will be used to quantify uncertainty in the measurements. Despite the large range in PSD amplitude, no such variation is evident in Θ , Ψ , or c_r . There is also no discernible trend in these variables with increasing model temperature. Evidently, if the surface temperature is destabilizing the boundary layer, it does not impact the frequency, phase speed, or wave angle of the traveling crossflow waves.

Table 5 Statistics for 11 repeat runs at $Re=8.1 \times 10^6/m$

	Θ_{31} (deg)	Θ_{35} (deg)	Θ_{51} (deg)	Ψ (deg)	c_r (u/U_e)
Low Value	29.8	101.4	65.0	70.2	0.26
High Value	41.8	110.7	76.44	72.5	0.31
Computational Value	-	-	-	72.4	0.25
Mean	35.2	107.6	72.4	71.2	0.29
Standard Deviation	3.8	3.1	3.6	0.7	0.02

8.6. Noisy Flow

The freestream noise level was increased to “conventional” levels and a Reynolds number sweep from $Re=0.4$ to $5.5 \times 10^6/m$ was performed. Traveling crossflow waves were expected since they were observed at the lower “quiet” freestream noise level. Figure 87 shows PSDs for all noisy Reynolds numbers. Two quiet PSDs are also included for reference. The quiet $Re=8.3 \times 10^6/m$ condition represents laminar flow with large traveling crossflow waves. The quiet $Re=12.4 \times 10^6/m$ case demonstrates a turbulent model boundary layer with quiet freestream flow. A PSD of the sensor output with quiescent air at vacuum, representative of the electronic noise floor, is also shown. The $Re=0.4 \times 10^6/m$ condition represents the lowest Reynolds number at which the BAM6QT can operate.

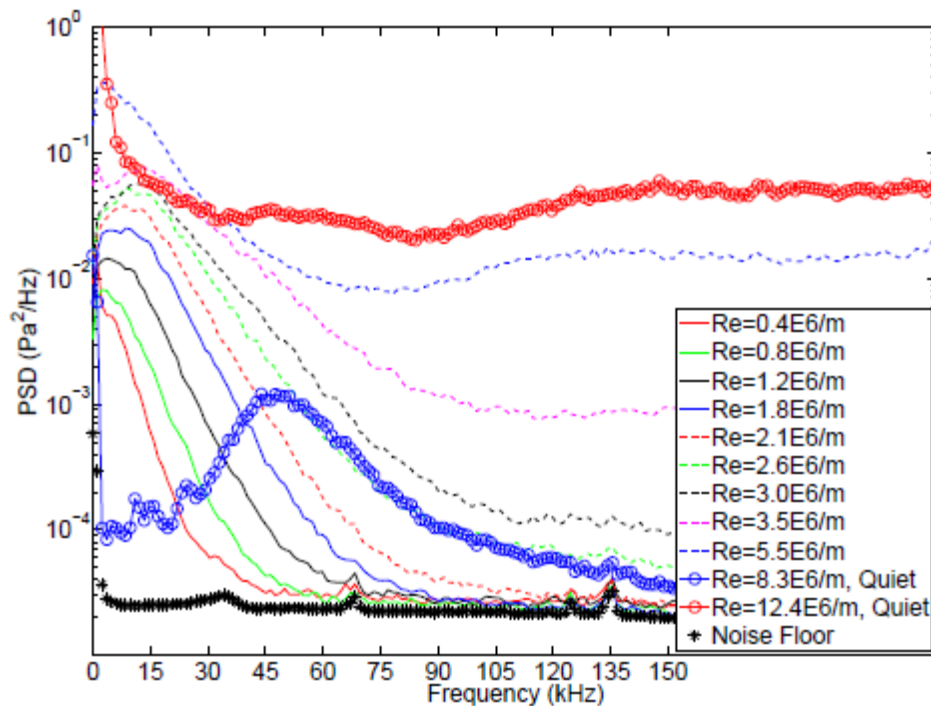


Figure 87 PSD for Noisy Flow, $Re = 0.4\text{-}5.5 \times 10^6/\text{m}$, Sensor 3

The spectrum for this condition is likely laminar since the power drops quickly from its initial value at 0 kHz to the electronic noise floor for frequencies greater than about 40 kHz. The highest Reynolds number condition, $Re=5.5 \times 10^6/\text{m}$ appears to be nearly turbulent since it approaches the quiet, $Re=12.4 \times 10^6/\text{m}$ turbulent spectrum. Although spectra with elevated freestream noise are shown spanning from fully laminar to fully turbulent conditions, there is no evidence of the prominent 40 to 50 kHz traveling waves seen with quiet flow. This lack of traveling crossflow waves is surprising.

The initial amplitudes of traveling crossflow waves are determined by vortical disturbances in the incoming flow.⁷⁵ With elevated freestream noise, the freestream Reynolds number is considerably below that for which traveling crossflow waves were measured in quiet flow. It is possible that the traveling crossflow growth rates at these reduced freestream Reynolds numbers are so low that traveling crossflow waves do not amplify sufficiently to be measured prior to boundary layer transition. Additionally, the freestream vortical disturbances at these reduced Reynolds numbers may be of lower amplitude than for the higher Reynolds number quiet cases, giving the traveling crossflow a lower initial amplitude. The absence of observable traveling crossflow waves in noisy flow while they are prominent in quiet flow is different from what has been observed for the second mode instability on a circular cone. In this case, second mode waves are seen in both noisy and quiet flow at the same Reynolds number in Purdue's tunnel. However, the amplitude of the second-mode waves is about 2 orders of magnitude lower for quiet flow than noisy flow.⁹³

This explanation accounts for the lack of measured traveling crossflow waves, but does not account for the transition mechanism. It seems evident that at this reduced Reynolds number and

increased freestream noise, the dominant transition mechanism is not the traveling crossflow instability. In a previous study,⁸⁸ stationary crossflow vortices were seen in oil flow for noisy flow at higher Reynolds numbers than those in the present experiments, but never in the TSP images. This behavior implies that the stationary crossflow modes in noisy flow do not reach the amplitudes that they do in quiet flow. Under noisy flow, transition is not caused by traveling crossflow instabilities. Under noisy flow, transition appears to be the result of broadband growth of lower-frequency disturbances. The precise nature of the lower-frequency disturbances is uncertain and remains under investigation.

8.7. Summary and Conclusions for HIFiRE-5 Ground Test

A traveling crossflow instability was clearly measured for the HIFiRE-5 in quiet flow using surface-mounted pressure sensors. The frequency, phase speed, and wave angle were measured and were all in good agreement with computations. The peak frequency at $Re=8.3 \times 10^6 /m$ shows good repeatability. The amplitudes of the PSDs were shown to increase over the course of a day. This increase is thought to be due to the increasing model surface temperature with each subsequent run. It is possible that the increased surface temperature destabilizes the traveling crossflow instability.

The traveling crossflow waves were observed to undergo a period of what appears to be primarily linear growth over a Reynolds number range from about 6.8×10^6 to $8.5 \times 10^6 /m$ for sensor 5. Bispectral analysis showed some nonlinear interactions for $8.9 \times 10^6 < Re < 9.8 \times 10^6 /m$, but not at frequencies corresponding to the peak traveling crossflow frequency. Higher Reynolds numbers then led to transition onset and turbulent flow. For the freestream Reynolds numbers showing no nonlinear processes, wave angle and phase speed matched the computations well over a range of frequencies. When nonlinear effects became significant, both wave angle and phase speed diverged considerably from the values observed for lower Reynolds numbers. The lack of nonlinear interactions involving the peak traveling crossflow frequency suggests that, although traveling crossflow disturbances are prominent in the surface pressure spectrum, they may not play a dominant role in the transition process.

No traveling crossflow waves were observed in noisy flow. This is thought to be due to a smaller area of the model being unstable to the traveling crossflow instability at the lower Reynolds numbers for which the model boundary layer was laminar with noisy flow. The dominant instability mechanism for low Reynolds number noisy flow is unknown, but analysis is ongoing.

9. References

- 1 Dolvin, D. "Hypersonic International Flight Research and Experimentation (HIFiRE) Fundamental Science and Technology Development Strategy," AIAA Paper 2008-2581, April 2008.
- 2 Dolvin, D. J., "Hypersonic International Flight Research and Experimentation Technology Development and Flight Certification Strategy," AIAA paper 2009-7228, October 2009.
- 3 Kimmel, R. L., Adamczak, D., Gaitonde, D., Rougeux, A., Hayes, J. R., "HIFiRE-1 Transition Experiment Design," AIAA paper 2007-0534, January 2007.
- 4 Wadhams, T. P., MacLean, M. G., Holden, M.S., and Mundy, E., "Pre-Flight Ground Testing of the Full-Scale FRESH FX-1 at Fully Duplicated Flight Conditions," AIAA paper 2007-4488, June 2007.
- 5 Johnson, H. B., Alba, C. R., Candler, G. V., MacLean, M., Wadhams, T, and Holden, M. "Boundary Layer Stability Analysis of the Hypersonic International Flight Research Transition Experiments," *AIAA Journal of Spacecraft and Rockets*, vol. 45, no. 2, March-April 2008, pp 228-236.
- 6 Holden, M. S., Wadhams, T. P., MacLean, M., "Experimental Studies in the LENS Supersonic and Hypersonic Tunnels for Hypervelocity Vehicle Performance and Code Validation," AIAA paper 2008-2505, April 2008.
- 7 Kimmel, R. L., "Aerothermal Design for the HIFiRE-1 Flight Vehicle," AIAA paper 2008-4034, June 2008.
- 8 Casper, K. M., Wheaton, B. M., Johnson, H. B., and Schneider, S. P., "Effect of Freestream Noise on Roughness-Induced Transition at Mach 6," AIAA paper 2008-4291 June 2008.
- 9 Kimmel, R. L., "Roughness Considerations for the HIFiRE-1 Vehicle," AIAA Paper 2008-4293, June 2008.
- 10 Alba, C. R., Johnson, H. B., Bartkowicz, M. D., Candler, G. V., and Berger, K. T. "Boundary- Layer Stability Calculations for the HIFiRE-1 Transition Experiment," *AIAA Journal of Spacecraft and Rockets*, vol. 45, no. 6, November-December 2008, pp. 1125-1133.
- 11 Wadhams, T. P., Mundy, E., MacLean, M. G., and Holden, M. S., "Ground Test Studies of the HIFiRE-1 Transition Experiment Part1: Experimental Results," *AIAA Journal of Spacecraft and Rockets*, vol. 45, no. 6, November-December 2008, pp. 1134-1148.
- 12 MacLean, M., Wadhams, T., Holden, M., and Johnson, H., "Ground Test Studies of the HIFiRE-1 Transition Experiment Part 2: Computational Analysis," *AIAA Journal of Spacecraft and Rockets*, vol. 45, no. 6, November-December 2008, pp. 1149-1164.
- 13 Berger, K. T., Greene, F. A., Kimmel, R. L., Alba, C., and Johnson, H., "Erratum on Aerothermodynamic Testing and Boundary-Layer Trip Sizing of the HIFiRE Flight 1 Vehicle," *AIAA Journal of Spacecraft and Rockets*, vol. 46, no., 2, March-April, 2009, pp. 473- 480.
- 14 Adamczak, D., Alesi, H., Frost, M., "HIFiRE-1: Payload Design, Manufacture, Ground Test, and Lessons Learned," AIAA paper 2009-7294, October 2009.
- 15 Li, F., Choudhari, M., Chang, C., Kimmel, R., Adamczak, D., "Transition Analysis for the HIFiRE-1 Flight Experiment," AIAA paper 2011-3414, June 2011.
- 16 Kimmel, R. L., Adamczak, D., and Brisbane DSTO-AVD Team, "HIFiRE-1 Preliminary Aerothermodynamic Experiments," AIAA paper 2011-3413, June 2011.
- 17 Stanfield, S. A., Kimmel, R. L., and Adamczak, D., "HIFiRE-1 Data Analysis:

- Boundary Layer Transition Experiment During Reentry,” AIAA paper 2012-1087, January 2012.
- 18 Kimmel, R. L., Adamczak, D., Stanfield, S., Borg, M., “Analysis of HIFiRE-1 Transition Data,” NATO Research and Technology Agency, Specialists Meeting AVT-200/RSM-030 on Hypersonic Laminar-Turbulent Transition, paper MP-AVT-200-02, San Diego, CA, 14-17 May 2012
 - 19 Stanfield, S., Kimmel, R. L., and Adamczak, D., “HIFiRE-1 Flight Data Analysis: Turbulent Shock-Boundary-Layer Interaction Experiment During Ascent,” AIAA paper 2012-2703, June 2012.
 - 20 Stanfield, S. A., and Kimmel, R. L., “Compensation Method for the Estimation of the Autospectral Density Function of the Unevenly Spaced HIFiRE-1 Flight Data,” AIAA paper 2013-3169, June 2013.
 - 21 Brown, M. S., and Barhorst, T. F., “Post-Flight Analysis of the Diode-Laser-Based mass Capture Experiment Onboard HIFiRE Flight 1,” AIAA paper 2011-2359, April 2011.
 - 22 “NASA Sounding Rocket Program Handbook,” 810-HB-SRP, Sounding Rockets Program Office, Suborbital & Special Orbital Projects Directorate, Goddard Space Flight Center, Wallops Island Flight Facility, June 2005.
 - 23 Smart, M. K., Hass, N. E., and Paull, A., “Flight Data Analysis of the HyShot 2 Scramjet Flight Experiment,” AIAA Journal, vol. 44, no. 10, October 2006, pp. 2366-2375.
 - 24 Walker, S., and Rodgers, F., “The Hypersonic Collaborative Australia/United States Experiment (HyCAUSE),” AIAA paper 2005-3254, May 2005.
 - 25 Wiesel W. E., Spaceflight Dynamics, 2nd Ed., McGraw-Hill Series in Aeronautical and Aerospace Engineering, McGraw-Hill, pp. 138-140, 1997.
 - 26 Adamczak, D., Kimmel, R. L., Paull, A., Alesi, H., “HIFiRE-1 Flight Trajectory Estimation and Initial Experimental Results,” AIAA paper 2011-2358, May 2011
 - 27 National Institute of Standards and Technology, “NIST Standard Reference Database 60, Version 2.0 (Web Version),” *NIST ITS-90 Thermocouple Database* [online database], URL: <http://srdata.nist.gov/its90/main/> [cited 4 March 2013].
 - 28 Boyd, C. F., and Howell, A., “Numerical Investigation of One-Dimensional Heat-Flux Calculations,” Naval Surface Warfare Center report NSWCDD/TR-94/114, 25 October 1994.
 - 29 Aerospace Specification Metals Inc., [online database], URL: <http://asm.matweb.com/search/SpecificMaterial.asp?bassnum=MA6061T6>, cited 26 March 2013.
 - 30 Aerospace Specification Metals Inc., [online database], URL: <http://www.matweb.com/search/DataSheet.aspx?MatGUID=14c0da863d264998a97f0be6a0f92c70>, cited 26 March 2013.
 - 31 Thompson, P. A., Compressible Fluid Dynamics, McGraw-Hill Book Company, New York, New York, 1972, pp. 487-490.
 - 32 Buchanan, T. D., Jenke, L. M., Chaney, M. J., “Dynamic Force Measurements and Boundary- Layer Transition Mapping on a Spinning 9-deg Cone With and Without Mass Addition at Mach Numbers 5 and 8,” Arnold Engineering Development Center Technical Report, AEDC – TR-78-40, August 1978, Arnold AFB, TN.
 - 33 Eckert, E. R. G., “Engineering Relations for Friction and Heat Transfer to Surfaces in High Velocity Flow,” *Journal of the Aeronautical Sciences*, vol. 22, Aug., 1955, pp. 585-587.
 - 34 Van Driest, E. R., “Turbulent Boundary Layer in Compressible Fluids,” *Journal of the*

- Aeronautical Sciences*, vol. 18, no. 3, March 1951, pp. 145-160, 216.
- 35 Schneider, S. P., "Effects of Roughness on Hypersonic Boundary Layer Transition," *AIAA Journal of Spacecraft and Rockets*, vol. 45, no. 2, March-April 2008
 - 36 Johnson, H. B., and Candler, G. V., "PSE Analysis of Reacting Hypersonic Boundary Layer Transition," AIAA 99-3793, June 1999.
 - 37 Malik, M. R., "Hypersonic Flight Transition Data Analysis Using Parabolized Stability Equations with Chemistry Effects," *Journal of Spacecraft and Rockets*, vol. 40, no. 3, May-June 2003.
 - 38 Johnson, H. B., Candler, G. V., "Analysis of Laminar-Turbulent Transition in Hypersonic Flight Using PSE-Chem," AIAA paper 2006-3057, June 2006
 - 39 Casper, K. M., Beresh, S. J., Henfling, J. F., Spillers, R. W., Pruett, B., and Schneider, S. P., "Hypersonic Wind-Tunnel Measurements of Boundary-Layer Pressure Fluctuations," AIAA paper 2009-4054, June 2009.
 - 40 Stetson, K. F., "Boundary-Layer Separation on Slender Cones at Angles of Attack," *AIAA Journal*, vol. 10, pp. 642-648, 1972.
 - 41 Juliano, T. J., Kimmel, R. L., Willems, S. Gülhan, A., and Schneider, S. P., "Surface Pressure Fluctuation Measurements from High Reynolds, High Angle HIFiRE-1 Ground Test," AIAA paper 2014-0429, January 2014.
 - 42 Willems, S., Gülhan, A., Juliano, T. J., Kimmel, R. L., and Schneider, S. P., "Laminar to turbulent transition on the HIFiRE-1 cone at Mach 7 and high angle of attack," AIAA 2014-0428, January 2014.
 - 43 Stetson, K., F., "Mach 6 Experiments of Transition on a Cone at Angle of Attack," *Journal of Spacecraft and Rockets*, vol. 19, no. 5, Sep.-Oct. 1982, pp. 397-403.
 - 44 Reda, D. C., "Boundary-Layer Transition Experiments on Sharp, Slender Cones in Supersonic Free Flight," *AIAA Journal*, vol. 17, no. 8, August 1979, pp. 803-810.
 - 45 Stetson, K. F., and Rushton, G. H., "Shock Tunnel Investigation of Boundary-Layer Transition at $M=5.5$," *AIAA Journal*, vol. 5, no. 5, May 1967, pp. 899-906.
 - 46 Holden, M. S., "Experimental Studies of the Effects of Asymmetric Transition on the Aerothermal Characteristics of Hypersonic Blunted Slender Cones," AIAA paper 1985-0325, January 1985.
 - 47 Holden, M. S., Bower, D., and Chadwick, K., "Measurements of Boundary Layer Transition on Cones at Angle of Attack for Mach Numbers from 11 to 13," AIAA-95-2294, June 1995.
 - 48 DiCristina, V., "Three-Dimensional Boundary Layer Transition on a Sharp 80 Cone at Mach 10," *AIAA Journal*, vol. 8, no. 5, May 1970, pp. 852-856.
 - 49 Muir, J. F., and Trujillo, A. A., "Experimental Investigation of the Effects of Nose Bluntness, Free-Stream Unit Reynolds Number, and Angle of Attack on Cone Boundary layer Transition at a Mach Number of 6," AIAA paper 72-216, January, 1972.
 - 50 Mack, L. M., "Boundary-Layer Stability Theory," *Special Course on Stability and Transition of Laminar Flow*, edited by R. Michel, AGARD Report No. 709, pp. 3-1 to 3-81, 1984.
 - 51 Li, F., Choudhari, M., Chang, C., White, J., Kimmel, R., Adamczak, D., Borg, M., Stanfield, S., and Smith, M., "Stability Analysis for HIFiRE Experiments," AIAA paper, 42nd AIAA Fluid Dynamics Conference and Exhibit, New Orleans, June 25-28, 2012.
 - 52 Dolling, D. S., "Unsteadiness of Shock-Induced Turbulent Separated Flows – Some Key Questions," AIAA paper 2001-2708, June 2001.

- 53 Kimmel, R. L., Adamczak, D., Berger, K., and Choudhari, M., "HIFiRE-5 Flight Vehicle Design," AIAA paper 2010-4985, June 2010
- 54 Palmerio, A. F.; Peres da Silva, J. P. C.; Turner, P.; Jung, W., "The development of the VSB-30 sounding rocket vehicle," in 16th ESA Symposium on European Rocket and Balloon Programmes and Related Research, 2 - 5 June 2003. Ed.: Barbara Warmbein. ESA SP-530, Noordwijk: ESA Publications Division, 2003, p. 137 – 140.
- 55 "NASA Sounding Rocket Program Handbook," 810-HB-SRP, Sounding Rockets Program Office, Suborbital & Special Orbital Projects Directorate, Goddard Space Flight Center, Wallops Island Flight Facility, June 2005.
- 56 Kimmel, R. L., and Poggie, J., "Transition on an Elliptic Cone at Mach 8," American Society of Mechanical Engineers ASME FEDSM97-3111, June 1997.
- 57 Kimmel, R. L., and Poggie, J., "Three-Dimensional Hypersonic Boundary Layer Stability and Transition," Air Force Research Laboratory Technical Report, WL-TR-97-3111, December 1997, Wright-Patterson Air Force Base, Ohio.
- 58 Kimmel, R. L., and Poggie, J., Schwoerke, S. N., "Laminar-Turbulent Transition in a Mach 8 Elliptic Cone Flow," AIAA Journal, vol. 37, no. 9, Sep. 1999, pp. 1080-1087.
- 59 Schmisseeur, J. D., "Receptivity of the Boundary Layer on a Mach-4 Elliptic Cone to Laser-Generated Localized Freestream Perturbations," Doctoral Dissertation, Purdue University Aerospace Sciences Laboratory, December 1997.
- 60 Holden, M., "Experimental Studies of Laminar, Transitional, and Turbulent Hypersonic Flows Over Elliptic Cones at Angle of Attack," Air Force Office of Scientific Research Technical Report AFRL-SR-BL-TR-98-0142, Bolling Air Force Base, DC, 1998.
- 61 Schmisseeur, J. D., Schneider, S. P., and Collicott, S. H., "Receptivity of the Mach 4 Boundary Layer on an Elliptic Cone to Laser-Generated Localized Freestream Perturbations," AIAA paper 1998-0532, January 1998.
- 62 Schmisseeur, J. D., Schneider, S. P., and Collicott, S. H., "Response of the Mach 4 boundary layer on an elliptic cone to laser-generated freestream perturbations," AIAA paper 1999-0410, January 1999.
- 63 Lytle, I. J., and Reed, H. L., "Use of Transition Correlations for Three-Dimensional Boundary Layers Within Hypersonic Flows," AIAA-95-2293, June 1995.
- 64 Löhle, S., Böhrk, H., Fuchs, U., Kraetzig, B., and Weihs, H., "Three-Dimensional Thermal Analysis of the HIFiRE-5 Ceramic Fin," AIAA paper 2012-5920, September 2012.
- 65 Berger, K. T., Rufer, S. J., Kimmel, R. and Adamczak, D., "Aerothermodynamic Characteristics of Boundary Layer Transition and Trip Effectiveness of the HIFiRE Flight 5 Vehicle," AIAA paper 2009-4055, June 2009.
- 66 Kimmel, R. L., Adamczak, D., and Brisbane DSTO-AVD Team, "HIFiRE-1 Preliminary Aerothermodynamic Experiments," AIAA paper 2011-3413, June 2011.
- 67 Bushnell, D. M., and Huffman, J. K., "Investigation of Heat Transfer to Leading Edge of a 760 Swept Fin With and Without Chordwise Slots and Correlations of Swept-Leading-Edge Transition Data for Mach 2 to 8," NASA TM X-1475, December 1967.
- 68 Murakami, A., Stanewsky, E., and Krogman, P., "Boundary-layer Transition on Swept Cylinders at Hypersonic Speeds," *AIAA Journal*, vol. 34, no. 4, April 1996, pp. 649-654.
- 69 Choudhari, M., Chang, C.-L., Jentink, T., Li, F., Berger, K., Candler, G., and Kimmel, R., "Transition Analysis for the HIFiRE-5 Vehicle," AIAA paper 2009-4056, June 2009.
- 70 Gosse, R., Kimmel, R. L., and Johnson, H. B., "CFD Study of the HIFiRE-5 Flight

- Experiment," AIAA paper 2010-4854, June 2010.
- 71 Borg, M. P., Kimmel, R. L., Stanfield, S., "Crossflow Instability for HIFiRE-5 in a Quiet Hypersonic Wind Tunnel," AIAA paper 2012-2821, June 2012
 - 72 Li, F., Choudhari, M., Chang, C.-L., White, J., Kimmel, R., Adamczak, D., Borg, M., Stanfield, S., and Smith, M., "Stability Analysis for HIFiRE Experiments," AIAA paper 2012-2961, June 2012.
 - 73 Malik, M., Li, F., and Chang, C.-L., "Crossflow disturbances in three-dimensional boundary layers: nonlinear development, wave interaction and secondary instability," *Journal of Fluid Mechanics*, Vol. 268, 1994, pp. 1–36.
 - 74 Saric, W. S. and Reed, H. L., "Crossflow Instabilities- Theory & Technology," AIAA paper 2003-0771, Jan. 2003.
 - 75 Bippes, H., "Basic experiments on transition in three-dimensional boundary layers dominated by crossflow instability," *Progress in Aerospace Sciences*, Vol. 35, 1999, pp. 363-412.
 - 76 Saric, W. S. and Reed, H. L., "Supersonic Laminar flow control on swept wings using distributed roughness," AIAA paper 2002-0147, Jan. 2002.
 - 77 Bippes, H. and Lerche, T., "Transition Prediction in Three-Dimensional Boundary-Layer Flows Unstable to Crossflow Instability," AIAA paper 97-1906, 1997.
 - 78 Carpenter, M. H., Choudhari, M., Li, F., Streett, C. L., and Chang, C.-L., "Excitation of Crossflow Instabilities in a Swept Wing Boundary Layer," Paper 2010-0378, AIAA, January 2010.
 - 79 Eppink, J. and Wlezien, R., "Observations of traveling crossflow resonant triad interactions on a swept wing," Paper 2012-2820, AIAA, June 2012.
 - 80 White, E. B. and Saric, W. S., "Secondary instability of crossflow vortices," *Journal of Fluid Mechanics*, Vol. 525, 2005, pp. 275-308.
 - 81 King, R., "Three-dimensional boundary-layer transition on a cone at Mach 3.5," *Experiments in Fluids*, Vol. 13, No. 4, 1992, pp. 305-314.
 - 82 Poggie, J., Kimmel, R. L., and Schwoerke, S. N., "Traveling Instability Waves in a Mach 8 Flow over an Elliptic Cone," *AIAA Journal*, Vol. 38, No. 2, 2000, pp. 251–258.
 - 83 Malik, M. R., Li, F., and Choudhari, M., "Analysis of Crossflow Transition Flight Experiment Aboard the Pegasus Launch Vehicle," AIAA paper 2007-4487, June 2007.
 - 84 Swanson, E. O. and Schneider, S. P., "Boundary-layer transition on cones at angle of attack in a Mach-6 quiet tunnel," Paper 2010-1062, AIAA, January 2010.
 - 85 Juliano, T. J. and Schneider, S. P., "Instability and Transition on the HIFiRE-5 in a Mach-6 Quiet Tunnel," AIAA paper 2010-5004, June 2010.
 - 86 Schneider, S. P., "Design of a Mach-6 quiet-flow wind-tunnel nozzle using the e**N method for transition estimation," AIAA paper 98-0547, Jan. 1998.
 - 87 Beresh, S. J., Hening, J., Spillers, R., and Pruett, B., "Measurements of Fluctuating Wall Pressures Beneath a Supersonic Turbulent Boundary Layer," Paper 2010-0305, AIAA, January 2010.
 - 88 Borg, M. P., Kimmel, R. L., and Stanfield, S., "HIFiRE-5 Attachment-line transition in a Quiet Hypersonic Wind Tunnel," Paper 2011-3247, AIAA, June 2011.
 - 89 Schneider, S. P., Collicott, S. H., Schmisser, J. D., Ladoon, D., Randall, L. A., Munro, S. E., and Salyer, T. R., "Laminar-turbulent transition research in the Purdue Mach-4 Quiet-Flow Ludwig Tube," AIAA paper 96-2191, June 1996.

- 90 Bendat, J. and Piersol, A., *Engineering Applications of Correlation and Spectral Analysis*, Wiley-Interscience, 1980.
- 91 Choudhari, M., Private communication, Aug. 2012.
- 92 Eppink, J. and Wlezien, R., "Data analysis for the NASA/Boeing hybrid laminar flow control crossflow experiment," Paper 2011-3879, AIAA, June 2011.
- 93 Estorf, M., Radespiel, R., Schneider, S. P., Johnson, H. B., and Hein, S., "Surface-pressure measurements of second-mode instability in quiet hypersonic flow," Paper 2008-1153, AIAA, January 2008.

List of Acronyms, Abbreviations, Symbols

A	= disturbance amplitude, dimensionless
A_0	= disturbance amplitude at lower neutral bound, dimensionless
C_h	= heat transfer coefficient (Stanton number), $\dot{q}/\rho_\infty U_\infty (H_0 - H_w)$, dimensionless
C_p	= specific heat, J/kg K
f	= frequency, dimensions as noted
G_{xx}	= autospectral density function of pressure fluctuations, kPa ² /Hz
h	= altitude, m
H	= specific enthalpy, J/kg
k	= thermal conductivity, W/mK, or roughness height, m
L	= reference length from stagnation point to flare /cylinder corner, 1.6013 m full scale
M	= Mach number, dimensionless
N	= $\ln[A(f)/A_0(f)]$, dimensionless
p	= pressure, kPa
p'	= fluctuating pressure (instantaneous departure from local mean), kPa
δp	= pressure zero-shift at $t=60$ seconds, kPa
\dot{q}	= heat transfer rate, W/m ² , or kW/m ² as noted
Re	= freestream unit Reynolds number per meter, $\rho_\infty U_\infty / \mu_\infty$
s	= streamwise surface arc length from stagnation point, m
t	= time after liftoff, seconds
T	= temperature, K
U	= magnitude of the velocity vector, m/s
v	= velocity component normal to missile x -axis, m/s
x	= distance from stagnation point along vehicle centerline, m
y	= vertical (pitch-plane) coordinate, or depth below model wetted surface m
α	= thermal diffusivity, $k/\rho C_p$, m ² /s, or angle of attack, degrees
Φ	= wind-fixed angular coordinate around vehicle circumference, $\Phi=0$ on windward stagnation line, degrees
ϕ	= body-fixed angular coordinate around vehicle circumference, $\phi=0$ on primary instrumentation ray, degrees
ρ	= density, kg/m ³
μ	= viscosity, N s/m ²

Subscripts

0	= stagnation conditions
ad	= recovery temperature
e	= evaluated at boundary layer edge
H	= high-frequency band
kk	= evaluated using conditions at roughness height, with roughness height as length scale
L	= low frequency band
l	= lower neutral bound
m	= measured in flight
tr	= transition location
w	= evaluated at model wall
x	= evaluated at distance x from stagnation point
∞	= freestream conditions, upstream of model bow shock

Acronyms

AoA	Angle of Attack
ARC	Ames Research Center
BC	Boundary Condition
BEA	Best Estimated Atmosphere
BET	Best Estimated Trajectory
BLT	Boundary Layer Transition
CUBRC	Calspan University of Buffalo Research Center
dB	Decibel
DLR	Deutsche Zentrum für Luft- und Raumfahrt
DFRC	Dryden Flight Research Center
DSTO	Defence Science and Technology Organisation
GPS	Global Positioning System
HIFiRE	Hypersonic International Flight Research and Experimentation
HT	Heat Transfer
IMU	Inertial Measurement Unit
LaRC	Langley Research Center
PHBW	Pressure High Bandwidth
PLBW	Pressure Low Bandwidth
RANRAU	Royal Australia Navy Ranges and Assessing Unit
RMS	Root Mean Square
SBLI	Shock Boundary Layer Interaction
TLBW	Temperature Low Bandwidth
TM	Telemetry
TZM	Titanium Zirconium Molybdenum
WSMR	White Sands Missile Range

Appendix - HIFiRE Flight 1 Shock-Boundary Layer Interaction Spectral Analysis

The HIFiRE-1 payload was instrumented with numerous thermocouples, heat transfer gauges, and pressure transducers. During flight, these data were digitized using a sampling scheme with a non-constant interval between samples. This sampling scheme was used to achieve maximum stable TM throughput. Although this sampling scheme maximized data acquisition, special care must be taken when performing spectral analysis on such unevenly-sampled data. Power spectra derived from unevenly sampled data are distorted and do not necessarily represent the true spectrum of the physical process. The spectral distortion caused by uneven sampling is independent of the data and depends only on the sampling scheme. This was especially true for the HIFiRE-1 high-bandwidth pressure data, which were sampled at rates up to 60 kHz. In addition, random data dropouts sometimes occurred in the telemetry. Generally however, dropouts were infrequent, and the dominant sampling feature was the uneven sampling rate. This section summarizes the methods used to analyze the high bandwidth pressure data, and quantifies spectral error introduced by uneven sampling.

The least squares (Lomb-Scargle) method determines the Fourier transform by estimating the different sinusoidal components of a time series. Although complicated to develop, the least squares method is robust, requiring very little user input, and it can be applied to any arbitrary sampling scheme. Moreover, the least squares approach has been shown to be more fundamental than the traditional Fourier methods since, for evenly sampled time series data, the two methods are exactly identical. For unevenly-sampled time series, the two methods are identical within the numerical error generated by numerical integration of the Fourier transform. The least-squares method can be useful for accurately computing the Fourier transform of unevenly-sampled, sinusoidal-periodic, complex-periodic, and almost-periodic data. It is not suitable for stochastic time series data with red-noise spectra such as the surface pressure fluctuations underneath boundary layers.

Generally, interpolation methods, slotted resampling methods, and continuous time models introduce unwanted distortion, are not robust, and can require significant user input depending on the time series. Specifically, interpolating methods such as nearest neighbor or spline interpolation underestimate high frequency components.^{1,2,3} Kernel-based interpolation results depend on the interpolation kernel and kernel parameters.⁴ Unlike the least squares method however, these methods are useful for estimating the spectral content of unevenly-sampled, stochastic signals having red-noise spectra.

Slotted resampling, which estimates the autocorrelation function by summing the product pairs $X_i X_j$ into bins lagged by $t_i - t_j$, cannot be employed for an arbitrary sampling scheme. Sufficiently large gaps in the data can cause the method to fail. These gaps could be filled in using interpolation. The interpolation process (if needed) and the binning process both independently distort the time series data. Regardless of these negative attributes, the slotted resampling method may be a useful method for analyzing the HIFiRE-1 data. The use of this method for analyzing the HIFiRE-1 data is still under investigation.

A block diagram representing the sampling process of a continuous function is given in Figure A-1. In Figure A-1, the signal $x(t)$ represents the output from a measurement device such as a pressure transducer and is a continuous function, $x'(t)$ is a band limited function assumed to have the same amplitude and phase spectrum as $x(t)$ for frequencies below the cutoff frequency of the antialiasing filter, $s(t)$ is the sampling function, and $y(t_n)$ is a set of discrete samples of $x'(t)$ sampled at times t_n . The function $x(t)$ is filtered before sampling so that the frequency content of $x'(t)$ is limited to frequencies below the Nyquist frequency, defined as

$$f_c = \frac{1}{2\Delta t} \quad (\text{A-1})$$

where Δt represents the sampling interval. According to the sampling theorem, $x'(t)$ can be reconstructed from $y(t_n)$ without information loss or distortion if the sampling rate is greater than or equal to twice the Nyquist frequency. If the sampling rate is less than twice the Nyquist frequency, spectral leakage from frequencies greater than the Nyquist frequency wrap-around and combine with frequencies below the Nyquist frequency. This problem is known as aliasing and in general cannot be removed.

The sampling function is defined as

$$s(t) = C \frac{\sum_{n=1}^N w_n \delta(t-t_n)}{\sum_{n=1}^N w_n} \quad (\text{A-2})$$

where $\delta(t - t_n)$ is the Dirac delta function, t_n are the sampled times, N is the number of data points, and C and w_n are constants. The discrete signal $y(t_n)$ is given as

$$y(t_n) = s(t)x'(t) = \frac{1}{N} \sum_{n=1}^N x'(t_n) \delta(t - t_n) \quad (\text{A-3})$$

where the constants C and w_n were set equal to 1. The discrete Fourier transform of Equation A-3 is given as

$$Y(f) = S(f) * X'(f) \quad (\text{A-4})$$

where the Fourier transform is defined as

$$Y(f_k) = \int_{-\infty}^{\infty} y(t) e^{2\pi i f_k t} dt \approx \sum_{n=0}^{N-1} y_n e^{2\pi i f_k t_n \Delta t}. \quad (\text{A-5})$$

Typically, the sampling interval is moved outside the summation because it is constant for an evenly sampled time series. In this work, the sampling interval is not necessarily constant and the sampling interval is left within the summation. In Equation A-4, $Y(f)$ is the Fourier transform of $y(t_n)$, $X'(f)$ is the Fourier transform of $x'(t_n)$, and $S(f)$ is the Fourier transform of $s(t)$ and is referred to as the normalized spectral window function. According to Equation A-4, and as pointed out by Deeming⁵, “the pathology of the data distribution is all contained in the spectral window, which can be calculated from the data spacing alone, and does not depend directly on the data themselves.” The discussion will now focus on identifying the source of the distortion in the Fourier transform of unevenly sampled time series data using the normalized spectral window function.

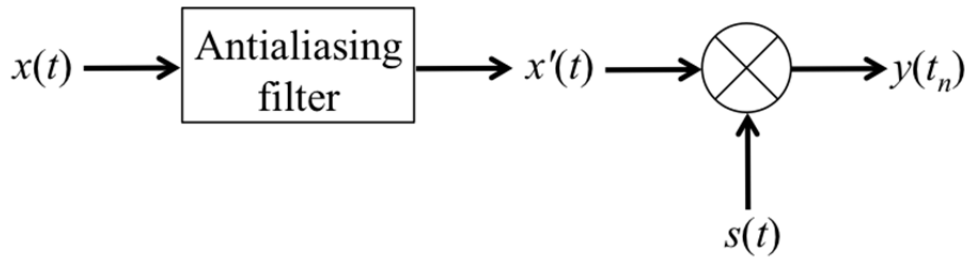


Figure A-1 Block Diagram Depicting the Sampling Process of a Continuous Function

The power spectrum of the spectral window function, defined as $|S(f)|^2$, is shown in Figure A-2 for an evenly sampled time series with a sample rate of 100 Hz. From Figure A-2, the normalized spectral window function has peaks with amplitude of 1 centered at $2nf_c$ where $n = 0, 1, 2 \dots \infty$. Hence, the normalized spectral window function is a periodic function with period $2f_c$. This periodicity is independent of the sample rate.

The power spectrum of the normalized spectral window function for a time series sampled at 200 Hz but with gaps in the data is shown in Figure A-3a. The sampling interval was constant at 0.005 seconds with gaps between 0.250 to 0.500, 0.750 to 1.000, and 1.250 to 1.500 seconds. The power spectrum in Figure A-3a is similar to the power spectrum in Figure A-2 with peaks centered at $2nf_c$, however, there are additional peaks (sidelobes) as shown in Figure A-3b. The magnitude and location of the sidelobes depend on the sampling scheme. These sidelobes cause the real and imaginary components of $Y(f)$ and $X'(f)$ to be different. This difference is referred to within this paper as the distortion in $Y(f)$ caused by the sampling scheme.

The period of the spectral window function for an unevenly-sampled time series is approximately $2f_c$, as shown in Figure A-3a. The spectral window function of an unevenly-sampled time series is not always exactly periodic, as the peaks centered at $2nf_c$ for $n > 0$ are sometimes split into multiple peaks. The frequency separation of the split peaks is very small such that the peaks are centered at approximately $2nf_c$. The peak centers at $2nf_c$ determine the Nyquist frequency of an unevenly sampled time series, since Equation A-1 is invalid when the sampling interval is not constant³³. The significance of the Nyquist frequency determined from the spectral window function is unchanged. Signal content above the Nyquist frequency wraps around, contaminating the Fourier transform below the Nyquist frequency.

An additional aliasing artifact is inherent only to unevenly sampled time series data. For example, let $x'(t) = \cos(2\pi tf)$ with $f = 96$ Hz, and let $y(t_n)$ be the set of discrete samples of $x'(t)$ where the sampling scheme has the normalized spectral window function depicted in Figure A-3a. The Nyquist frequency for this sampling scheme is 100 Hz. The sidelobes centered at 2, 6, and 10 Hz in Figure A-3b are centered at 98, 104, and 106 Hz after convolving $S(f)$ with $X'(f)$. The sidelobes centered at 104 and 106 Hz are greater than the Nyquist frequency and wrap-around to 96 and 94 Hz, respectively. Notice the peak in the power spectrum corresponding to the input signal has a frequency below the Nyquist frequency and does not wrap-around but combines with the sidelobe aliased to 96 Hz. The real and imaginary components of $Y(f)$ at 96 Hz are distorted due to the aliased sidelobe.

Another property of interest is now given. Assume that $x(t)$ is the output of a constant-parameter linear system. If the output of such a system is sampled unevenly, then the overall system is nonlinear. This property is demonstrated with the following example. Let $x'(t) = \cos(2\pi tf)$ with $f = 23$ Hz and let $y(t_n)$ be the set of discrete samples of $x'(t)$ where the sampling scheme has the normalized spectral window function depicted in Figure A-3a. The Fourier transform of $x'(t)$ will be zero everywhere except at $f = 23$ Hz. The Fourier transform of $Y(f)$ according to Equation A-4 is $S(f) * X'(f)$. The power spectrum of $Y(f)$ is shown in Figure A-4. In Figure A-4, the Fourier transform of $Y(f)$ is computed by convolving $S(f)$ with $X'(f)$ and by computing the Fourier transform of $y(t_n)$. The Fourier transform of $y(t_n)$ was computed using the least squares Fourier transform to eliminate numerical integration error. In

Figure A-4, the two methods for computing $Y(f)$ are identical. More importantly, the sampling scheme results in the leakage of power from 23 Hz to sidelobes centered at 13, 17, 21, 25, 29, and 33 Hz. That is, uneven-sampling causes frequency translation and is therefore nonlinear, regardless of whether the transducer has a linear response.

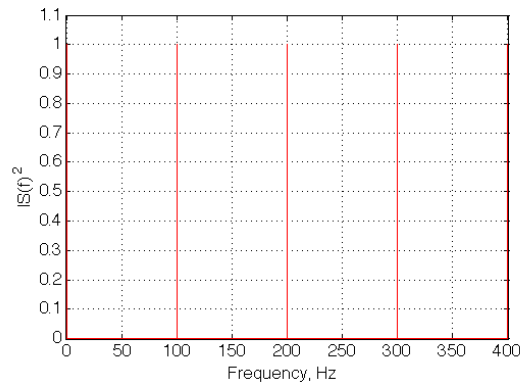


Figure A-2 Power Spectrum of the Normalized Spectral Window Function for an Evenly Sampled Time Series

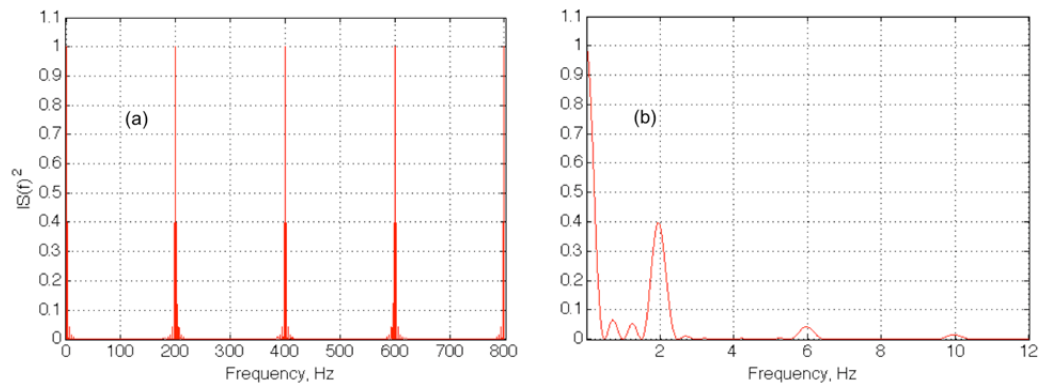


Figure A-3 (a) Power Spectra for the Spectral Window Function of an Unevenly Sampled Time Series, (b) Rescaled View Showing Sidelobes

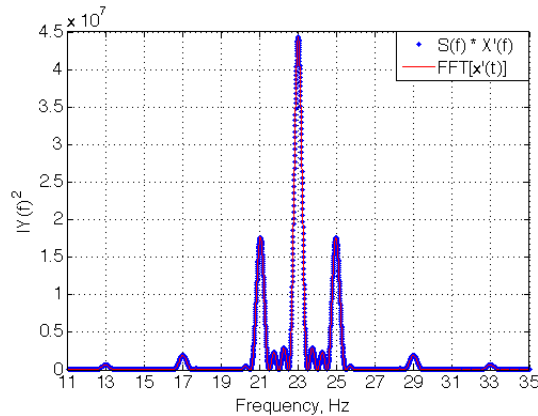


Figure A-4 Power Spectra Computed by Convolving a 23 Hz Sinusoid With the Normalized Spectral Window Function, and by Computing the Fourier Transform of the Unevenly Sampled Time Series

The discussion has so far focused on periodic data. The discussion is now extended to stochastic time series data such as surface pressure data. The power spectra of this type of data will have nonzero power at each resolvable frequency. The frequencies with nonzero power each contribute sidelobes, resulting in significant distortion of the Fourier transform due to the sum contribution of so many sidelobes. The distortion in the Fourier transform of surface pressure measurements underneath a transitional boundary layer is shown in Figure A-5. Evenly-sampled surface pressure data was acquired at a sample rate of 500 kHz³⁵. The corresponding Nyquist frequency was 250 kHz. Two unevenly-sampled time series (USTS) were generated from the evenly-sampled (ESTS) time series by deleting every sixth and every third data point. Each time series was partitioned into 400 segments. The least squares Fourier transform was computed for each segment, and these were averaged. Figure A-5a shows the power spectra of the ESTS and two USTS. In Figure A-5a, the sidelobe distortion is apparent by comparing the amplitude of the ESTS with the amplitudes of the two USTS. A comparison between the phase of the ESTS and one of the USTS is shown in Figure A-5b. In Figure A-5b, the phases of the evenly and unevenly sampled time series are different due to the distortion caused by the sidelobes.

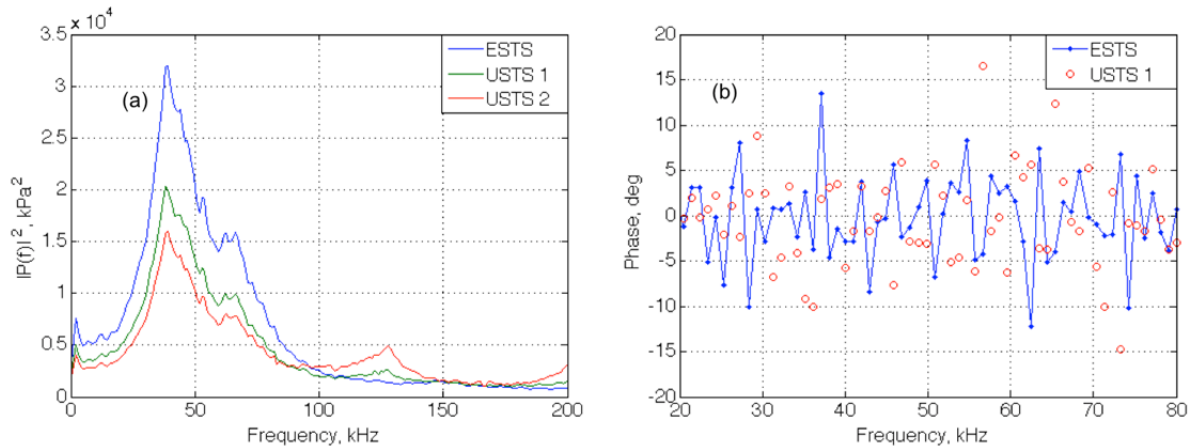


Figure A-5 (a) Power Spectra for ESTS and USTS 1 and USTS 2 of the ESTS, (b) Phase Spectra of the ESTS and USTS

The sampling scheme for the high bandwidth pressure transducers are shown in Figure A-6a-c. The normalized time interval is defined as $\Delta t / \min(\Delta t)$. The sampling scheme for each pressure transducer was periodic. Transducer 12 was sampled at a lower rate than the rest of the transducers located on the cylinder. The sample rate for transducer 12 was well below the cutoff frequency of the antialiasing filter. The sampling scheme used for the transducers distributed on the flare consisted of 48 consecutively measured data points sampled evenly for 1.2407×10^{-3} seconds, as shown in Figure A-6b. The fundamental frequency for these evenly-sampled blocks of data is ~ 806 Hz. The Fourier transform of these blocks of data are free of the distortion caused by sidelobes. The frequency resolution for these evenly-sampled blocks is low, but they may be used to validate the interpolation method used to analyze unevenly-sampled data.

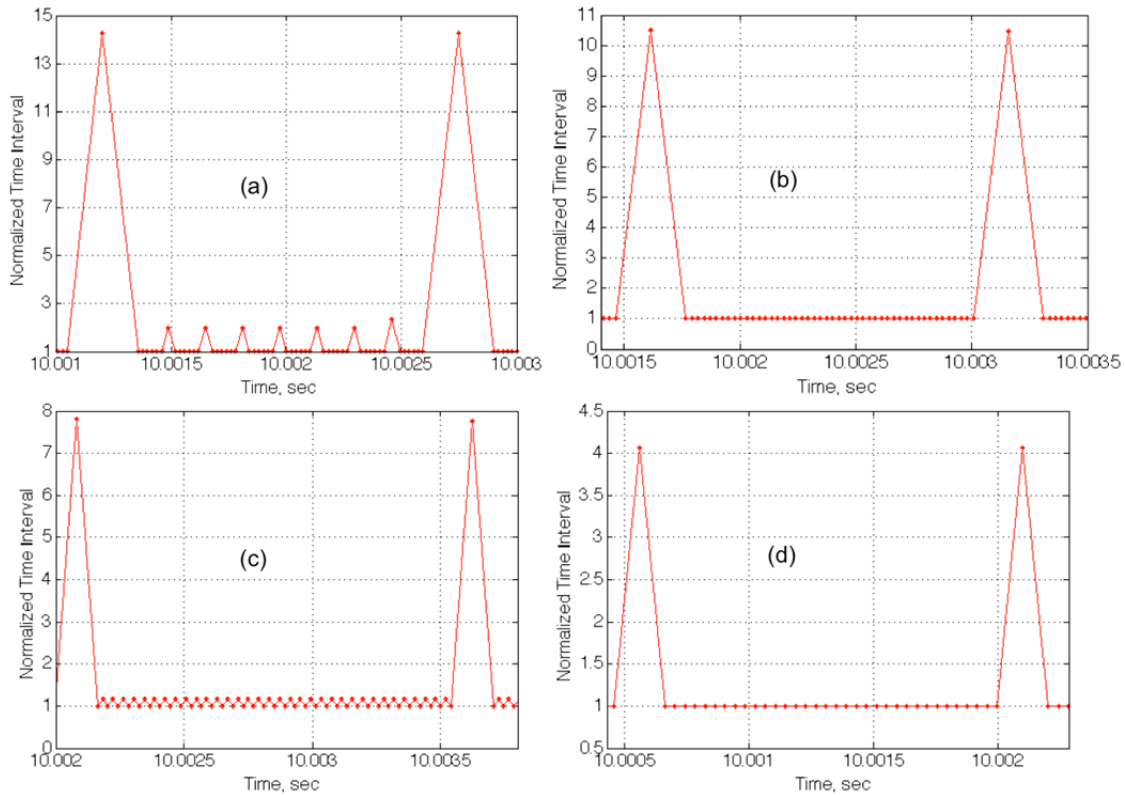


Figure A-6 The Sampling Schemes for (a) Cone Transducers, (b) Flare Transducers, (c) Cylinder Transducers 7, 8, 9, 10, 11, and 19, and (d) Cylinder Transducer 12

Power spectra of the spectral window functions for the high bandwidth pressure transducers are shown in Figure A-7a-d, respectively. The power spectra of the spectral window functions possess numerous sidelobes. These sidelobes cause significant distortion of the Fourier transform. The mean Nyquist frequency, computed using the mean sampling interval and Equation A-1, are given as 17.81, 15.87, and 22.67 kHz for the transducers mounted on the cone, flare, and cylinder, respectively. The cone transducers were bandpass-filtered at 100 Hz – 30 kHz, and those on the cylinder and flare were filtered at 100 Hz – 20 kHz. Signals on the cone and flare were thus subject to some aliasing at higher frequencies, but the cylinder transducers should be free of aliasing.

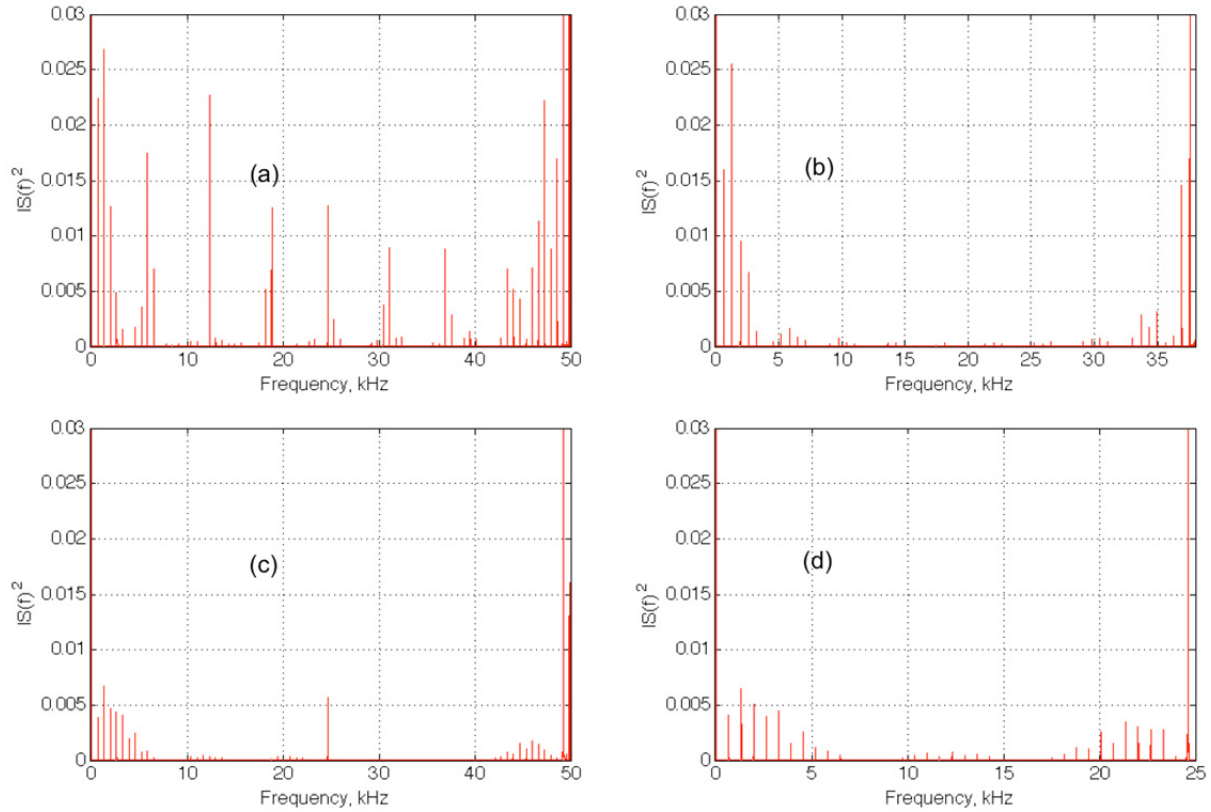


Figure A-7 Power Spectrum of the Spectral Window Function for (a) Cone Transducers, (b) Flare Transducers, (c) Cylinder Transducers 7, 8, 9, 10, 11, and 19, and (d) Cylinder Transducer 12

Interpolating irregularly-spaced data onto a uniformly spaced grid eliminates sidelobes. However, interpolation acts as a low-pass filter, reducing the power at higher frequencies. The amount of power loss depends on the interpolation scheme. In general, every interpolation scheme acts as a low-pass filter causing some power loss³⁶.

The grid spacing for an evenly spaced grid, commonly referred to as the resampling time, is given as

$$t_r = \frac{1}{2f_c} \quad (\text{A-6})$$

where the Nyquist frequency is determined from the spectral window function. The uniform grid is given as $t_n = t_0 + (n - 1)t_r$ for $n = 1, 2, 3, \dots, (t_f - t_0)/t_r$ where t_0 and t_f are the initial and final times of the time series.

Discussion now focuses on estimating the power loss caused by resampling the HIFiRE-1 data onto a uniformly-spaced grid with spacing t_r . This process involves determining a time-series with analytically-describable spectral characteristics similar to the HIFiRE data. The spectral distortion caused by uneven sampling can then be quantified, and this known distortion can then be used to determine the transfer function of the resampling process.

Consider Langevin's equation describing the velocity $x(t_n)$ of a Brownian particle given as

$$dx(t) = \tau x(t)dt + d\xi(t) \quad (\text{A-7})$$

where $\tau < 0$ and $\xi(t)$ represents a random process consistent with Brownian motion. According to Robinson⁶, the velocity samples generated by Equation A-7 are also generated by

$$x(t_n) = \exp\left(-\frac{t_n - t_{n-1}}{\tau}\right) x(t_{n-1}) + \varepsilon(t_n) \quad (\text{A-8})$$

where

$$\varepsilon(t_n) \sim N\left\{0, 1 - \exp\left(-2\frac{t_n - t_{n-1}}{\tau}\right)\right\} \quad (\text{A-9})$$

In Equation A-9, ε represents the random component of the time series and is assumed to have a normal distribution with a mean and variance of zero and $1 - \exp\left(-2\frac{t_n - t_{n-1}}{\tau}\right)$, respectively.

The autospectral density function can be determined by computing the Fourier transform of the autocorrelation function of Equation A-8 and is given as

$$G_{\tilde{x}\tilde{x}}(f) = G_0 \frac{1 - \rho^2}{1 - 2\rho \cos\left(\frac{\pi f}{f_c}\right) + \rho^2} \quad (\text{A-10})$$

where G_0 is the average spectral amplitude and ρ is given as

$$\rho = \exp\left(-\frac{\overline{\Delta t}}{\tau}\right). \quad (\text{A-11})$$

In Equation A-11, τ is a time constant and represents the decay period of the autocorrelation function, and $\overline{\Delta t}$ is the average sampling interval given as

$$\overline{\Delta t} = \frac{t_N - t_1}{N - 1}. \quad (\text{A-12})$$

According to Robinson³⁷, Equation A-8 may be thought of as a first order autoregressive model with time-varying coefficients and heteroscedastic errors.

Equations A-8 and A-10 provide a way to compute time series data with a known autospectral density function for any arbitrary sampling scheme. Figure A-8a compares analytically and numerically obtained autospectral density function of Equation A-10. The analytical autospectral density was obtained using Equation A-10. The numerical autospectral density was obtained for a uniformly-sampled time-series using procedures given in Bendat and Piersol⁷. The comparison is nearly identical.

The power loss caused by resampling the HIFiRE-1 data was estimated by generating time series data for Equation A-8 using the HIFiRE-1 sampling scheme. This time series was then interpolated onto an evenly spaced grid. The analytical autospectral density function was determined from Equation A-8 and compared with the autospectral density function computed from the interpolated time series. Comparisons are shown in Figure A-8b-d for transducers located on the cone, flare, and cylinder. The results shown in Figure A-8b-d are for a linear interpolation scheme. Other interpolation methods were investigated and yielded similar results. As shown in Figure A-8, the power loss was greatest for the transducers located on the cone. Transducers located on the flare experienced the least power loss. It is reasonable that the cone transducers experienced a greater power reduction than the flare transducers, because the cone data were missing more samples than the flare data, as shown in Figure A-6. Similarly, data blocks with many missing data points, such as near the beginning of the first and second stage rocket burn, will experience the most power reduction. Uncertainty for these data blocks will be greater than for data blocks with fewer missing samples.

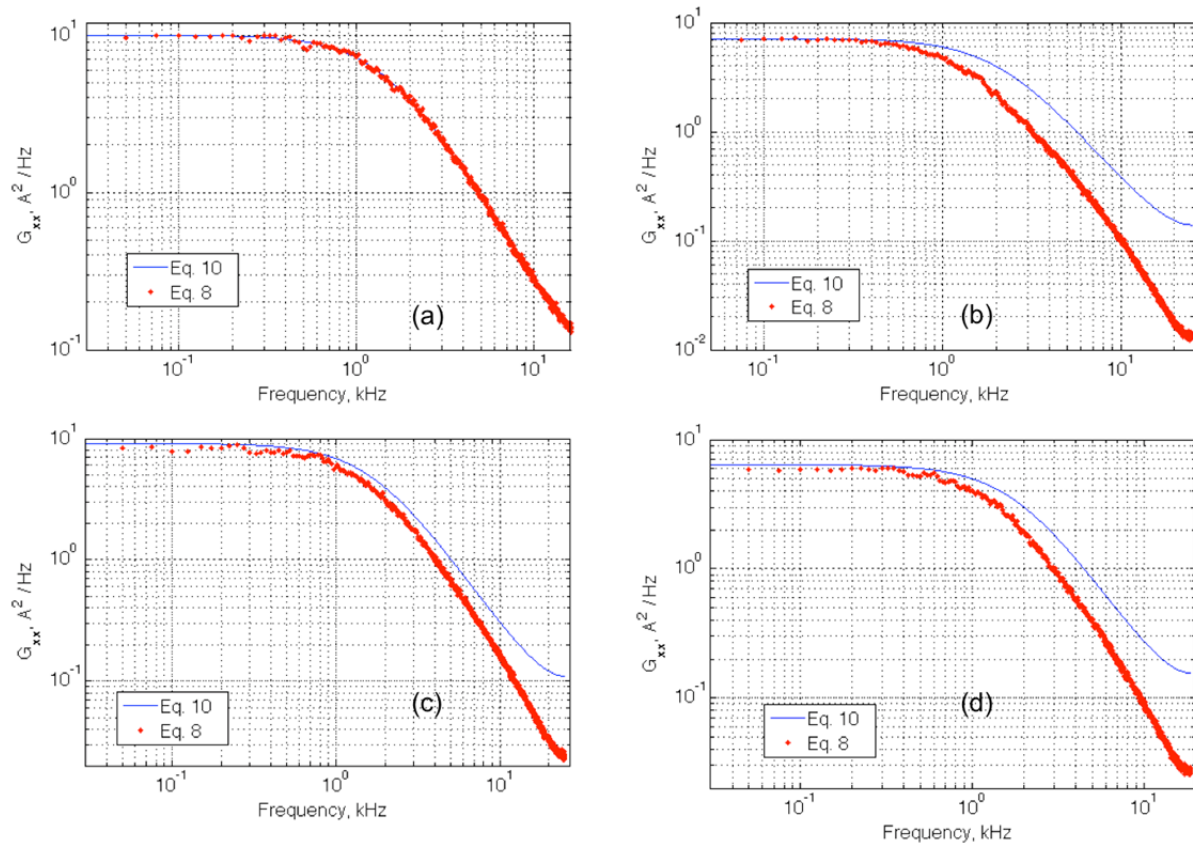


Figure A-8 Theoretical Autospectral Density Function for Equation A-8 Compared to Autospectral Density Functions for Various Sampling Schemes Interpolated Onto Uniformly-Sampled Time Series (a) Uniformly-Sampled, (b) Cone Transducer Sampling Scheme, (c) Flare Transducer Sampling, and (d) Cylinder Transducer Sampling

As discussed in the previous section, interpolating unevenly sampled data onto an evenly spaced grid eliminates the nonlinear sidelobes but acts as a low-pass filter, reducing the power of the higher frequency content. In this section, a method is developed to compensate this reduction in power caused by linear interpolation. The compensation method is very similar to the method given by Schulz and Mudelsee.⁸ After compensation, the autospectral density function is similar to the autospectral density function of $x'(t)$.

It is assumed that the time series data does not have sinusoidal periodic, complex periodic, or almost-periodic components and is a stochastic time series with a red-noise-like autospectral density function. Sinusoidal components should be removed from the time series before compensation. The steps for the compensation method are as follows:

1. Determine τ by fitting the measured data with Equation A-8. There are two equivalent approaches for determining τ in Equation A-8 from the measured data. The first approach is to use the estimation procedure given by Mudelsee,⁹ which utilizes Brent's method. The second approach utilizes the equations given in this paper. To begin,

interpolate the measured data onto a uniformly spaced grid and determine the autoregressive coefficient given as

$$\hat{\phi}_1 = \exp\left(-\frac{\Delta t}{\tau}\right) \quad (\text{A-13})$$

by fitting the interpolated data using least squares given as

$$\begin{bmatrix} \sum_{m=n+1}^M x_{m-1}^2 & \sum_{m=n+1}^M x_{m-1}x_{m-2} \\ \sum_{m=n+1}^M x_{m-1}x_{m-2} & \sum_{m=n+1}^M x_{m-2}^2 \end{bmatrix} \begin{bmatrix} \hat{\phi}_0 \\ \hat{\phi}_1 \end{bmatrix} = \begin{bmatrix} \sum_{m=n+1}^M x_m x_{m-1} \\ \sum_{m=n+1}^M x_m x_{m-2} \end{bmatrix} \quad (\text{A-14})$$

In Equation A-4, M is the total number of autoregressive coefficients. The time constant is given as

$$\tau_{fit} = -\frac{\Delta t}{\log \hat{\phi}_1} \quad (\text{A-15})$$

The time constant given in Equation A-15 does not actually correspond to τ of the measured data. Instead, an iterative procedure is required to determine the appropriate value for τ . In this iterative procedure, τ is assigned an initial value designated as τ' . Next, compute a time series for $\tau = \tau'$ using Equation A-8 for the same sampling scheme used in the measured data. Interpolate this time series onto the same uniform grid used to analyze the measured time series data. Determine the time constant, $\tilde{\tau}$, for this time series using Eqs. A-14 and A-15. Adjust τ' so that $|\tilde{\tau} - \tau_{fit}| \rightarrow 0$. The time constant of the measured data is then estimated as τ' .

2. Compute an autoregressive time series using Equation A-8 for $\tau = \tau'$.
3. Interpolate the time series data from Step 2 and compute the autospectral density function. The autospectral density function from this step is designated as G'_{AR} .
4. Compute the autospectral density function of the time series data from Step 2 using Equation A-10. The autospectral density function from this step is designated as G_{AR} .
5. Compute the compensation factor given as

$$H(f) = \frac{G_{AR}(f)}{G'_{AR}(f)} \quad (\text{A-16})$$

6. Determine the compensated autospectral density function given as

$$G_{xx}(f) = H(f)G'_{xx}(f) \quad (\text{A-17})$$

where $G'_{xx}(f)$ is the autospectral density function of the measured data interpolated onto an evenly spaced grid.

The compensation method was checked in two ways. In one approach, short blocks of flight data with even sampling rates provided undistorted spectra. In the second approach, a large-eddy simulation (LES) of a turbulent shock boundary layer interaction provided a time-series that could be evenly and unevenly sampled. The evenly-sampled LES time series provided a truth-model against which to compare the unevenly-sampled, compensated spectrum.

As shown in Figure A-6b, the flight sampling scheme on the flare featured evenly sampled blocks of data separated by gaps. The autospectrum for evenly-sampled blocks was determined by averaging the autospectrum over 1200 blocks of data. This spectrum was treated as a known spectrum with frequency resolution of approximately 700 Hz. This known spectrum is designated as $G(ESTS)$. The autospectrum of unevenly sampled data was determined from the

flare data by partitioning the data into blocks which contained the gaps. As shown in Figure A-9, the interpolated spectrum $G'_{xx}(f)$ is significantly lower than the baseline spectrum $G(ESTS)$ for frequencies greater than 2 kHz. A comparison between the compensated spectrum $G_{xx}(f)$ and $G(ESTS)$ shows that the compensation method recovers the correct roll-off and power levels. The baseline spectrum was determined from the evenly sampled blocks of data shown in Figure A-6b.

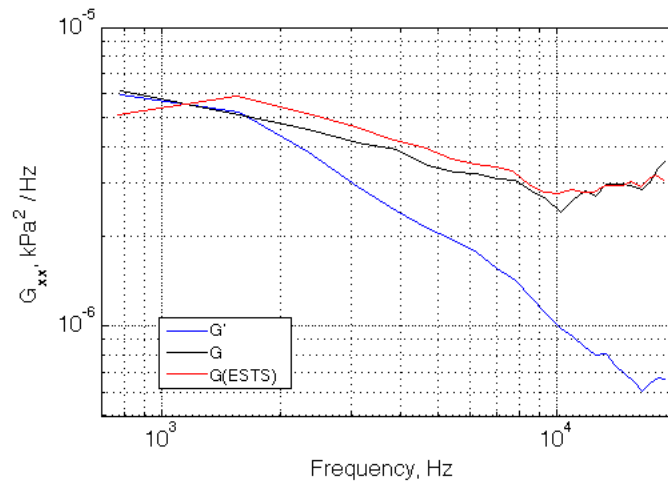


Figure A-9 Comparison Between $G'_{xx}(f)$ and $G_{xx}(f)$ With a Baseline Spectrum for Transducer 21

The compensation method was also validated using numerical time series data.¹⁰ This numerical time series was sampled evenly at 192.9 MHz. The numerical time series was resampled to match the sampling scheme used for the cone transducers. The numerical time series was digitally low-pass filtered prior to resampling. Resampling was accomplished by sampling the time series using the sampling scheme shown in Figure A-6a. Since the numerical time-series was sampled at discrete time intervals, the uneven sampling rate was similar to the HIFiRE sampling rate, but did not exactly reproduce it. The spectral window functions for the sampling scheme of the cone transducers and the resampled numerical time series are shown in Figure A-10. The frequencies were normalized by the Nyquist frequency of each sampling scheme. As shown, the spectral window functions are very similar, thus the distortion caused by sidelobes should be very similar for the two time series. In Figure A-11, the autospectral density function was determined for the evenly spaced numerical time series, the unevenly spaced numerical time series interpolated onto an evenly spaced grid, and the unevenly-spaced time series, interpolated and compensated. As shown in Figure A-11, the compensation method recovers the roll-off and power loss caused by interpolating the unevenly sampled numerical time series onto an evenly grid. This numerical experiment and the comparison of unevenly to evenly-spaced flight data confirm the validity of the compensation method.

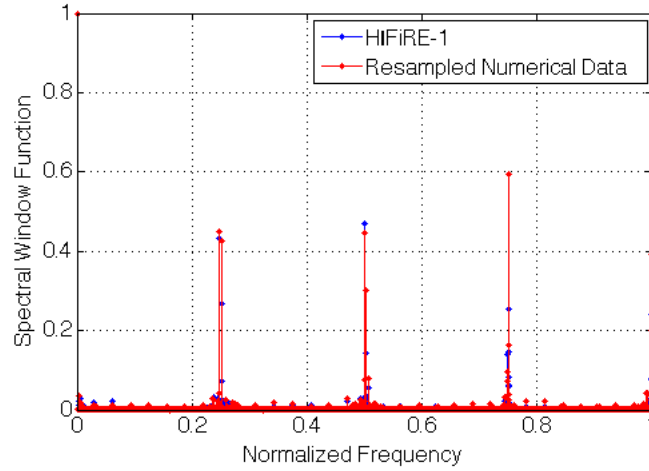


Figure A-10 Comparison Between the Spectral Window Functions of the Cone Transducer Flight Sampling Scheme and the Resampled Numerical Time Series

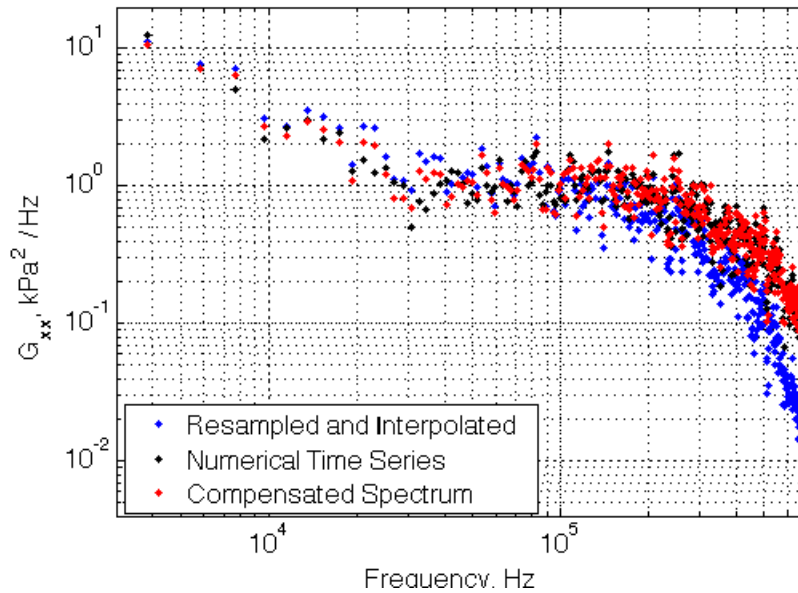


Figure A-11 Comparison Among the Autospectral Density Function of the Compensated Spectrum, the Evenly Sampled Numerical Time Series, and the Resampled Numerical Time Series

A comparison between the dimensional and nondimensional $G'_{xx}(f)$ and $G_{xx}(f)$ for surface pressure measurements recorded at different times during the ascent by transducers 7 and 9 located on the cylinder are shown in Figure A-12 and Figure A-13. These transducers were located respectively 8 and 6 cm upstream of the flare. The frequency and autospectral density function were normalized using the edge velocity boundary layer thickness and the dynamic pressure. These normalizing quantities were provided by Robert Yentsch of The Ohio State University. The flight conditions for the times shown in Figure A-12 and Figure A-13 are

summarized in the Table A-1 below. Times prior to $t=6$ seconds correspond to the first-stage boost phase. Times between $t=6$ and $t=15$ seconds correspond to the coast phase between first-stage burnout and second-stage ignition.

The flight data show a rolloff in amplitude with increasing frequency, typical of that seen in shock-boundary interactions.¹¹ As shown in the figure, the compensation method does not noticeably alter power levels for frequencies below 1.5 to 3 kHz but becomes more prominent as the frequency increases. The compensated spectra roll off at a rate of about 8 dB/octave. This rolloff rate is slightly lower than that observed in Ref 10, but similar to other data cited in the same reference. These data, combined with checks against numerical experiment and small blocks of evenly-sampled flight data, indicate that unevenly-sampled flight data may be analyzed to provide meaningful spectral data.

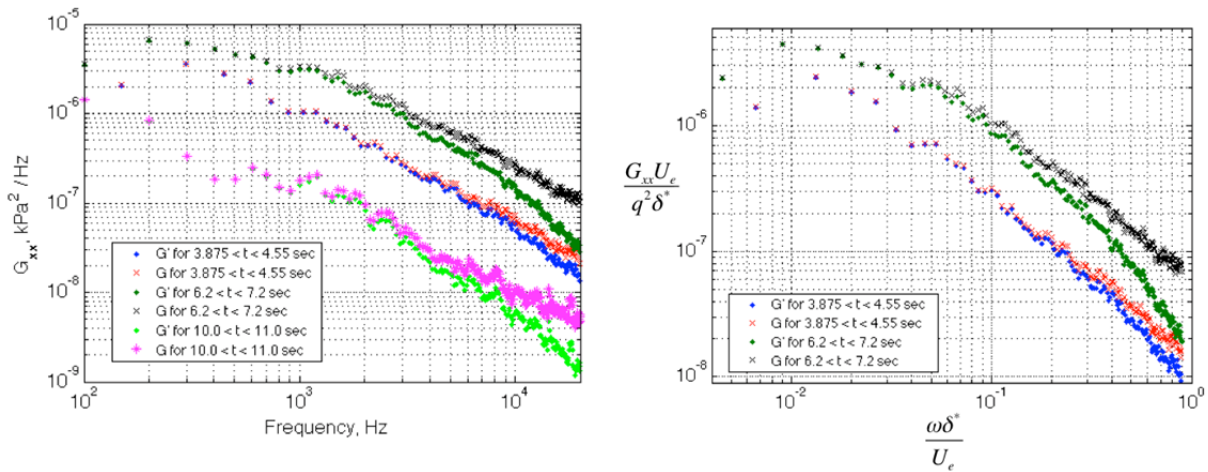


Figure A-12 (a) $G'_{xx}(f)$ and $G_{xx}(f)$ at Selected Times During the Ascent, (b) Normalized $G'_{xx}(f)$ and $G_{xx}(f)$

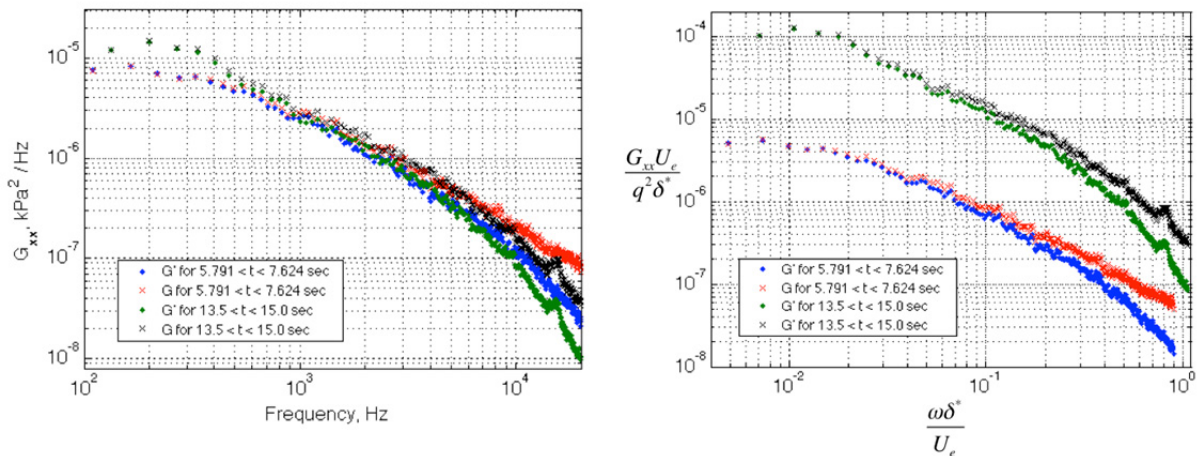


Figure A-13 (a) $G'_{xx}(f)$ and $G_{xx}(f)$ at Selected Later Times During the Ascent, (b) Normalized $G'_{xx}(f)$ and $G_{xx}(f)$

Table A-1 Flight Conditions Analyzed

Time, sec	Freestream Mach, M	Freestream Unit Reynolds Number per meter
3.870	2.14	4.26E+07
4.550	2.61	4.95E+07
6.200	3.43	5.57E+07
7.200	3.25	4.71E+07
5.791	3.41	5.80E+07
7.624	3.19	4.44E+07
10.000	2.90	3.20E+07
11.000	2.83	2.88E+07
13.500	2.67	2.21E+07
15.000	2.58	1.89E+07

In conclusion, computing the autospectral density function directly from an unevenly sampled time series results in a distorted spectrum. The distortion is caused by nonlinear sidelobes. This nonlinearity can be removed by resampling the unevenly-sampled time series onto an evenly-spaced grid, at the cost of under predicting the power of the higher frequency components. A compensation method was implemented to recover the power lost by resampling. Specifically, the compensation method estimated the autospectral density function of stochastic, surface pressure data having red-noise spectra similar to the HIFiRE-1 pressure data. This compensation method estimated the autospectral density function by determining a correction factor. The coefficients of a first-order, autoregressive model, that holds for unevenly sampled data, are determined from the measured time series data using a nonlinear least squares procedure. The autoregressive coefficients are used to generate a time series with the same sampling scheme as the surface pressure data. This autoregressive time series and measured time series are resampled onto an evenly spaced grid. The autospectral density function is computed from the resampled autoregressive time series, the resampled measured data, and directly from the autoregressive coefficients. A correction factor is determined by taking the ratio of the autospectral density function computed from the autoregressive coefficients with the autospectral density function of the resampled autoregressive time series. The autospectral density function of the measured data is estimated by multiplying the correction factor with the autospectral density function of the resampled measured pressure data.

The time series data measured during the flight experiment has some aerothermal data that would benefit from correlation-based analysis such as crossflow instabilities, rolling and pitching motions of the payload, and shock-foot motion overtop surface mounted transducers. Future work will investigate methods for preserving the phase information of the time series data recorded during the HIFiRE-1 flight.

References

¹ Scargle, J. D, "Studies in Astronomical Time Series Analysis. III. Fourier Transforms, Autocorrelation Functions, and Cross-Correlation Functions of Unevenly Spaced Data," *The Astrophysical Journal*, Vol. 343, pp. 874-887, 1989.

-
- ² Schulz, M. and Stattegger, K., "Spectrum: Spectral Analysis of Unevenly Spaced Paleoclimatic Time Series," *Computers & Geosciences*, Vol. 23, pp. 929-945, 1997.
- ³ Horowitz, L. L., "The Effects of Spline Interpolation on Power Spectral Density," *IEEE Trans. Audio Electroacoust.*, Vol. ASSP-22, pp. 22-27, 1974.
- ⁴ Babu, P. and Stoica, P., "Spectral Analysis of Nonuniformly Sampled Data – A Review," *Digital Signal Processing*, Vol. 20, pp. 359-378, 2010.
- ⁵ Deeming, T. J., "Fourier Analysis with Unequally-Spaced Data," *Astrophysics and Space Science*, Vol. 36, pp. 137-158, 1975.
- ⁶ Robinson, P. M., "Estimation of a Time Series Model from Unequally Spaced Data," *Stochastic Processes and their Applications*, Vol. 6, pp. 9-24, 1977.
- ⁷ Bendat, J. S., and Piersol, A. G., *Random Data Analysis and Measurement Procedures*, 4th Ed., John Wiley & Sons, Inc., New Jersey, 2010, pp. 386 – 404.
- ⁸ Schulz, M. and Mudelsee, M., "REDFIT: Estimating Red-Noise Spectra Directly from Unevenly Spaced Paleoclimatic Time series," *Computers & Geosciences*, Vol. 28, pp. 421-426, 2002.
- ⁹ Mudelsee, M., "TAUEST: A Computer Program for Estimating Persistence in Unevenly Spaced Weather / Climate Time Series," *Computers & Geosciences*, Vol. 28, pp. 69-72, 2002.
- ¹⁰ Poggie, J., Bisek, N. J., Kimmel, R. L., Stanfield, S. A., "Spectral Characteristics and Reduced-Order Modeling of Separation Shock Unsteadiness," AIAA paper, 43rd AIAA Fluid Dynamics Conference, June 2013.
- ¹¹ Dolling, D. S. and Or, C. T., "Unsteadiness of the Shock Wave Structure in Attached and Separated Compression Ramp Flows," *Experiments in Fluids*, Vol. 3, 1985, pp. 24-32.